

1 SEARCH FOR PRODUCTION OF A HIGGS BOSON AND A SINGLE TOP  
2 QUARK IN MULTILEPTON FINAL STATES IN  $pp$  COLLISIONS AT  $\sqrt{s} = 13$   
3 TeV.

4 by

5 Jose Andres Monroy Monta  ez

# A DISSERTATION

7 Presented to the Faculty of

8 The Graduate College at the University of Nebraska

9 In Partial Fulfilment of Requirements

10 For the Degree of Doctor of Philosophy

11 Major: Physics and Astronomy

<sup>12</sup> Under the Supervision of Kenneth Bloom and Aaron Dominguez

13 Lincoln, Nebraska

14 July, 2018

15 SEARCH FOR PRODUCTION OF A HIGGS BOSON AND A SINGLE TOP  
16 QUARK IN MULTILEPTON FINAL STATES IN pp COLLISIONS AT  $\sqrt{s} = 13$   
17 TeV.

18 Jose Andres Monroy Montañez, Ph.D.

19 University of Nebraska, 2018

20 Adviser: Kenneth Bloom and Aaron Dominguez

# **<sup>21</sup> Table of Contents**

<b><sup>22</sup> Table of Contents</b>	<b>iii</b>
<b><sup>23</sup> List of Figures</b>	<b>vi</b>
<b><sup>24</sup> List of Tables</b>	<b>ix</b>
<b><sup>25</sup> 1 INTRODUCTION</b>	<b>1</b>
<b><sup>26</sup> 2 Theoretical approach</b>	<b>2</b>
27     2.1 Introduction . . . . .	2
28     2.2 Standard model of particle physics . . . . .	3
29     2.2.1 Fermions . . . . .	5
30     2.2.1.1 Leptons . . . . .	6
31     2.2.1.2 Quarks . . . . .	8
32     2.2.2 Fundamental interactions . . . . .	12
33     2.2.3 Gauge bosons . . . . .	18
34     2.3 Electroweak unification and the Higgs mechanism . . . . .	20
35     2.3.1 Spontaneous symmetry breaking (SSB) . . . . .	28
36     2.3.2 Higgs mechanism . . . . .	32
37     2.3.3 Masses of the gauge bosons . . . . .	34

38	2.3.4	Masses of the fermions . . . . .	35
39	2.3.5	The Higgs field . . . . .	36
40	2.3.6	Production of Higgs bosons at LHC . . . . .	37
41	2.3.7	Higgs boson decay channels . . . . .	41
42	2.4	Associated production of a Higgs boson and a single Top quark. . . . .	42
43	2.5	The CP-mixing in tH processes . . . . .	47
44	2.6	Experimantal status of the anomalous Higg-fermion coupling. . . . .	51
45	<b>3</b>	<b>The CMS experiment at the LHC</b>	<b>53</b>
46	3.1	Introduction . . . . .	53
47	3.2	The LHC . . . . .	54
48	3.3	The CMS experiment . . . . .	63
49	3.3.1	Coordinate system . . . . .	65
50	3.3.2	Pixels detector . . . . .	67
51	3.3.3	Silicon strip tracker . . . . .	69
52	3.3.4	Electromagnetic calorimeter . . . . .	70
53	3.3.5	Hadronic calorimeter . . . . .	72
54	3.3.6	Superconducting solenoid magnet . . . . .	73
55	3.3.7	Muon system . . . . .	75
56	3.3.8	CMS trigger system . . . . .	76
57	3.3.9	CMS computing . . . . .	78
58	<b>4</b>	<b>Event generation, simulation and reconstruction</b>	<b>82</b>
59	4.1	Event generation . . . . .	83
60	4.2	Monte Carlo Event Generators. . . . .	87
61	4.3	CMS detector simulation. . . . .	88
62	4.4	Event reconstruction. . . . .	90

63	4.4.1	Particle-Flow Algorithm. . . . .	91
64	4.5	MVA methods, NN, BDT, boosting, overtraining, variable ranking .	97
65	4.6	statistical inference, likelihood parametrization . . . . .	97
66	4.7	nuisance parameters . . . . .	97
67	4.8	exclusion limits . . . . .	97
68	4.9	asymptotic limits . . . . .	97
69	<b>5</b>	<b>Search for production of a Higgs boson and a single top quark in multilepton final states in pp collisions at <math>\sqrt{s} = 13</math> TeV</b>	<b>98</b>
70	5.1	Introduction . . . . .	98
71	5.2	Data and MC Samples . . . . .	100
72	5.2.1	Full 2016 dataset and MC samples . . . . .	100
73	5.2.2	Triggers . . . . .	103
74	5.2.2.1	Trigger efficiency scale factors . . . . .	103
75	5.3	Object Identification and event selection . . . . .	104
76	5.3.1	Jets and $b$ tagging . . . . .	104
77	5.3.2	Lepton selection . . . . .	105
78	5.3.3	Lepton selection efficiency . . . . .	106
79	5.4	Background predictions . . . . .	107
80	5.5	Signal discrimination . . . . .	108
81	5.5.1	Classifiers response . . . . .	112
82	5.6	Additional discriminating variables . . . . .	115
84	<b>Bibliography</b>		<b>116</b>
85	<b>References</b>		<b>118</b>

## <sup>86</sup> List of Figures

87	2.1	Standard model of particle physics.	4
88	2.2	Transformations between quarks	12
89	2.3	Fundamental interactions in nature.	13
90	2.4	SM interactions diagrams	14
91	2.5	Neutral current processes	21
92	2.6	Spontaneous symmetry breaking mechanism	28
93	2.7	SSB Potential form	29
94	2.8	Potential for complex scalar field	30
95	2.9	SSB mechanism for complex scalar field	31
96	2.10	Proton-Proton collision	38
97	2.11	Higgs boson production mechanism Feynman diagrams	39
98	2.12	Higgs boson production cross section and decay branching ratios	40
99	2.13	Associated Higgs boson production mechanism Feynman diagrams	43
100	2.14	Cross section for tHq process as a function of $\kappa_t$	45
101	2.15	Cross section for $tHW$ process as a function of $\kappa_{Htt}$	46
102	2.16	NLO cross section for $tX_0$ and $t\bar{t}X_0$ .	49
103	2.17	NLO cross section for $tWX_0$ , $t\bar{t}X_0$ .	50

104	2.18 Two dimentional $\kappa_t$ - $\kappa_V$ plot of the coupling modifiers. ATLAS and CMS 105 combination. . . . .	51
106	3.1 CERN accelerator complex . . . . .	54
107	3.2 LHC protons source. First acceleration stage. . . . .	55
108	3.3 The LINAC2 accelerating system at CERN. . . . .	56
109	3.4 LHC layout and RF cavities module. . . . .	57
110	3.5 LHC dipole magnet. . . . .	59
111	3.6 Integrated luminosity delivered by LHC and recorded by CMS during 2016	61
112	3.7 LHC interaction points . . . . .	62
113	3.8 Multiple $pp$ collision bunch crossing at CMS. . . . .	64
114	3.9 Layout of the CMS detector . . . . .	65
115	3.10 CMS detector coordinate system . . . . .	66
116	3.11 CMS pixel detector schematic view. . . . .	68
117	3.12 SST Schematic view. . . . .	69
118	3.13 CMS ECAL schematic view . . . . .	71
119	3.14 CMS HCAL schematic view . . . . .	73
120	3.15 CMS solenoid magnet . . . . .	74
121	3.16 CMS Muon system schematic view . . . . .	75
122	3.17 CMS Level-1 trigger architecture . . . . .	77
123	3.18 WLCG structure . . . . .	78
124	3.19 Data flow from CMS detector through hardware Tiers . . . . .	81
125	4.1 Event generation process. . . . .	83
126	5.1 The two leading-order diagrams of $tHq$ production. . . . .	99
127	5.2 Input variables to the BDT for signal discrimination normalized. . . . .	109

128	5.3	Input variables to the BDT for signal discrimination not normalized. . . . .	111
129	5.4	BDT inputs as seen by TMVA against $t\bar{t}$ . . . . .	112
130	5.5	BDT inputs as seen by TMVA against $t\bar{t}V$ . . . . .	113
131	5.6	Correlation matrices for the input variables in the TMVA. . . . .	114
132	5.7	MVA classifiers performance. . . . .	114
133	5.8	Additional discriminating variables distributions. . . . .	116

# <sup>134</sup> List of Tables

135	2.1	Fermions of the SM. . . . .	5
136	2.2	Fermion masses. . . . .	6
137	2.3	Leptons properties. . . . .	9
138	2.4	Quarks properties. . . . .	9
139	2.5	Fermion weak isospin and weak hypercharge multiplets. . . . .	11
140	2.6	Fundamental interactions features. . . . .	15
141	2.7	SM gauge bosons. . . . .	19
142	2.8	Higgs boson properties. . . . .	37
143	2.9	Predicted branching ratios for a SM Higgs boson with $m_H = 125 \text{ GeV}/c^2$ . . . . .	42
144	2.10	Predicted SM cross sections for $tH$ production at $\sqrt{s} = 13 \text{ TeV}$ . . . . .	44
145	2.11	Predicted enhancement of the $tHq$ and $tHW$ cross sections at LHC . . . . .	47
146	5.1	Signal samples and their cross section and branching fraction. . . . .	100
147	5.2	$\kappa_V$ and $\kappa_t$ combinations. . . . .	101
148	5.3	List of background samples used in this analysis (CMSSW 80X). . . . .	102
149	5.4	Leading-order $t\bar{t}W$ and $t\bar{t}Z$ samples used in the signal BDT training. . . . .	102
150	5.5	Table of high-level triggers that we consider in the analysis. . . . .	103
151	5.6	Trigger efficiency scale factors and associated uncertainties. . . . .	104
152	5.7	Requirements on each of the three muon selections. . . . .	105

153	5.8 Criteria for each of the three electron selections. . . . .	106
154	5.9 MVA input discriminating variables . . . . .	110
155	5.10 TMVA input variables ranking for BDTA_GRAD method . . . . .	115
156	5.11 TMVA configuration used in the BDT training. . . . .	115
157	5.12 ROC-integral for all the testing cases. . . . .	117

<sup>158</sup> Chapter 1

<sup>159</sup> INTRODUCTION

# <sup>160</sup> Chapter 2

## <sup>161</sup> Theoretical approach

### <sup>162</sup> 2.1 Introduction

<sup>163</sup> The physical description of the universe is a challenge that physicists have faced by  
<sup>164</sup> making theories that refine existing principles and proposing new ones in an attempt  
<sup>165</sup> to embrace emerging facts and phenomena.

<sup>166</sup>

<sup>167</sup> At the end of 1940s Julian Schwinger [1] and Richard P. Feynman [2], based in the  
<sup>168</sup> work of Sin-Itiro Tomonaga [3], developed an electromagnetic theory consistent with  
<sup>169</sup> special relativity and quantum mechanics that describes how matter and light inter-  
<sup>170</sup> act; the so-called “quantum eletrodynamics” (QED) had born.

<sup>171</sup>

<sup>172</sup> QED has become the guide in the development of theories that describe the universe.  
<sup>173</sup> It was the first example of a quantum field theory (QFT), which is the theoretical  
<sup>174</sup> framework for building quantum mechanical models that describes particles and their  
<sup>175</sup> interactions. QFT is composed of a set of mathematical tools that combines classical  
<sup>176</sup> fields, special relativity and quantum mechanics, while keeping the quantum point

177 particles and locality ideas.

178 This chapter gives an overview of the standard model of particle physics, starting  
 179 with a description of the particles and interactions that compose it, followed by a  
 180 description of the electroweak interaction, the Higgs boson and the associated pro-  
 181 duction of Higgs boson and a single top quark ( $tH$ ). The description contained in  
 182 this chapter is based on references [4–6].

## 183 2.2 Standard model of particle physics

184 Particle physics at the fundamental level is modeled in terms of a collection of in-  
 185 teracting particles and fields in a theory known as the “standard model of particle  
 186 physics (SM)”<sup>1</sup>.

187

188 The full picture of the SM is composed of three fields<sup>2</sup>, whose excitations are inter-  
 189 preted as particles called mediators or force-carriers; a set of fields, whose excitations  
 190 are interpreted as elementary particles, interacting through the exchange of those  
 191 mediators and a field that gives the mass to elementary particles. Figure 2.1 shows  
 192 an scheme of the SM particles organization. In addition to the particles in the scheme  
 193 (but not listed in it), their corresponding anti-particles, with opposite quantum num-  
 194 bers, are also part of the picture; some particles are their own anti-particles, like  
 195 photon or Higgs, or anti-particle is already listed like in the  $W^+$  and  $W^-$  case.

196

197 The mathematical formulation of the SM is based on group theory and the use of  
 198 Noether’s theorem [8] which states that for a physical system modeled by a Lagrangian

---

<sup>1</sup> The formal and complete treatment of the SM is out of the scope of this document, however a plenty of textbooks describing it at several levels are available in the literature. The treatment in references [?] is quite comprehensive and detailed.

<sup>2</sup> Note that gravitational field is not included in the standard model formulation

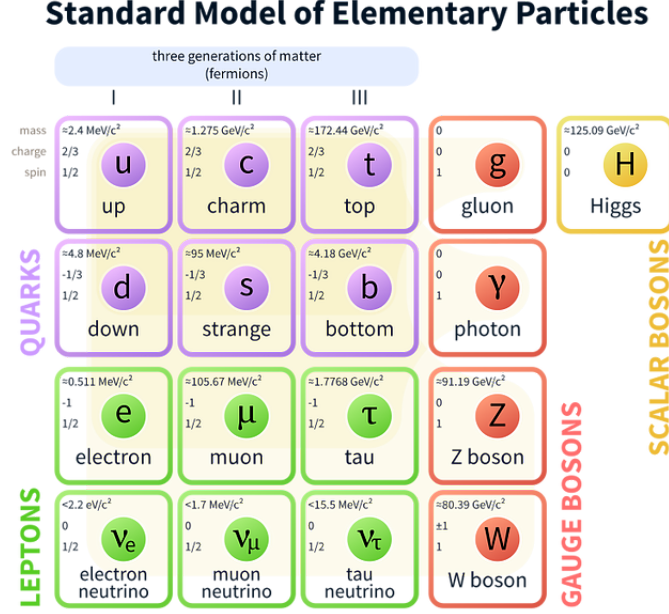


**Figure 2.1:** Schematic representation of the Standard model of particle physics. SM is a theoretical model intended to describe three of the four fundamental forces of the universe in terms of a set of particles and their interactions. [7].

199 that is invariant under a group of transformations a conservation law is expected. For  
 200 instance, a system described by a time-independent Lagrangian is invariant (symmet-  
 201 ric) under time changes (transformations) with the total energy conservation law as  
 202 the expected conservation law. In QED, the charge operator ( $Q$ ) is the generator of  
 203 the  $U(1)$  symmetry which according to the Noether's theorem means that there is a  
 204 conserved quantity; this conserved quantity is the electric charge and thus the law  
 205 conservation of electric charge is established.

206

207 In the SM, the symmetry group  $SU(3)_C \otimes SU(2)_L \otimes U(1)_Y$  describes three of the  
 208 four fundamental interactions in nature(see section 2.2.2): strong interaction(SI),  
 209 weak interaction(WI) and electromagnetic interactions (EI) in terms of symmetries  
 210 associated to physical quantities:

- 211     • Strong:  $SU(3)_C$  associated to color charge
- 212     • Weak:  $SU(2)_L$  associated to weak isospin and chirality
- 213     • Electromagnetic:  $U(1)_Y$  associated to weak hypercharge and electric charge
- 214   It will be shown that the electromagnetic and weak interactions are combined in  
 215   the so-called electroweak interaction where chirality, hypercharge, weak isospin and  
 216   electric charge are the central concepts.

### 217   **2.2.1 Fermions**

218   The basic constituents of the ordinary matter at the lowest level, which form the set  
 219   of elementary particles in the SM formulation, are quarks and leptons. All of them  
 220   have spin 1/2, therefore they are classified as fermions since they obey Fermi-Dirac  
 221   statistics. There are six “flavors” of quarks and three of leptons organized in three  
 222   generations, or families, as shown in table 2.1.

223

		Generation		
		1st	2nd	3rd
Leptons	Charged	Electron (e)	Moun( $\mu$ )	Tau ( $\tau$ )
	Neutral	Electron neutrino ( $\nu_e$ )	Muon neutrino ( $\nu_\mu$ )	Tau neutrino ( $\nu_\tau$ )
Quarks	Up-type	Up (u)	Charm (c)	Top (t)
	Down-type	Down (d)	Strange (s)	Bottom (b)

**Table 2.1:** Fermions of the SM. There are six flavors of quarks and three of leptons, organized in three generations, or families, composed of two pairs of closely related particles. The close relationship is motivated by the fact that WI between leptons is limited to the members of the same generation; WI between quarks is not limited but greatly favoured, to same generation members.

224

225   There is a mass hierarchy between generations (see table 2.2), where the higher gener-  
 226   ation particles decays to the lower one, which can explain why the ordinary matter is

made of particles in the first generation. In the SM, neutrinos are modeled as massless particles so they are not subject to this mass hierarchy; however, today it is known that neutrinos are massive so the hierarchy could be restated. The reason behind this mass hierarchy is one of the most important open questions in particle physics, and it becomes more puzzling when noticing that the mass difference between first and second generation fermions is small compared to the mass difference with respect to the third generation.

Lepton	Mass (MeV/c <sup>2</sup> )	Quark	Mass (MeV/c <sup>2</sup> )
e	0.51	u	2.2
$\mu$	105.65	c	$1.28 \times 10^3$
$\tau$	1776.86	t	$173.1 \times 10^3$
$\nu_e$	Unknown	d	4.7
$\nu_\mu$	Unknown	s	96
$\tau_\mu$	Unknown	b	$4.18 \times 10^3$

**Table 2.2:** Fermion masses [9]. Generations differ by mass in a way that have been interpreted as a masss hierarchy. Approximate values with no uncertainties are used, for comparison purpose.

234

Usually, the second and third generation fermions are produced in high energy processes, like the ones recreated in particle accelerators.

### 237 2.2.1.1 Leptons

A lepton is an elementary particle that is not subject to the SI. As seen in table 2.1, there are two types of leptons, the charged ones (electron, muon and tau) and the neutral ones (the three neutrinos). The electric charge (Q) is the property that gives leptons the ability to participate in the EI. From the classical point of view, Q plays a central role determining, among others, the strength of the electric field through which the electromagnetic force is exerted. It is clear that neutrinos are not affected

244 by EI because they don't carry electric charge.

245

246 Another feature of the leptons that is fundamental in the mathematical description  
247 of the SM is the chirality, which is closely related to spin and helicity. Helicity defines  
248 the handedness of a particle by relating its spin and momentum such that if they  
249 are parallel then the particle is right-handed; if spin and momentum are antiparallel  
250 the particle is said to be left-handed. The study of parity conservation (or viola-  
251 tion) in  $\beta$ -decay has shown that only left-handed electrons/neutrinos or right-handed  
252 positrons/anti-neutrinos are created [10]; the inclusion of that feature in the theory  
253 was achieved by using projection operators for helicity, however, helicity is frame de-  
254 pendent for massive particles which makes it not Lorentz invariant and then another  
255 related attribute has to be used: *chirality*.

256

257 Chirality is a purely quantum attribute which makes it not so easy to describe in  
258 graphical terms but it defines how the wave function of a particle transforms under  
259 certain rotations. As with helicity, there are two chiral states, left-handed chiral (L)  
260 and right-handed chiral (R). In the highly relativistic limit where  $E \approx p \gg m$  helicity  
261 and chirality converge, becoming exactly the same for massless particles.

262

263 In the following, when referring to left-handed (right-handed) it will mean left-handed  
264 chiral (right-handed chiral). The fundamental fact about chirality is that while EI  
265 and SI are not sensitive to chirality, in WI left-handed and right-handed fermions are  
266 treated asymmetrically, such that only left handed fermions and right-handed anti-  
267 fermions are allowed to couple to WI mediators, which is a violation of parity. The  
268 way to translate this statement in a formal mathematical formulation is based on the  
269 isospin symmetry group  $SU(2)_L$ .

270

271 Each generation of leptons is seen as a weak isospin doublet.<sup>3</sup> The left-handed charged  
 272 lepton and its associated left-handed neutrino are arranged in doublets of weak isospin  
 273 T=1/2 while their right-handed partners are singlets:

$$\begin{pmatrix} \nu_l \\ l \end{pmatrix}_L, l_R := \begin{pmatrix} \nu_e \\ e \end{pmatrix}_L, \begin{pmatrix} \nu_\mu \\ \mu \end{pmatrix}_L, \begin{pmatrix} \nu_\tau \\ \tau \end{pmatrix}_L, e_R, \mu_R, \tau_R, \nu_{eR}, \nu_{\mu R}, \nu_{\tau R} \quad (2.1)$$

274 The isospin third component refers to the eigenvalues of the weak isospin operator  
 275 which for doublets is  $T_3 = \pm 1/2$ , while for singlets it is  $T_3 = 0$ . The physical meaning  
 276 of this doublet-singlet arrangement falls in that the WI couples the two particles in  
 277 the doublet by exchanging the interaction mediator while the singlet member is not  
 278 involved in WI. The main properties of the leptons are summarized in table 2.3.

279

280 Altough all three flavor neutrinos have been observed, their masses remain unknown  
 281 and only some estimations have been made [11]. The main reason is that the fla-  
 282 vor eigenstates are not the same as the mass eigenstates which implies that when  
 283 a neutrino is created its mass state is a linear combination of the three mass eigen-  
 284 states and experiments can only probe the squared difference of the masses. The  
 285 Pontecorvo-Maki-Nakagawa-Sakata (PMNS) mixing matrix encode the relationship  
 286 between flavor and mass eigenstates.

287

### 288 2.2.1.2 Quarks

289 Quarks are the basic constituents of protons and neutrons. The way quarks join to  
 290 form bound states, called “hadrons”, is through the SI. Quarks are affected by all the

---

<sup>3</sup> The weak isospin is an analogy of the isospin symmetry in strong interaction where neutron and proton are affected equally by strong force but differ in their charge.

Lepton	Q(e)	$T_3$	$L_e$	$L_\mu$	$L_\tau$	Lifetime (s)
Electron (e)	-1	-1/2	1	0	0	Stable
Electron neutrino( $\nu_e$ )	0	1/2	1	0	0	Unknown
Muon ( $\mu$ )	-1	-1/2	0	1	0	$2.19 \times 10^{-6}$
Muon neutrino ( $\nu_\mu$ )	0	1/2	0	1	0	Unknown
Tau ( $\tau$ )	-1	-1/2	0	0	1	$290.3 \times 10^{-15}$
Tau neutrino ( $\tau_\mu$ )	0	1/2	0	0	1	Unknown

**Table 2.3:** Leptons properties [9]. Q: electric charge,  $T_3$ : weak isospin. Only left-handed leptons and right-handed anti-leptons participate in the WI. Anti-particles with inverted  $T_3$ , Q and lepton number complete the leptons set but are not listed. Right-handed leptons and left-handed anti-leptons, neither listed, form weak isospin singlets with  $T_3 = 0$  and do not take part in the weak interaction.

291 fundamental interactions which means that they carry all the four types of charges:  
292 color, electric charge, weak isospin and mass.

Flavor	Q(e)	$I_3$	$T_3$	B	C	S	T	$B'$	Y	Color
Up (u)	2/3	1/2	1/2	1/3	0	0	0	0	1/3	r,b,g
Charm (c)	2/3	0	1/2	1/3	1	0	0	0	4/3	r,b,g
Top(t)	2/3	0	1/2	1/3	0	0	1	0	4/3	r,b,g
Down(d)	-1/3	-1/2	-1/2	1/3	0	0	0	0	1/3	r,b,g
Strange(s)	-1/3	0	-1/2	1/3	0	-1	0	0	-2/3	r,b,g
Bottom(b)	-1/3	0	-1/2	1/3	0	0	0	-1	-2/3	r,b,g

**Table 2.4:** Quarks properties [9]. Q: electric charge,  $I_3$ : isospin,  $T_3$ : weak isospin, B: baryon number, C: charmness, S: strangeness, T: topness,  $B'$ : bottomness, Y: hypercharge. Anti-quarks posses the same mass and spin as quarks but all charges (color, flavor numbers) have opposite sign.

293  
294 Table 2.4 summarizes the features of quarks, among which the most particular is  
295 their fractional electric charge. Note that fractional charge is not a problem, given  
296 that quarks are not found isolated, but serves to explain how composed particles are  
297 formed out of two or more valence quarks<sup>4</sup>.

298

---

<sup>4</sup> Hadrons can contain an indefinite number of virtual quarks and gluons, known as the quark and gluon sea, but only the valence quarks determine hadrons' quantum numbers.

299 Color charge is the responsible for the SI between quarks and is the symmetry  
 300 ( $SU(3)_C$ ) that defines the formalism to describe SI. There are three colors: red (r),  
 301 blue(b) and green(g) and their corresponding three anti-colors; thus each quark carries  
 302 one color unit while anti-quarks carries one anti-color unit. As said above, quarks are  
 303 not allowed to be isolated due to the color confinement effect, therefore their features  
 304 have been studied indirectly by observing their bound states created when:

- 305     • one quark with a color charge is attracted by an anti-quark with the correspond-  
 306         ing anti-color charge forming a colorless particle called a “meson.”
- 307     • three quarks (anti-quarks) with different color (anti-color) charges are attracted  
 308         among them forming a colorless particle called a “baryon(anti-baryon).”

309 In the first version of the quark model (1964), M. Gell-Mann [12] and G. Zweig  
 310 [13, 14] developed a consistent way to classify hadrons according to their properties.  
 311 Only three quarks (u, d, s) were involved in a scheme in which all baryons have  
 312 baryon number  $B=1$  and therefore quarks have  $B=1/3$ ; non-baryons have  $B=0$ . The  
 313 scheme organizes baryons in a two-dimensional space ( $I_3 - Y$ );  $Y$  (hypercharge) and  $I_3$   
 314 (isospin) are quantum numbers related by the Gell-Mann-Nishijima formula [15, 16]:

$$Q = I_3 + \frac{Y}{2} \quad (2.2)$$

315 where  $Y = B + S + C + T + B'$  are the quantum numbers listed in table 2.4. Baryon  
 316 number is conserved in SI and EI which means that single quarks cannot be created  
 317 but in pairs  $q - \bar{q}$ .

318

319 There are six quark flavors organized in three generations (see table 2.1) following a  
 320 mass hierarchy which, again, implies that higher generations decay to first generation

321 quarks.

	Quarks			$T_3$	$Y_W$	Leptons			$T_3$	$Y_W$
Doublets	$(\frac{u}{d'})_L$	$(\frac{c}{s'})_L$	$(\frac{t}{b'})_L$	$(\frac{1/2}{-1/2})$	1/3	$(\nu_e)_L$	$(\nu_\mu)_L$	$(\nu_\tau)_L$	$(\frac{1/2}{-1/2})$	-1
Singlets	$u_R$	$c_R$	$t_R$	0	4/3	$\nu_{eR}$	$\nu_{\mu R}$	$\nu_{\tau R}$	0	-2

**Table 2.5:** Fermion weak isospin and weak hypercharge multiplets. Weak hypercharge is calculated through the Gell-Mann-Nishijima formula 2.2 but using the weak isospin and charge for quarks.

322

323 Isospin doublets of quarks are also defined (see table 2.5) and as for neutrinos, the  
 324 mass eigenstates are not the same as the WI eigenstates which means that members of  
 325 different quark generations are connected by the WI mediator; thus, up-type quarks  
 326 are coupled not to down-type quarks directly but to a superposition of down-type  
 327 quarks ( $q'_d$ ) via WI according to:

$$q'_d = V_{CKM} q_d$$

328

$$\begin{pmatrix} d' \\ s' \\ b' \end{pmatrix} = \begin{pmatrix} V_{ud} & V_{us} & V_{ub} \\ V_{cd} & V_{cs} & V_{cb} \\ V_{td} & V_{ts} & V_{tb} \end{pmatrix} \begin{pmatrix} d \\ s \\ b \end{pmatrix} \quad (2.3)$$

329 where  $V_{CKM}$  is known as Cabibbo-Kobayashi-Maskawa (CKM) mixing matrix [17,18].  
 330 The weak decays of quarks are represented in the diagram of figure 2.2; again the  
 331 CKM matrix plays a central role since it contains the probabilities for the different  
 332 quark decay channels, in particular, note that quark decays are greatly favored be-  
 333 tween generation members.

334

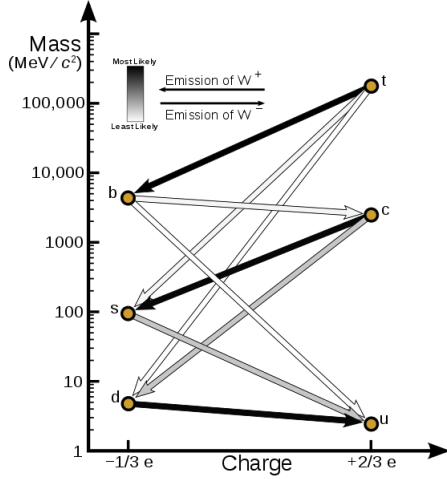


**Figure 2.2:** Transformations between quarks through the exchange of a WI. Higher generations quarks decay to first generation quarks by emitting a W boson. The arrow color indicates the likelihood of the transition according to the grey scale in the top left side which represent the CKM matrix parameters [19].

335 CKM matrix is a  $3 \times 3$  unitary matrix parametrized by three mixing angles and  
 336 the *CP-mixing phase*; the latter is the parameter responsible for the Charge-Parity  
 337 symmetry violation (CP-violation) in the SM. The fact that the b quark decays almost  
 338 all the times to a top quark is exploited in this thesis when making the selection of  
 339 the signal events by requiring the presence of a jet tagged as a jet coming from a  
 340 b quark in the final state. The effect of the *CP-mixing phase* on the cross section of  
 341 associated production of Higgs boson and a single top process is also explored in this  
 342 thesis.

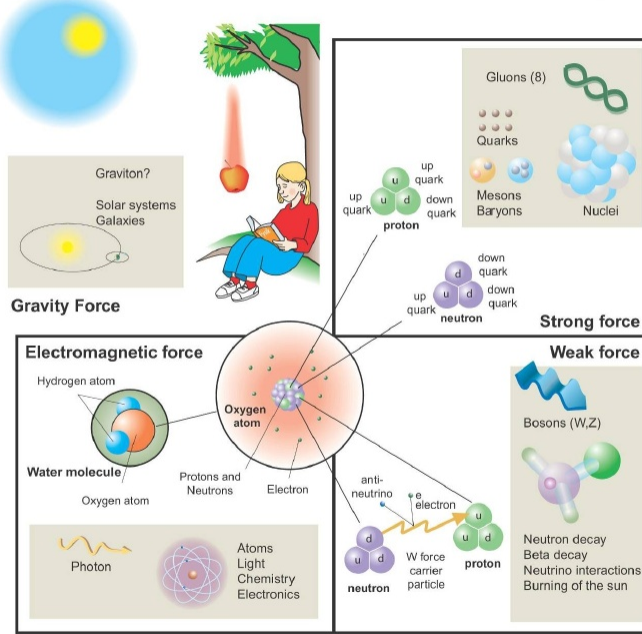
### 343 2.2.2 Fundamental interactions

344 Even though there are many manifestations of force in nature, like the ones repre-  
 345 sented in figure 2.3, we can classify all of them into one of four fundamental interac-  
 346 tions:

- 347 • *Electromagnetic interaction (EI)* affects particles that are “electrically charged,”

## Fundamental interactions.

Illustration: Typoform



Summer School KPI 15 August 2009

**Figure 2.3:** Fundamental interactions in nature. Despite the many manifestations of forces in nature, we can track all of them back to one of the fundamental interactions. The most common forces are gravity and electromagnetic given that all of us are subject and experience them in everyday life.

348 like electrons and protons. It is described by QED combining quantum mechan-  
 349 ics, special relativity and electromagnetism in order to explain how particles  
 350 with electric charge interact through the exchange of photons, therefore, one  
 351 says that “Electromagnetic Force” is mediated by “photons”. Figure 2.4a. shows  
 352 a graphical representation, known as “feynman diagram”, of electron-electron  
 353 scattering.

- 354 • *Strong interaction (SI)* described by Quantum Chromodynamics (QCD). Hadrons  
 355 like proton and neutron have internal structure given that they are composed  
 356 of two or more valence quarks<sup>5</sup>. Quarks have fractional electric charge which  
 357 means that they are subject to electromagnetic interaction and in the case of the

<sup>5</sup> particles made of four and five quarks are exotic states not so common.

358 proton they should break apart due to electrostatic repulsion; however, quarks  
 359 are held together inside the hadrons against their electrostatic repulsion by the  
 360 “Strong Force” through the exchange of “gluons.” The analog to the electric  
 361 charge is the “color charge”. Electrons and photons are elementary particles  
 362 as quarks but they don’t carry color charge, therefore they are not subject to  
 363 SI. The feynman diagram for gluon exchange between quarks is shown in figure  
 364 2.4b.

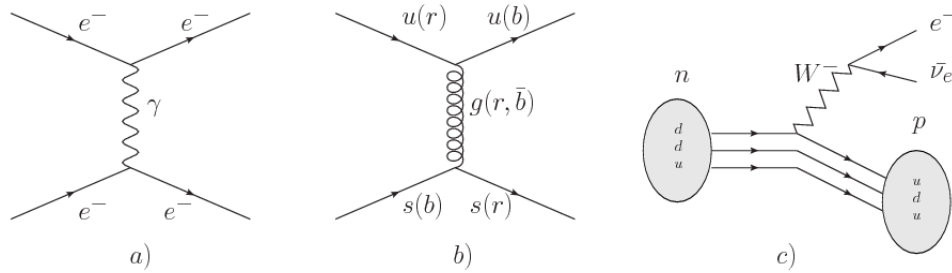


**Figure 2.4:** Feynman diagrams representing the interactions in SM; a) EI:  $e^-$ - $e^-$  scattering; b) SI: gluon exchange between quarks ; c) WI:  $\beta$ -decay

365     • *Weak interaction (WI)* described by the weak theory (WT), is responsible, for  
 366 instance, for the radioactive decay in atoms and proton-proton (pp) fusion  
 367 within the sun. Quarks and leptons are the particles affected by the weak  
 368 interaction; they possess a property called “flavor charge” (see 2.2.1) which can  
 369 be changed by emitting or absorbing one weak force mediator. There are three  
 370 mediators of the “weak force” known as “Z” boson in the case of electrically  
 371 neutral changes and “ $W^\pm$ ” bosons in the case of electrically charged changes.  
 372 The “weak isospin” is the WI analog to electric charge in EI, and color charge  
 373 in SI, and defines how quarks and leptons are affected by the weak force. Figure  
 374 2.4c. shows the feynman diagram of  $\beta$ -decay where a newtron (n) is transformed  
 375 in a proton (p) by emmiting a  $W^-$  particle. Since this thesis is in the frame  
 376 of the electroweak interaction, a more detailed description of it will be given in

377 section 2.3

- 378 • *Gravitational interaction (GI)* described by General Theory of Relativity (GR).  
 379 It is responsible for the structure of galaxies and black holes as well as the  
 380 expansion of the universe. As a classical theory, in the sense that it can be for-  
 381 mulated without even appeal to the concept of quantization, it implies that the  
 382 spacetime is a continuum and predictions can be made without limitation to the  
 383 precision of the measurement tools. The latter represent a direct contradic-  
 384 tion of the quantum mechanics principles. Gravity is deterministic while quantum  
 385 mechanics is probabilistic; despite that, efforts to develop a quantum theory of  
 386 gravity have predicted the “graviton” as mediator of the Gravitational force<sup>6</sup>.

Interaction	Acts on	Relative strength	Range (m)	Mediators
Electromagnetic (QED)	Electrically charged particles	$10^{-2}$	Infinite	Photon
Strong (QCD)	Quarks and gluons	1	$10^{-15}$	Gluon
Weak (WI)	Leptons and quarks	$10^{-6}$	$10^{-18}$	$W^\pm, Z$
Gravitational (GI)	Massive particles	$10^{-39}$	Infinite	Graviton

**Table 2.6:** Fundamental interactions features [20].

387

388 Table 2.6 summarizes the main features of the fundamental interactions. The rela-  
 389 tive strength of the fundamental forces reveals the meaning of strong and weak; in  
 390 a context where the relative strength of the SI is 1, the EI is about hundred times  
 391 weaker and WI is about million times weaker than the SI. A good description on  
 392 how the relative strength and range of the fundamental interactions are calculated  
 393 can be found in references [20, 21]. In the everyday life, only EI and GI are explicitly  
 394 experienced due to the range of these interactions; i.e., at the human scale distances

---

<sup>6</sup> Actually a wide variety of theories have been developed in an attempt to describe gravity; some famous examples are string theory and supergravity.

395 only EI and GI have appreciable effects, in contrast to SI which at distances greater  
 396 than  $10^{-15}$ m become negligible.

397

398 QED was built successfully on the basis of the classical electrodynamics theory (CED)  
 399 of Maxwell and Lorentz, following theoretical and experimental requirements imposed  
 400 by

- 401     • lorentz invariance: independence on the reference frame.
- 402     • locallity: interacting fields are evaluated at the same space-time point to avoid  
     403       action at a distance.
- 404     • renormalizability: physical predictions are finite and well defined
- 405     • particle spectrum, symmetries and conservation laws already known must emerge  
     406       from the theory.
- 407     • gauge invariance.

408 The gauge invariance requirement reflects the fact that the fundamental fields cannot  
 409 be directly measured but associated fields which are the observables. Electric (“**E**”)  
 410 and magnetic (“**B**”) fields in CED are associated with the electric scalar potential  
 411 “**V**” and the vector potential “**A**”. In particular, **E** can be obtained by measuring  
 412 the change in the space of the scalar potential ( $\Delta V$ ); however, two scalar potentials  
 413 differing by a constant “f” correspond to the same electric field. The same happens in  
 414 the case of the vector potential “**A**”; thus, different configurations of the associated  
 415 fields result in the same set of values of the observables. The freedom in choosing  
 416 one particular configuration is known as “gauge freedom”; the transformation law con-  
 417 necting two configurations is known as “gauge transformation” and the fact that the

418 observables are not affected by a gauge transformation is called “gauge invariance”.

419

420 When the gauge transformation:

$$\begin{aligned} \mathbf{A} &\rightarrow \mathbf{A} - \Delta f \\ V &\rightarrow V - \frac{\partial f}{\partial t} \end{aligned} \tag{2.4}$$

421 is applied to Maxwell equations, they are still satisfied and the fields remain invariant.

422 Thus, CED is invariant under gauge transformations and is called a “gauge theory”.

423 The set of all gauge transformations form the “symmetry group” of the theory, which

424 according to the group theory, has a set of “group generators”. The number of group

425 generators determine the number of “gauge fields” of the theory.

426

427 As mentioned in the first lines of section 2.2, QED has one symmetry group ( $U(1)$ )

428 with one group generator (the  $Q$  operator) and one gauge field (the electromagnetic

429 field  $A^\mu$ ). In CED there is not a clear definition, beyond the historical convention, of

430 which fields are the fundamental and which are the associated, but in QED it is clear

431 that the fundamental field is  $A^\mu$ . When a gauge theory is quantized, the gauge field

432 is quantized and its quanta is called “gauge boson”. The word boson characterizes

433 particles with integer spin which obvey Bose-einstein statistics.

434

435 As will be detailed in section 2.3, interactions between particles in a system can be

436 obtained by considering first the Lagrangian density of free particles in the system,

437 which of course is incomplete because the interaction terms have been left out, and

438 demanding global phase transformation invariance. Global phase transformation in-

439 variance means that a gauge transformation is performed identically to every point  
 440 in the space<sup>7</sup> and the Lagrangian remains invariant. Then, the global transformation  
 441 is promoted to a local phase transformation (this time the gauge transformation de-  
 442 pends on the position in space) and again invariance is required.

443

444 Due to the space dependence of the local tranformation, the Lagrangian density is  
 445 not invariant anymore. In order to restate the gauge invariance, the gauge covariant  
 446 derivative is introduced in the Lagrangian and with it the gauge field responsible for  
 447 the interaction between particles in the system. The new Lagrangian density is gauge  
 448 invariant, includes the interaction terms needed to account for the interactions and  
 449 provides a way to explain the interaction between particles through the exchange of  
 450 the gauge boson.

451 This recipe was used to build QED and the theories that aim to explain the funda-  
 452 mental interactions.

### 453 **2.2.3 Gauge bosons**

454 The importance of the gauge bosons comes from the fact that they are the force  
 455 mediators or force carriers. The features of the gauge bosons reflect those of the  
 456 fields they represent and they are extracted from the Lagrangian density used to  
 457 describe the interactions. In section 2.3, it will be shown how the gauge bosons of the  
 458 EI and WI emerge from the electroweak Lagrangian. The SI gauge bosons features  
 459 are also extracted from the SI Lagrangian but it is not detailed in this document. The  
 460 main features of the SM gauge bosons will be briefly presented below and summarized  
 461 in table 2.7.

---

<sup>7</sup> Here space corresponds to the 4-dimensional space i.e. space-time.

- 462     • **Photon.** EI occurs when the photon couples to (is exchanged between) particles  
 463       carrying electric charge; however, the photon itself does not carry electric charge,  
 464       therefore, there is no coupling between photons. Given that the photon is  
 465       massless the EI is of infinite range, i.e., electrically charged particles interact  
 466       even if they are located far away one from each other; this also implies that  
 467       photons always move with the speed of light.
- 468     • **Gluon.** SI is mediated by gluons which, same as photons, are massless. They  
 469       carry one unit of color charge and one unit of anticolor charge which means that  
 470       gluons couple to other gluons. As a result, the range of the SI is not infinite  
 471       but very short due to the attraction between gluons, giving rise to the “color  
 472       confinement” which explains why color charged particles cannot be isolated but  
 473       live within composited particles, like quarks inside protons.
- 474     • **W, Z.** The WI mediators,  $W^\pm$  and Z, are massive which explains their short-  
 475       range. Given that the WI is the only interaction that can change the flavor  
 476       of the interacting particles, the W boson is the responsible for the nuclear  
 477       transmutation where a neutron is converted in a proton or vice versa with the  
 478       involvement of an electron and a neutrino (see figure 2.4c). The Z boson is the  
 479       responsible of the neutral weak processes like neutrino elastic scattering where  
 480       no electric charge but momentum transference is involved. WI gauge bosons  
 481       carry isospin charge which makes possible the interaction between them.

Interaction	Mediator	Electric charge (e)	Color charge	Weak Isospin	mass (GeV/c <sup>2</sup> )
Electromagnetic	Photon ( $\gamma$ )	0	No	0	0
Strong	Gluon (g)	0	Yes -octet	No	0
Weak	$W^\pm$	$\pm 1$	No	$\pm 1$	$80.385 \pm 0.015$
	Z	0	No	0	$91.188 \pm 0.002$

Table 2.7: SM gauge bosons main features [9].

## 483 2.3 Electroweak unification and the Higgs

### 484 mechanism

485 Physicists dream of building a theory that contains all the interactions in one single  
 486 interaction, i.e., showing that at some scale in energy all the four fundamental in-  
 487 teractions are unified and only one interaction emerges in a “Theory of everything”.  
 488 The first sign of the feasibility of such unification comes from success in the con-  
 489 struction of the CED. Einstein spent years trying to reach that dream, which by  
 490 1920 only involved electromagnetism and gravity, with no success; however, a new  
 491 partial unification was achieved in the 1960’s, when S.Glashow [22], A.Salam [23] and  
 492 S.Weinberg [24] independently proposed that electromagnetic and weak interactions  
 493 are two manifestations of a more general interaction called “electroweak interaction  
 494 (EWT)”. Both, QCD and EWT, were developed in parallel and following the useful  
 495 prescription provided by QED and the gauge invariance principles.

496

497 The theory of weak interactions was capable of explaining the  $\beta$ -decay and in general  
 498 the processes mediated by  $W^\pm$  bosons. However, there were some processes like the  
 499 “ $\nu_\mu - e$  scattering” which would require the exchange of two W bosons (see figure 2.5  
 500 top diagrams) giving rise to divergent loop integrals and then non finite predictions.  
 501 By including neutral currents involving fermions via the exchange of neutral bosons  
 502 Z, those divergences are compensated and the predictions become realistic.

503

504 Neutral weak interaction vertices conserve flavor in the same way as the electromag-  
 505 netic vertices do, but additionally, the Z boson can couple to neutrinos which implies  
 506 that processes involving charged fermions can proceed through EI or WI but processes  
 507 involving neutrinos can proceed only through WI.

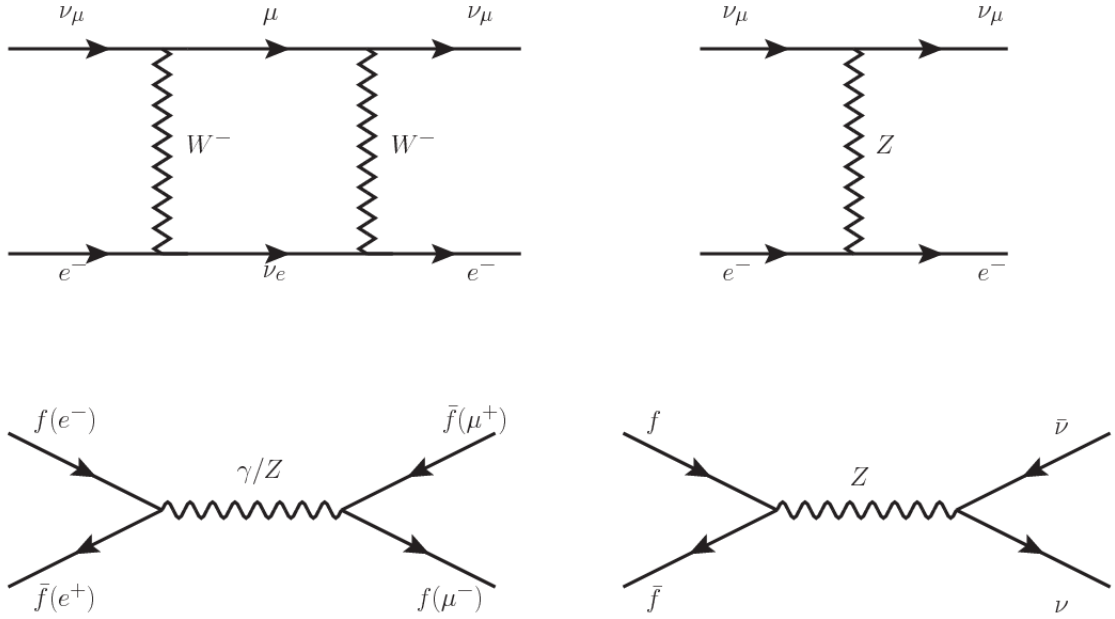


**Figure 2.5:** Top:  $\nu_\mu - e^-$  scattering going through charged currents (left) and neutral currents (right). Bottom: neutral current processes for charged fermions (left) and involving neutrinos (right). While neutral current processes involving only charged fermions can proceed through EI or WI, those involving neutrinos can only proceed via WI.

508

509 The prescription to build a gauge theory of the WI consists of proposing a free field  
 510 Lagrangian density that includes the particles involved; next, by requesting invari-  
 511 ance under global phase transformations first and generalizing to local phase trans-  
 512 formations invariance later, the conserved currents are identified and interactions are  
 513 generated by introducing gauge fields. Given that the goal is to include the EI and  
 514 WI in a single theory, the group symmetry considered should be a combination of  
 515  $SU(2)_L$  and  $U(1)_{em}$ , however the latter cannot be used directly because the EI treats  
 516 left and right-handed particles indistinctly in contrast to the former. Fortunately, the  
 517 weak hypercharge, which is a combination of the weak isospin and the electric charge  
 518 (eqn 2.2) is suitable to be used since it is conserved by the EI and WI. Thus, the  
 519 symmetry group to be considered is

$$G \equiv SU(2)_L \otimes U(1)_Y \quad (2.5)$$

520 The following treatment applies to any of the fermion generations, but for simplicity  
 521 the first generation of leptons will be considered [5, 6, 25, 26].

522

523 Given the first generation of leptons

$$\psi_1 = \begin{pmatrix} \nu_e \\ e^- \end{pmatrix}_L, \quad \psi_2 = \nu_{eR}, \quad \psi_3 = e_R^- \quad (2.6)$$

524 the charged fermionic currents are given by

$$J_\mu \equiv J_\mu^+ = \bar{\nu}_{eL} \gamma_\mu e_L, \quad J_\mu^\dagger \equiv J_\mu^- = \bar{e}_L \gamma_\mu \nu_{eL} \quad (2.7)$$

525 and the free Lagrangian is given by

$$\mathcal{L}_0 = \sum_{j=1}^3 i\bar{\psi}_j(x) \gamma^\mu \partial_\mu \psi_j(x). \quad (2.8)$$

526 Mass terms are included directly in the QED and QCD free Lagrangians since they  
 527 preserve the invariance under the symmetry transformations involved which treat  
 528 left-handed and right-handed similarly, however mass terms of the form

$$m_W^2 W_\mu^\dagger(x) W^\mu(x) + \frac{1}{2} m_Z^2 Z_\mu(x) Z^\mu(x) - m_e \bar{\psi}_e(x) \psi_e(x) \quad (2.9)$$

529 which represent the mass of  $W^\pm$ , Z and electrons, are not invariant under G trans-  
 530 formations, therefore the gauge fields described by the EWI are in principle massless.

531

532 Experiments have shown that the gauge fields are not massless; however, they have

533 to acquire mass through a mechanism compatible with the gauge invariance; that  
 534 mechanism is known as the “Higgs mechanism” and will be considered later in this  
 535 section. The global transformations in the combined symmetry group  $G$  can be  
 536 written as

$$\begin{aligned}\psi_1(x) &\xrightarrow{G} \psi'_1(x) \equiv U_Y U_L \psi_1(x), \\ \psi_2(x) &\xrightarrow{G} \psi'_2(x) \equiv U_Y \psi_2(x), \\ \psi_3(x) &\xrightarrow{G} \psi'_3(x) \equiv U_Y \psi_3(x)\end{aligned}\tag{2.10}$$

537 where  $U_L$  represent the  $SU(2)_L$  transformation acting only on the weak isospin dou-  
 538 blet and  $U_Y$  represent the  $U(1)_Y$  transformation acting on all the weak isospin mul-  
 539 tiplets. Explicitly

$$U_L \equiv \exp\left(i\frac{\sigma_i}{2}\alpha^i\right), \quad U_Y \equiv \exp(iy_i\beta) \quad (i = 1, 2, 3)\tag{2.11}$$

540 with  $\sigma_i$  the Pauli matrices and  $y_i$  the weak hypercharges. In order to promote the  
 541 transformations from global to local while keeping the invariance, it is required that  
 542  $\alpha^i = \alpha^i(x)$ ,  $\beta = \beta(x)$  and the replacement of the ordinary derivatives by the covariant  
 543 derivatives

$$\begin{aligned}D_\mu \psi_1(x) &\equiv [\partial_\mu + ig\sigma_i W_\mu^i(x)/2 + ig'y_1 B_\mu(x)] \psi_1(x) \\ D_\mu \psi_2(x) &\equiv [\partial_\mu + ig'y_2 B_\mu(x)] \psi_2(x) \\ D_\mu \psi_3(x) &\equiv [\partial_\mu + ig'y_3 B_\mu(x)] \psi_3(x)\end{aligned}\tag{2.12}$$

544 introducing in this way four gauge fields,  $W_\mu^i(x)$  and  $B_\mu(x)$ , in the process. The  
 545 covariant derivatives (eqn 2.12) are required to transform in the same way as fermion  
 546 fields  $\psi_i(x)$  themselves, therefore, the gauge fields transform as:

$$\begin{aligned} B_\mu(x) &\xrightarrow{G} B'_\mu(x) \equiv B_\mu(x) - \frac{1}{g'} \partial_\mu \beta(x) \\ W_\mu^i(x) &\xrightarrow{G} W_\mu^{i\prime}(x) \equiv W_\mu^i(x) - \frac{i}{g} \partial_\mu \alpha_i(x) - \varepsilon_{ijk} \alpha_i(x) W_\mu^j(x). \end{aligned} \quad (2.13)$$

547 The G invariant version of the Lagrangian density 2.8 can be written as

$$\mathcal{L}_0 = \sum_{j=1}^3 i \bar{\psi}_j(x) \gamma^\mu D_\mu \psi_j(x) \quad (2.14)$$

548 where free massless fermion and gauge fields and fermion-gauge boson interactions  
 549 are included. The EWI Lagrangian density must additionally include kinetic terms  
 550 for the gauge fields ( $\mathcal{L}_G$ ) which are built from the field strengths, according to

$$B_{\mu\nu}(x) \equiv \partial_\mu B_\nu - \partial_\nu B_\mu \quad (2.15)$$

$$W_{\mu\nu}^i(x) \equiv \partial_\mu W_\nu^i(x) - \partial_\nu W_\mu^i(x) - g \varepsilon^{ijk} W_\mu^j W_\nu^k \quad (2.16)$$

551 the last term in eqn. 2.16 is added in order to hold the gauge invariance; therefore,

$$\mathcal{L}_G = -\frac{1}{4} B_{\mu\nu}(x) B^{\mu\nu}(x) - \frac{1}{4} W_{\mu\nu}^i(x) W_i^{\mu\nu}(x) \quad (2.17)$$

552 which contains not only the free gauge fields contributions, but also the gauge fields  
 553 self-interactions and interactions among them.

555 The three weak isospin conserved currents resulting from the  $SU(2)_L$  symmetry are  
 556 given by

$$J_\mu^i(x) = \frac{1}{2} \bar{\psi}_1(x) \gamma_\mu \sigma^i \psi_1(x) \quad (2.18)$$

557 while the weak hypercharge conserved current resulting from the  $U(1)_Y$  symmetry is  
 558 given by

$$J_\mu^Y = \sum_{j=1}^3 \bar{\psi}_j(x) \gamma_\mu y_j \psi_j(x) \quad (2.19)$$

559 In order to evaluate the electroweak interactions modeled by an isovector field  $W_\mu^i$   
 560 which couples to isospin currents  $J_\mu^i$  with strength  $g$  and additionally the singlet  
 561 field  $B_\mu$  which couples to the weak hypercharge current  $J_\mu^Y$  with strength  $g'/2$ . The  
 562 interaction Lagrangian density to be considered is

$$\mathcal{L}_I = -g J^{i\mu}(x) W_\mu^i(x) - \frac{g'}{2} J^{Y\mu}(x) B_\mu(x) \quad (2.20)$$

563 Note that the weak isospin currents are not the same as the charged fermionic currents  
 564 that were used to describe the WI (eqn 2.7), since the weak isospin eigenstates are  
 565 not the same as the mass eigenstates, but they are closely related

$$J_\mu = \frac{1}{2} (J_\mu^1 + i J_\mu^2), \quad J_\mu^\dagger = \frac{1}{2} (J_\mu^1 - i J_\mu^2). \quad (2.21)$$

566 The same happens with the gauge fields  $W_\mu^i$  which are related to the mass eigenstates  
 567  $W^\pm$  by

$$W_\mu^+ = \frac{1}{\sqrt{2}} (W_\mu^1 - i W_\mu^2), \quad W_\mu^- = \frac{1}{\sqrt{2}} (W_\mu^1 + i W_\mu^2). \quad (2.22)$$

568 The fact that there are three weak isospin conserved currents is an indication that in  
 569 addition to the charged fermionic currents, which couple charged to neutral leptons,  
 570 there should be a neutral fermionic current that does not involve electric charge  
 571 exchange; therefore, it couples neutral fermions or fermions of the same electric charge.  
 572 The third weak isospin current contains a term that is similar to the electromagnetic  
 573 current ( $j_\mu^{em}$ ), indicating that there is a relation between them and resembling the  
 574 Gell-Mann-Nishijima formula 2.2 adapted to electroweak interactions

$$Q = T_3 + \frac{Y_W}{2}. \quad (2.23)$$

575 Just as Q generates the  $U(1)_{em}$  symmetry, the weak hypercharge generates the  $U(1)_Y$   
 576 symmetry as said before. It is possible to write the relationship in terms of the currents  
 577 as

$$j_\mu^{em} = J_\mu^3 + \frac{1}{2}J_\mu^Y. \quad (2.24)$$

578 The neutral gauge fields  $W_\mu^3$  and  $B_\mu$  cannot be directly identified with the  $Z$  and the  
 579 photon fields since the photon interacts similarly with left and right-handed fermions;  
 580 however, they are related through a linear combination given by

$$\begin{aligned} A_\mu &= B_\mu \cos \theta_W + W_\mu^3 \sin \theta_W \\ Z_\mu &= -B_\mu \sin \theta_W + W_\mu^3 \cos \theta_W \end{aligned} \quad (2.25)$$

581 where  $\theta_W$  is known as the “Weinberg angle.” The interaction Lagrangian is now given

582 by

$$\mathcal{L}_I = -\frac{g}{\sqrt{2}}(J^\mu W_\mu^+ + J^{\mu\dagger} W_\mu^-) - \left(g \sin \theta_W J_\mu^3 + g' \cos \theta_W \frac{J_\mu^Y}{2}\right) A^\mu - \left(g \cos \theta_W J_\mu^3 - g' \sin \theta_W \frac{J_\mu^Y}{2}\right) Z^\mu \quad (2.26)$$

583 the first term is the weak charged current interaction, while the second term is the  
584 electromagnetic interaction under the condition

$$g \sin \theta_W = g' \cos \theta_W = e, \quad \frac{g'}{g} = \tan \theta_W \quad (2.27)$$

585 contained in the eqn.2.24; the third term is the neutral weak current.

586

587 Note that the neutral fields transformation given by the eqn. 2.25 can be written in  
588 terms of the coupling constants  $g$  and  $g'$  as:

$$A_\mu = \frac{g' W_\mu^3 + g B_\mu}{\sqrt{g^2 + g'^2}}, \quad Z_\mu = \frac{g W_\mu^3 - g' B_\mu}{\sqrt{g^2 + g'^2}} \quad (2.28)$$

589 So far, the Lagrangian density describing the non-massive EWI is:

$$\mathcal{L}_{nmEWI} = \mathcal{L}_0 + \mathcal{L}_G \quad (2.29)$$

590 where fermion and gauge fields have been considered massless because their regular  
591 mass terms are manifestly non invariant under G transformations; therefore, masses  
592 have to be generated in a gauge invariant way. The mechanism by which this goal is  
593 achieved is known as the “Higgs mechanism” and is closely connected to the concept  
594 of “spontaneous symmetry breaking.”

595 **2.3.1 Spontaneous symmetry breaking (SSB)**

596 Figure 2.6 left shows a steel nail (top) which is subject to an external force; the form  
 597 of the potential energy is also shown (bottom).

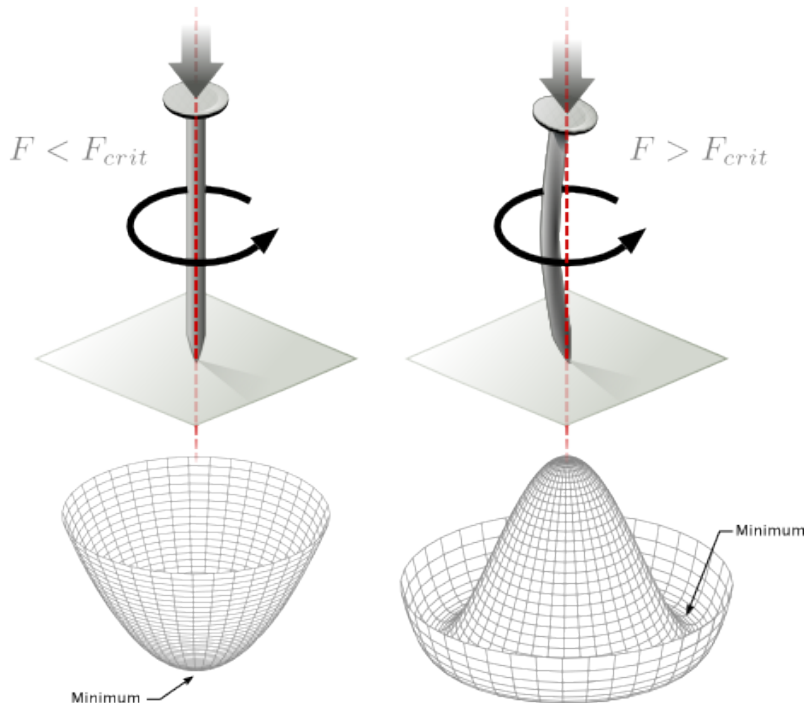


**Figure 2.6:** Spontaneous symmetry breaking mechanism. The steel nail, subject to an external force (top left), has rotational symmetry with respect to its axis. When the external force overcomes a critical value the nail buckles (top right) choosing a minimal energy state (ground state) and thus “*breaking spontaneously the rotational symmetry*”. The potential energy (bottom) changes but holds the rotational symmetry; however, an infinite number of asymmetric ground states are generated and circularly distributed in the bottom of the potential [27].

598

599 Before reaching the critical force value, the system has rotational symmetry with re-  
 600 spect to the nail axis; however, after the critical force value is reached the nail buckles  
 601 (top right). The form of the potential energy (bottom right) changes, preserving its  
 602 rotational symmetry although its minima does not exhibit that rotational symmetry  
 603 any longer. Right before the nail buckles there is no indication of the direction the

604 nail will bend because any of the directions are equivalent, but once the nail bends,  
 605 choosing a direction, an arbitrary minimal energy state (ground state) is selected and  
 606 it does not share the system's rotational symmetry. This mechanism for reaching an  
 607 asymmetric ground state is known as "*spontaneous symmetry breaking*".

608 The lesson from this analysis is that the way to introduce the SSB mechanism into a  
 609 system is by adding the appropriate potential to it.

610

611 Figure 2.7 shows a plot of the potential  $V(\phi)$  in the case of a scalar field  $\phi$

$$V(\phi) = \mu^2 \phi^\dagger \phi + \lambda (\phi^\dagger \phi)^2 \quad (2.30)$$

612 If  $\mu^2 > 0$  the potential has only one minimum at  $\phi = 0$  and describes a scalar field  
 613 with mass  $\mu$ . If  $\mu^2 < 0$  the potential has a local maximum at  $\phi = 0$  and two minima  
 614 at  $\phi = \pm\sqrt{-\mu^2/\lambda}$  which enables the SSB mechanism to work.

615

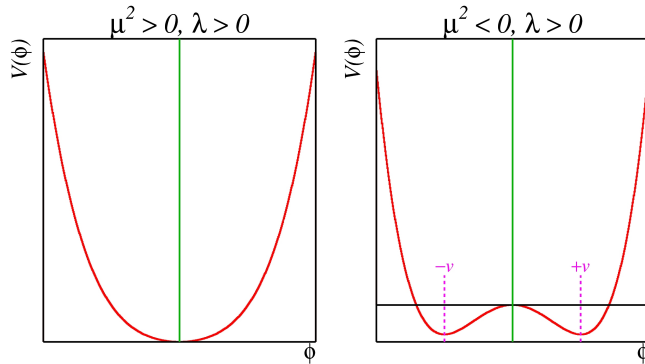


**Figure 2.7:** Shape of the potential  $V(\phi)$  for  $\lambda > 0$  and:  $\mu^2 > 0$  (left) and  $\mu^2 < 0$  (right). The case  $\mu^2 < 0$  corresponds to the potential suitable for introducing the SSB mechanism by choosing one of the two ground states which are connected via reflection symmetry. [27].

616 In the case of a complex scalar field  $\phi(x)$

$$\phi(x) = \frac{1}{\sqrt{2}}(\phi_1 + i\phi_2) \quad (2.31)$$

617 the Lagrangian (invariant under global  $U(1)$  transformations) is given by

$$\mathcal{L} = (\partial_\mu \phi)^\dagger (\partial^\mu \phi) - V(\phi), \quad V(\phi) = \mu^2 \phi^\dagger \phi + \lambda (\phi^\dagger \phi)^2 \quad (2.32)$$

618 where an appropriate potential has been added in order to introduce the SSB.

619

620 As seen in figure 2.8, the potential has now an infinite number of minima circularly  
 621 distributed along the  $\xi$ -direction which makes possible the occurrence of the SSB by  
 622 choosing an arbitrary ground state; for instance,  $\xi = 0$ , i.e.  $\phi_1 = v, \phi_2 = 0$

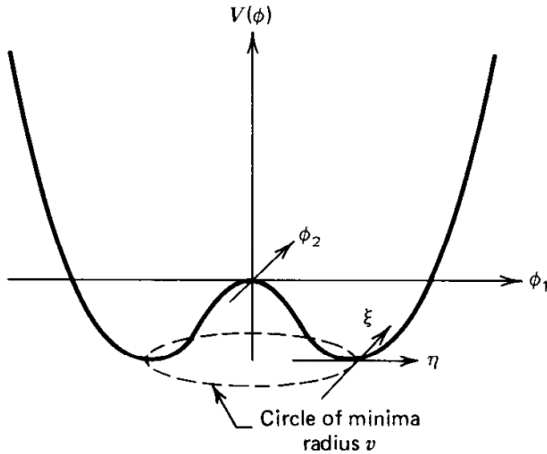


**Figure 2.8:** Potential for complex scalar field. There is a circle of minima of radius  $v$  along the  $\xi$ -direction [6].

$$\phi_0 = \frac{v}{\sqrt{2}} \exp(i\xi) \xrightarrow{SSB} \phi_0 = \frac{v}{\sqrt{2}} \quad (2.33)$$

623 As usual, excitations over the ground state are studied by making an expansion about

624 it; thus, the excitation can be parametrized as:

$$\phi(x) = \frac{1}{\sqrt{2}}(v + \eta(x) + i\xi(x)) \quad (2.34)$$

625 which when substituted into eqn. 2.32 produces a Lagrangian in terms of the new  
 626 fields  $\eta$  and  $\xi$

$$\mathcal{L}' = \frac{1}{2}(\partial_\mu\xi)^2 + \frac{1}{2}(\partial_\mu\eta)^2 + \mu^2\eta^2 - V(\phi_0) - \lambda v\eta(\eta^2 + \xi^2) - \frac{\lambda}{4}(\eta^2 + \xi^2)^2 \quad (2.35)$$

627 where the last two terms represent the interactions and self-interaction between the  
 628 two fields  $\eta$  and  $\xi$ . The particular feature of the SSB mechanism is revealed when  
 629 looking to the first three terms of  $\mathcal{L}'$ . Before the SSB, only the massless  $\phi$  field is  
 630 present in the system; after the SSB there are two fields of which the  $\eta$ -field has  
 631 acquired mass  $m_\eta = \sqrt{-2\mu^2}$  while the  $\xi$ -field is still massless (see figure 2.9).

632

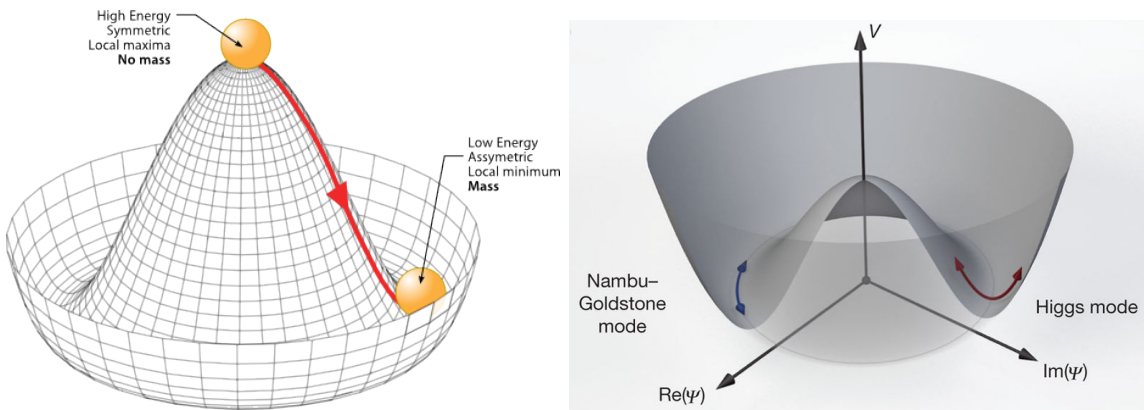


**Figure 2.9:** SSB mechanism for a complex scalar field [27, 28].

633 Thus, the SSB mechanism serves as a method to generate mass but as a side effect a  
 634 massless field is introduced in the system. This fact is known as the Goldstone theorem

and states that a massless scalar field appears in the system for each continuous symmetry spontaneously broken. Another version of the Goldstone theorem states that “*if a Lagrangian is invariant under a continuous symmetry group  $G$ , but the vacuum is only invariant under a subgroup  $H \subset G$ , then there must exist as many massless spin-0 particles (Nambu-Goldstone bosons) as broken generators.*” [26] The Nambu-Goldstone boson can be understood considering that the potential in the  $\xi$ -direction is flat so excitations in that direction are not energy consuming and thus represent a massless state.

### 2.3.2 Higgs mechanism

When the SSB mechanism is introduced in the formulation of the EWI in an attempt to generate the mass of the so far massless gauge bosons and fermions, an interesting effect is revealed. In order to keep the  $G$  symmetry group invariance and generate the mass of the EW gauge bosons, a  $G$  invariant Lagrangian density ( $\mathcal{L}_S$ ) has to be added to the non massive EWI Lagrangian (eqn. 2.29)

$$\mathcal{L}_S = (D_\mu \phi)^\dagger (D^\mu \phi) - \mu^2 \phi^\dagger \phi - \lambda (\phi^\dagger \phi)^2, \quad \lambda > 0, \mu^2 < 0 \quad (2.36)$$

$$D_\mu \phi = \left( i\partial_\mu - g \frac{\sigma_i}{2} W_\mu^i - g' \frac{Y}{2} B_\mu \right) \phi \quad (2.37)$$

$\phi$  has to be an isospin doublet of complex scalar fields so it preserves the  $G$  invariance; thus  $\phi$  can be defined as:

$$\phi = \begin{pmatrix} \phi^+ \\ \phi^0 \end{pmatrix} \equiv \frac{1}{\sqrt{2}} \begin{pmatrix} \phi_1 + i\phi_2 \\ \phi_3 + i\phi_4 \end{pmatrix}. \quad (2.38)$$

The minima of the potential are defined by

$$\phi^\dagger \phi = \frac{1}{2}(\phi_1^2 + \phi_2^2 + \phi_3^2 + \phi_4^2) = -\frac{\mu^2}{2\lambda}. \quad (2.39)$$

652 The choice of the ground state is critical. By choosing a ground state, invariant under  
 653  $U(1)_{em}$  gauge symmetry, the photon will remain massless and the  $W^\pm$  and  $Z$  bosons  
 654 masses will be generated which is exactly what is needed. In that sense, the best  
 655 choice corresponds to a weak isospin doublet with  $T_3 = -1/2$ ,  $Y_W = 1$  and  $Q = 0$   
 656 which defines a ground state with  $\phi_1 = \phi_2 = \phi_4$  and  $\phi_3 = v$ :

$$\phi_0 \equiv \frac{1}{\sqrt{2}} \begin{pmatrix} 0 \\ v \end{pmatrix}, \quad v^2 \equiv -\frac{\mu^2}{\lambda}. \quad (2.40)$$

657 where the vacuum expectation value  $v$  is fixed by the Fermi coupling  $G_F$  according  
 658 to  $v = (\sqrt{2}G_F)^{1/2} \approx 246$  GeV.

659

660 The G symmetry has been broken and three Nambu-Goldstone bosons will appear.  
 661 The next step is to expand  $\phi$  about the chosen ground state as:

$$\phi(x) = \frac{1}{\sqrt{2}} \exp\left(\frac{i}{v} \sigma_i \theta^i(x)\right) \begin{pmatrix} 0 \\ v + H(x) \end{pmatrix} \approx \frac{1}{\sqrt{2}} \begin{pmatrix} \theta_1(x) + i\theta_2(x) \\ v + H(x) - i\theta_3(x) \end{pmatrix} \quad (2.41)$$

662 to describe fluctuations from the ground state  $\phi_0$ . The fields  $\theta_i(x)$  represent the  
 663 Nambu-Goldstone bosons while  $H(x)$  is known as “higgs field.” The fundamental  
 664 feature of the parametrization used is that the dependence on the  $\theta_i(x)$  fields is  
 665 factored out in a global phase that can be eliminated by taking the physical “unitary  
 666 gauge”  $\theta_i(x) = 0$ . Therefore the expansion about the ground state is given by:

$$\phi(x) \frac{1}{\sqrt{2}} \begin{pmatrix} 0 \\ v + H(x) \end{pmatrix} \quad (2.42)$$

667 which when substituted into  $\mathcal{L}_S$  (eqn. 2.36) results in a Lagrangian containing the now  
 668 massive three gauge bosons  $W^\pm, Z$ , one massless gauge boson (photon) and the new  
 669 Higgs field ( $H$ ). The three degrees of freedom corresponding to the Nambu-Goldstone  
 670 bosons are now integrated into the massive gauge bosons as their longitudinal po-  
 671 larizations which were not available when they were massless particles. The effect  
 672 by which vector boson fields acquire mass after an spontaneous symmetry breaking,  
 673 but without an explicit gauge invariance breaking is known as the “*Higgs mechanism*”.

674

675 The mechanism was proposed by three independent groups: F.Englert and R.Brout  
 676 in August 1964 [29], P.Higgs in October 1964 [30] and G.Guralnik, C.Hagen and  
 677 T.Kibble in November 1964 [31]; however, its importance was not realized until  
 678 S.Glashow [22], A.Salam [23] and S.Weinberg [24], independently, proposed that elec-  
 679 tromagnetic and weak interactions are two manifestations of a more general interac-  
 680 tion called “electroweak interaction” in 1967.

### 681 2.3.3 Masses of the gauge bosons

682 The mass of the gauge bosons is extracted by evaluating the kinetic part of Lagrangian  
 683  $\mathcal{L}_S$  in the ground state (known also as the vacuum expectation value), i.e.,

$$\left| \left( \partial_\mu - ig \frac{\sigma_i}{2} W_\mu^i - i \frac{g'}{2} B_\mu \right) \phi_0 \right|^2 = \left( \frac{1}{2} v g \right)^2 W_\mu^+ W^{-\mu} + \frac{1}{8} v^2 (W_\mu^3, B_\mu) \begin{pmatrix} g^2 & -gg' \\ -gg' & g'^2 \end{pmatrix} \begin{pmatrix} W^{3\mu} \\ B^\mu \end{pmatrix} \quad (2.43)$$

684 comparing with the typical mass term for a charged boson  $M_W^2 W^+ W^-$

$$M_W = \frac{1}{2} v g. \quad (2.44)$$

The second term in the right side of the eqn.2.43 comprises the masses of the neutral

bosons, but it needs to be written in terms of the gauge fields  $Z_\mu$  and  $A_\mu$  in order to be compared to the typical mass terms for neutral bosons, therefore using eqn. 2.28

$$\begin{aligned} \frac{1}{8}v^2[g^2(W_\mu^3)^2 - 2gg'W_\mu^3B^\mu + g'^2B_\mu^2] &= \frac{1}{8}v^2[gW_\mu^3 - g'B_\mu]^2 + 0[g'W_\mu^3 + gB_\mu]^2 \\ &= \frac{1}{8}v^2[\sqrt{g^2 + g'^2}Z_\mu]^2 + 0[\sqrt{g^2 + g'^2}A_\mu]^2 \end{aligned} \quad (2.45)$$

685 and then

$$M_Z = \frac{1}{2}v\sqrt{g^2 + g'^2}, \quad M_A = 0 \quad (2.46)$$

### 686 2.3.4 Masses of the fermions

687 The lepton mass terms can be generated by introducing a gauge invariant Lagrangian  
688 term describing the Yukawa coupling between the lepton field and the Higgs field

$$\mathcal{L}_{Yl} = -G_l \left[ (\bar{\nu}_l, \bar{l})_L \begin{pmatrix} \phi^+ \\ \phi^0 \end{pmatrix} l_R + \bar{l}_R (\phi^-, \bar{\phi}^0) \begin{pmatrix} \nu_l \\ l \end{pmatrix}_L \right], \quad l = e, \mu, \tau. \quad (2.47)$$

689 After the SSB and replacing the usual field expansion about the ground state (eqn.2.40)  
690 into  $\mathcal{L}_{Yl}$ , the mass term arises

$$\mathcal{L}_{Yl} = -m_l(\bar{l}_L l_R + \bar{l}_R l_L) - \frac{m_l}{v}(\bar{l}_L l_R + \bar{l}_R l_L)H = -m_l \bar{l} \left( 1 + \frac{H}{v} \right) \quad (2.48)$$

691

$$m_l = \frac{G_l}{\sqrt{2}}v \quad (2.49)$$

692 where the additional term represents the lepton-Higgs interaction. The quark masses  
693 are generated in a similar way as lepton masses but for the upper member of the

694 quark doublet a different Higgs doublet is needed:

$$\phi_c = -i\sigma_2\phi^* = \begin{pmatrix} -\bar{\phi}^0 \\ \phi^- \end{pmatrix}. \quad (2.50)$$

695 Additionally, given that the quark isospin doublets are not constructed in terms of  
 696 the mass eigenstates but in terms of the flavor eigenstates, as shown in table 2.5, the  
 697 coupling parameters will be related to the CKM matrix elements; thus the quark  
 698 Lagrangian is given by:

$$\mathcal{L}_{Yq} = -G_d^{i,j}(\bar{u}_i, \bar{d}_i)_L \begin{pmatrix} \phi^+ \\ \phi^0 \end{pmatrix} d_{jR} - G_u^{i,j}(\bar{u}_i, \bar{d}_i)_L \begin{pmatrix} -\bar{\phi}^0 \\ \phi^- \end{pmatrix} u_{jR} + h.c. \quad (2.51)$$

699 with  $i,j=1,2,3$ . After SSB and expansion about the ground state, the diagonal form  
 700 of  $\mathcal{L}_{Yq}$  is:

$$\mathcal{L}_{Yq} = -m_d^i \bar{d}_i d_i \left( 1 + \frac{H}{v} \right) - m_u^i \bar{u}_i u_i \left( 1 + \frac{H}{v} \right) \quad (2.52)$$

701 Fermion masses depend on arbitrary couplings  $G_l$  and  $G_{u,d}$  and are not predicted by  
 702 the theory.

### 703 2.3.5 The Higgs field

704 After the characterization of the fermions and gauge bosons as well as their interac-  
 705 tions, it is necessary to characterize the Higgs field itself. The Lagrangian  $\mathcal{L}_S$  in eqn.  
 706 2.3.6 written in terms of the gauge bosons is given by

$$\mathcal{L}_S = \frac{1}{4}\lambda v^4 + \mathcal{L}_H + \mathcal{L}_{HV} \quad (2.53)$$

$$\mathcal{L}_H = \frac{1}{2}\partial_\mu H \partial^\mu H - \frac{1}{2}m_H^2 H^2 - \frac{1}{2v}m_H^2 H^3 - \frac{1}{8v^2}m_H^2 H^4 \quad (2.54)$$

$$\mathcal{L}_{HV} = m_H^2 W_\mu^+ W^{\mu-} \left( 1 + \frac{2}{v}H + \frac{2}{v^2}H^2 \right) + \frac{1}{2}m_Z^2 Z_\mu Z^\mu \left( 1 + \frac{2}{v}H + \frac{2}{v^2}H^2 \right) \quad (2.55)$$

709 The mass of the Higgs boson is deduced as usual from the mass term in the Lagrangian  
 710 resulting in:

$$m_H = \sqrt{-2\mu^2} = \sqrt{2\lambda}v \quad (2.56)$$

711 however, it is not predicted by the theory either. The experimental efforts to find  
 712 the Higgs boson, carried out by the “Compact Muon Solenoid (CMS)” experiment  
 713 and the “A Toroidal LHC AppartuS (ATLAS)” experiments at the “Large Hadron  
 714 Collider(LHC)”, gave great results by July of 2012 when the discovery of a new  
 715 particle compatible with the Higgs boson predicted by the electroweak theory [32, 33]  
 716 was announced. Although at the announcement time there were some reservations  
 717 about calling the new particle the “Higgs boson”, today this name is widely accepted.  
 718 The Higgs mass measurement, reported by both experiments [34], is in table 2.8.

Property	Value
Electric charge	0
Colour charge	0
Spin	0
Weak isospin	-1/2
Weak hypercharge	1
Parity	1
Mass (GeV/c <sup>2</sup> )	125.09±0.21 (stat.)±0.11 (syst.)

**Table 2.8:** Higgs boson properties. Higgs mass is not predicted by the theory and the value here corresponds to the experimental measurement.

719

### 720 2.3.6 Production of Higgs bosons at LHC

721 At LHC, Higgs boson is produced as a result of the collision of two counter-rotating  
 722 protons beams. A detailed description of the LHC machine will be presented in  
 723 chapter 3. “The total cross section” is a parameter that quantifies the number of pp  
 724 collisions that happen when a number of protons are fired at each other. Different  
 725 results can be obtained after a pp collision and for each one the “cross section” is

defined as the number of pp collisions that conclude in that particular result with respect to the number of protons fired at each other.

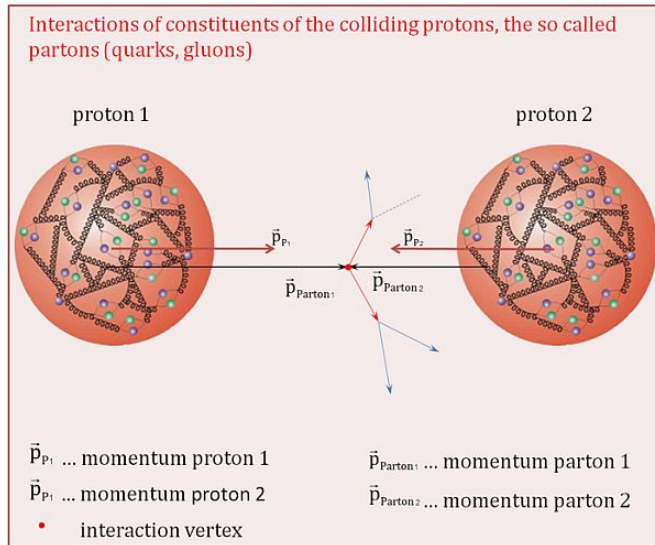


**Figure 2.10:** Proton-proton collision. Protons are composed of 3 valence quarks, a sea of quarks and gluons; therefore in a proton-proton collision, quarks and gluons are those who collide. [35].

727

728 Protons are composed of quarks and these quarks are bound by gluons; however,  
729 what is commonly called the quark content of the proton makes reference to the  
730 valence quarks. A sea of quarks and gluons is also present inside the proton as repre-  
731 sented in figure 2.10. In a proton-proton (pp) collision, the constituents (quarks and  
732 gluons) are those who collide. The pp cross section depends on the momentum of  
733 the colliding particles, reason for which it is needed to know how the momentum is  
734 distributed inside the proton. Quarks and gluons are known as partons and the func-  
735 tions that describe how the proton momentum is distributed among partons inside it  
736 are called “parton distribution functions (PDFs)”; PDFs are determined from experi-  
737 mental data obtained in experiments where the internal structure of hadrons is tested.

738

<sup>739</sup> In addition, in physics, a common approach to study complex systems consists in

740 starting with a simpler version of them, for which a well known description is avail-  
 741 able, and add an additional “perturbation” which represents a small deviation from  
 742 the known behavior. If the perturbation is small enough, the physical quantities as-  
 743 sociated with the perturbed system are expressed as a series of corrections to those  
 744 of the simpler system; therefore, the more terms are considered in the series (the  
 745 higher order in the perturbation series), the more precise is the the description of the  
 746 complex system.

747

748 This thesis explores the Higgs production at LHC; therefore the overview presented  
 749 here will be oriented specifically to the production mechanisms after pp collisions at  
 750 LHC.

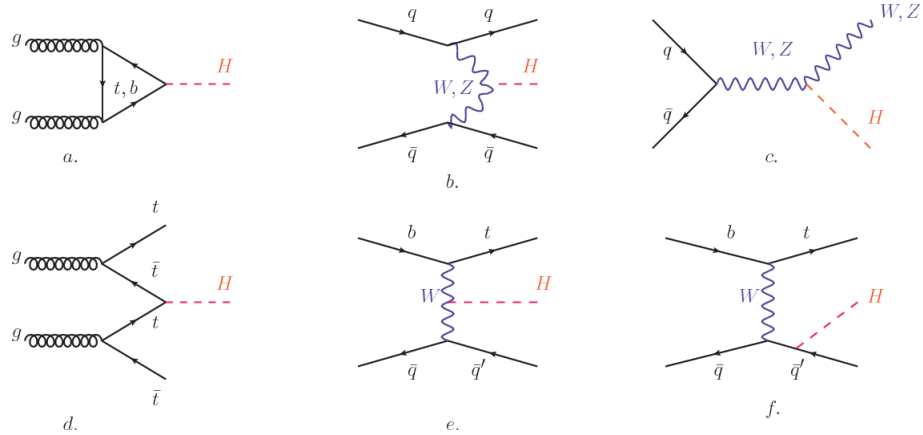


**Figure 2.11:** Main Higgs boson production mechanism Feynman diagrams. a. gluon-gluon fusion, b. vector boson fusion (VBF), c. Higgs-strahlung, d. Associated production with a top or bottom quark pair, e-f. associated production with a single top quark.

751 Figure 2.11 shows the Feynman diagrams for the leading order (first order) Higgs  
 752 production processes at LHC, while the cross section for Higgs production as a func-  
 753 tion of the center of mass-energy ( $\sqrt{s}$ ) for pp collisions is showed in figure 2.12 left.  
 754 The tags NLO (next to leading order), NNLO (next to next to leading order) and  
 755 N3LO (next to next to next to leading order) make reference to the order at which

756 the perturbation series have been considered.

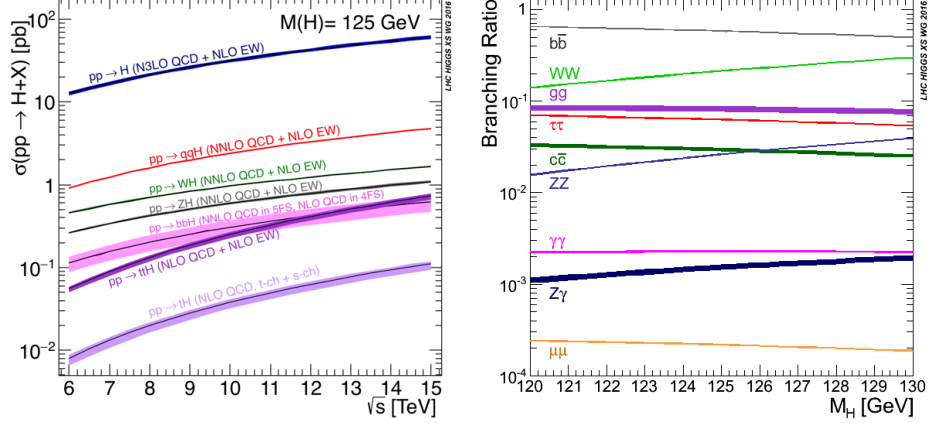


**Figure 2.12:** Higgs boson production cross sections (left) and decay branching ratios (right) for the main mechanisms. The VBF is indicated as  $q\bar{q}H$  [36].

757 As shown in eqns 2.47, 2.51 and 2.55, the strength of the Higgs-fermion interaction  
 758 is proportional to the fermion mass while the strength of the Higgs-gauge boson  
 759 interaction is proportional to the square of the gauge boson mass, which implies  
 760 that the Higgs production and decay mechanisms are dominated by couplings  $H -$   
 761  $(W, Z, t, b, \tau)$ .

762 The main production mechanism is the gluon fusion (figure 2.11a and  $pp \rightarrow H$  in figure  
 763 2.12) given that gluons carry the highest fraction of momentum of the protons in pp  
 764 colliders. Since the Higgs boson does not couple to gluons, the mechanism proceeds  
 765 through the exchange of a virtual top-quark loop given that for it the coupling is  
 766 the biggest. Note that in this process, the Higgs boson is produced alone, which  
 767 makes this mechanism experimentally clean when combined with the two-photon or  
 768 the four-lepton decay channels (see section 2.3.7).

769 Vector boson fusion (figure 2.11b and  $pp \rightarrow q\bar{q}H$  in figure 2.12) has the second largest  
 770 production cross section. The scattering of two fermions is mediated by a weak  
 771 gauge boson which later emits a Higgs boson. In the final state, the two fermions

772 tend to be located in a particular region of the detector which is used as a signature  
 773 when analyzing the datasets provided by the experiments. More details about how  
 774 to identify events of interest in an analysis will be given in chapter 5.

775 The next production mechanism is Higgs-strahlung (figure 2.11c and  $pp \rightarrow WH, pp \rightarrow$   
 776  $ZH$  in figure 2.12) where two fermions annihilate to form a weak gauge boson. If the  
 777 initial fermions have enough energy, the emergent boson eventually will emit a Higgs  
 778 boson.

779 The associated production with a top or bottom quark pair and the associated pro-  
 780 duction with a single top quark (figure 2.11d-f and  $pp \rightarrow bbH, pp \rightarrow t\bar{t}H, pp \rightarrow tH$   
 781 in figure 2.12) have a smaller cross section than the main three mechanisms above,  
 782 but they provide a good opportunity to test the Higgs-top coupling. The analysis  
 783 reported in this thesis is developed using these production mechanisms. A detailed  
 784 description of the  $tH$  mechanism will be given in section 2.4.

### 785 2.3.7 Higgs boson decay channels

786 When a particle can decay through several modes, also known as channels, the  
 787 probability of decaying through a given channel is quantified by the “branching ratio  
 788 (BR)” of the decay channel; thus, the BR is defined as the ratio of number of decays  
 789 going through that given channel to the total number of decays. In regard to the  
 790 Higgs boson decay, the BR can be predicted with accuracy once the Higgs mass is  
 791 known [37, 38]. In figure 2.12 right, a plot of the BR as a function of the Higgs mass  
 792 is presented. The largest predicted BR corresponds to the  $b\bar{b}$  pair decay channel (see  
 793 table 2.9).

Decay channel	Branching ratio	Rel. uncertainty
$H \rightarrow b\bar{b}$	$5.84 \times 10^{-1}$	$+3.2\% - 3.3\%$
$H \rightarrow W^+W^-$	$2.14 \times 10^{-1}$	$+4.3\% - 4.2\%$
$H \rightarrow \tau^+\tau^-$	$6.27 \times 10^{-2}$	$+5.7\% - 5.7\%$
$H \rightarrow ZZ$	$2.62 \times 10^{-2}$	$+4.3\% - 4.1\%$
$H \rightarrow \gamma\gamma$	$2.27 \times 10^{-3}$	$+5.0\% - 4.9\%$
$H \rightarrow Z\gamma$	$1.53 \times 10^{-3}$	$+9.0\% - 8.9\%$
$H \rightarrow \mu^+\mu^-$	$2.18 \times 10^{-4}$	$+6.0\% - 5.9\%$

**Table 2.9:** Predicted branching ratios and the relative uncertainty for a SM Higgs boson with  $m_H = 125\text{GeV}/c^2$ . [9]

<sup>795</sup> 2.4 Associated production of a Higgs boson and a  
<sup>796</sup> single Top quark.

Associated production of Higgs boson has been extensively studied [39–43]. While measurements of the main Higgs production mechanisms rates are sensitive to the strength of the Higgs coupling to W boson or top quark, they are not sensitive to the relative sign between the two couplings. In this thesis, the Higgs boson production mechanism explored is the associated production with a single top quark ( $t\bar{h}$ ) which offers sensitiveness to the relative sign of the Higgs couplings to W boson and to top quark. The description given here is based on the reference [41]

804

A process where two incoming particles interact and produce a final state with two particles can proceed in three ways also called channels (see, for instance, figure 2.13 omitting the red line). The t-channel represents processes where an intermediate particle is emitted by one of the incoming particles and absorbed by the other. The s-channel represents processes where the two incoming particles merge into an intermediate particle which eventually will split into the particles in the final state. The third channel, u-channel, is similar to the t-channel but the two outgoing particles

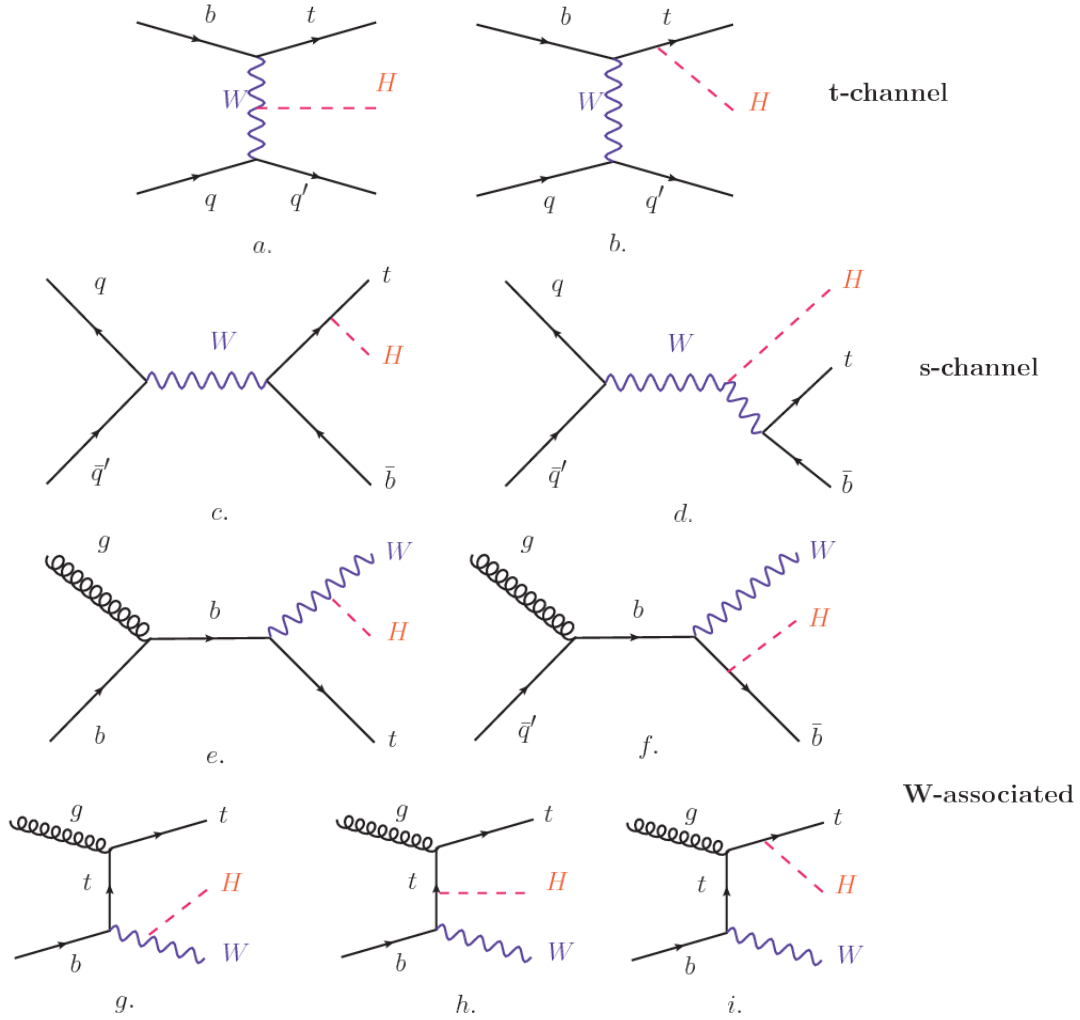


**Figure 2.13:** Associated Higgs boson production mechanism Feynman diagrams. a.,b. t-channel (tHq), c.,d. s-channel (tHb), e-i. W-associated.

812 interchange their roles.

813

814 The *th* production, where Higgs boson can be radiated either from the top quark or  
 815 from the W boson, is represented by the leading order Feynman diagrams in figure  
 816 2.13. The cross section for the *th* process is calculated, as usual, summing over  
 817 the contributions from the different feynman diagrams; therefore it depends on the  
 818 interference between the contributions. In the SM, the interference for t-channel (tHq

819 process) and W-associated (tHW process) production is destructive [39] resulting in  
 820 the small cross sections presented in table 2.10.

tH production channel	Cross section (fb)
t-channel ( $pp \rightarrow tHq$ )	$70.79^{+2.99}_{-4.80}$
W-associated ( $pp \rightarrow tHW$ )	$15.61^{+0.83}_{-1.04}$
s-channel( $pp \rightarrow tHb$ )	$2.87^{+0.09}_{-0.08}$

**Table 2.10:** Predicted SM cross sections for  $tH$  production at  $\sqrt{s} = 13$  TeV [44, 45].

821

822 While the s-channel contribution can be neglected, it will be shown that a deviation  
 823 from the SM destructive interference would result in an enhancement of the  $th$  cross  
 824 section compared to that in SM, which could be used to get information about the  
 825 sign of the Higgs-top coupling [41, 42]. In order to describe  $th$  production processes,  
 826 Feynman diagram 2.13b will be considered; there, the W boson is radiated by a  
 827 quark in the proton and eventually it will interact with the b quark. In the high  
 828 energy regime, the effective W approximation [46] allows to describe the process as  
 829 the emmision of an approximately on-shell W and its hard scattering with the b  
 830 quark; i.e.  $Wb \rightarrow th$ . The scattering amplitude for the process is given by

$$\mathcal{A} = \frac{g}{\sqrt{2}} \left[ (\kappa_t - \kappa_V) \frac{m_t \sqrt{s}}{m_W v} A \left( \frac{t}{s}, \varphi; \xi_t, \xi_b \right) + \left( \kappa_V \frac{2m_W s}{v} \frac{1}{t} + (2\kappa_t - \kappa_V) \frac{m_t^2}{m_W v} \right) B \left( \frac{t}{s}, \varphi; \xi_t, \xi_b \right) \right], \quad (2.57)$$

831 where  $\kappa_V \equiv g_{HVV}/g_{HVV}^{SM}$  and  $\kappa_t \equiv g_{Ht}/g_{Ht}^{SM} = y_t/y_t^{SM}$  are scaling factors that quan-  
 832 tify possible deviations of the couplings, Higgs-Vector boson (H-W) and Higgs-top  
 833 (H-t) respectively, from the SM couplings;  $s = (p_W + p_b)^2$ ,  $t = (p_W - p_H)^2$ ,  $\varphi$  is the  
 834 Higgs azimuthal angle around the  $z$  axis taken parallel to the direction of motion of  
 835 the incoming W; A and B are funtions describing the weak interaction in terms of

836 the chiral states of the quarks  $b$  and  $t$ . Terms that vanish in the high energy limit  
 837 have been neglected as well as the Higgs and  $b$  quark masses<sup>8</sup>.

838

839 The scattering amplitude grows with energy like  $\sqrt{s}$  for  $\kappa_V \neq \kappa_t$ , in contrast to  
 840 the SM ( $\kappa_t = \kappa_V = 1$ ), where the first term in 2.57 cancels out and the amplitude  
 841 is constant for large  $s$ ; therefore, a deviation from the SM predictions represents an  
 842 enhancement in the  $tHq$  cross section. In particular, for a SM H-W coupling and a H-t  
 843 coupling of inverted sign with respect to the SM ( $\kappa_V = -\kappa_t = 1$ ) the  $tHq$  cross section  
 844 is enhanced by a factor greater 10 as seen in the figure 2.14 taken from reference [41];  
 845 reference [47] has reported similar enhancement results.

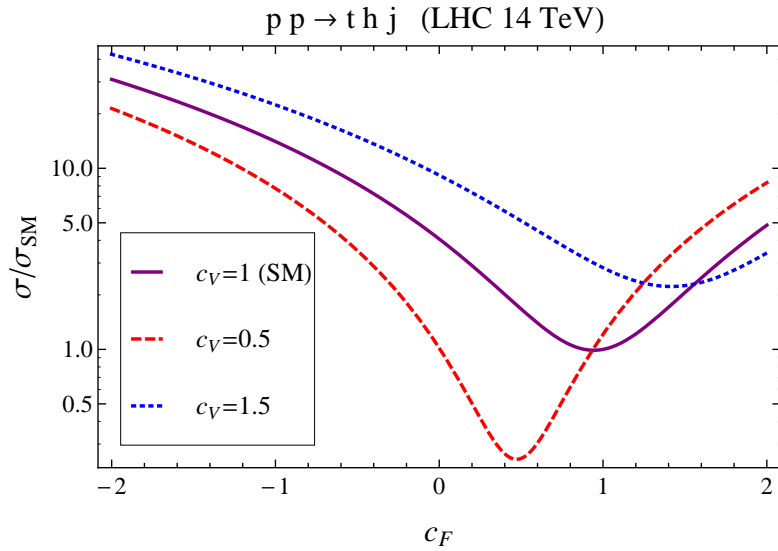


**Figure 2.14:** Cross section for  $tHq$  process as a function of  $\kappa_t$ , normalized to the SM, for three values of  $\kappa_V$ . In the plot  $c_f$  refers to the Higgs-fermion coupling which is dominated by the H-t coupling and represented here by  $\kappa_t$ . Solid, dashed and dotted lines correspond to  $c_V \rightarrow \kappa_V = 1, 0.5, 1.5$  respectively. Note that for the SM ( $\kappa_V = \kappa_t = 1$ ), the destructive effect of the interference is maximal.

846 A similar analysis is valid for the W-associated channel but, in that case, the inter-  
 847 ference is more complicated since there are more than two contributions and an ad-

---

<sup>8</sup> A detailed explanation of the structure and approximations used to derive  $\mathcal{A}$  can be found in reference [41]

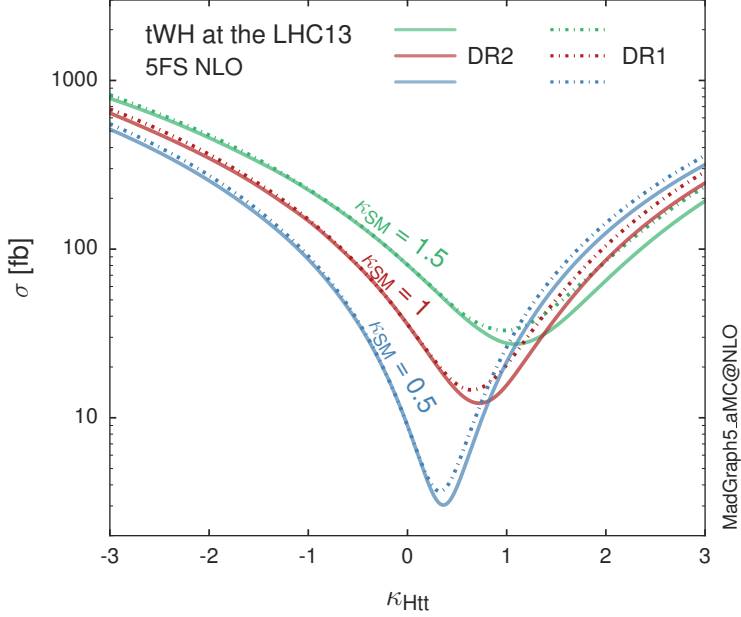


**Figure 2.15:** Cross section for  $tHW$  process as a function of  $\kappa_{Htt}$ , for three values of  $\kappa_{SM}$  at  $\sqrt{s} = 13$  TeV.  $\kappa_{Htt}^2 = \sigma_{Htt}/\sigma_{Htt}^{SM}$  is a simple rescaling of the SM Higgs interactions.

ditional interference with the production of Higgs boson and a top pair process( $t\bar{t}H$ ).  
The calculations are made using the so-called Diagram Removal (DR) technique where  
interfering diagrams are removed (or added) from the calculations in order to evaluate  
the impact of the removed contributions. DR1 was defined to neglect  $t\bar{t}H$  interference  
while DR2 was defined to take  $t\bar{t}H$  interference into account [48]. As shown in figure  
2.15, the  $tHW$  cross section is enhanced from about 15 fb (SM:  $\kappa_{Htt} = 1$ ) to about  
150 fb ( $\kappa_{Htt} = -1$ ). Differences between curves for DR1 and DR2 help to gauge the  
impact of the interference with  $t\bar{t}H$ .  
Results of the calculations of the  $tHq$  and  $tHW$  cross sections at  $\sqrt{s} = 13$  TeV can be  
found in reference [49] and a summary of the results is presented in table 2.11.

	$\sqrt{s}$ TeV	$\kappa_t = 1$	$\kappa_t = -1$
$\sigma^{LO}(tHq)(\text{fb})$ [41]	8	$\approx 17.4$	$\approx 252.7$
	14	$\approx 80.4$	$\approx 1042$
$\sigma^{NLO}(tHq)(\text{fb})$ [41]	8	$18.28^{+0.42}_{-0.38}$	$233.8^{+4.6}_{-0.0}$
	14	$88.2^{+1.7}_{-0.0}$	$982.8^{+28}_{-0.0}$
$\sigma^{LO}(tHq)(\text{fb})$ [47]	14	$\approx 71.8$	$\approx 893$
$\sigma^{LO}(tHW)(\text{fb})$ [47]	14	$\approx 16.0$	$\approx 139$
$\sigma^{NLO}(tHq)(\text{fb})$ [49]	8	$18.69^{+8.62\%}_{-17.13\%}$	-
	13	$74.25^{+7.48\%}_{-15.35\%}$	$848^{+7.37\%}_{-13.70\%}$
	14	$90.10^{+7.34\%}_{-15.13\%}$	$1011^{+7.24\%}_{-13.39\%}$
$\sigma^{LO}(tHW)(\text{fb})$ [48]	13	$15.77^{+15.91\%}_{-15.76\%}$	-
$\sigma^{NLO}DR1(tHW)(\text{fb})$ [48]	13	$21.72^{+6.52\%}_{-5.24\%}$	$\approx 150$
$\sigma^{NLO}DR2(tHW)(\text{fb})$ [48]	13	$16.28^{+7.34\%}_{-15.13\%}$	$\approx 150$

**Table 2.11:** Predicted enhancement of the  $tHq$  and  $tHW$  cross sections at LHC for  $\kappa_V = 1$  and  $\kappa_t = \pm 1$  at LO and NLO; the cross section enhancement of more than a factor of 10 is due to the flippling in the sign of the H-t coupling with respect to the SM one.

## 859 2.5 The CP-mixing in tH processes

860 In addition to the sensitivity to sign of the H-t coupling,  $tHq$  and  $tHW$  processes have  
 861 been proposed as a tool to investigate the possibility of a H-t coupling that does not  
 862 conserve CP [43, 48, 50]. Current experimental results are consistent with SM H-V  
 863 and H-t couplings; however, negative H-t coupling is not excluded completely [52].

864

865 In this thesis, the sensitivity of  $th$  processes to CP-mixing is also studied in the  
 866 effective field theory framework and based in references [43, 48]; a generic particle  
 867 ( $X_0$ ) of spin-0 and a general CP violating interaction with the top quark, can couple  
 868 to scalar and pseudoscalar fermionic densities. The H-W interaction is assumed to  
 869 be SM-like. The Lagrangian modeling the H-t interaction is given by

$$\mathcal{L}_0^t = -\bar{\psi}_t (c_\alpha \kappa_{Htt} g_{Htt} + i s_\alpha \kappa_{Att} g_{Att} \gamma_5) \psi_t X_0, \quad (2.58)$$

870 where  $\alpha$  is the CP-mixing phase,  $c_\alpha \equiv \cos \alpha$  and  $s_\alpha \equiv \sin \alpha$ ,  $\kappa_{Htt}$  and  $\kappa_{Att}$  are real  
 871 dimensionless rescaling parameters<sup>9</sup>,  $g_{Htt} = g_{Att} = m_t/v = y_t/\sqrt{2}$  and  $v \sim 246$  GeV is  
 872 the Higgs vacuum expectation value. In this parametrization, it is easy to recover  
 873 three special cases

- 874     • CP-even coupling  $\rightarrow \alpha = 0^\circ$
- 875     • CP-odd coupling  $\rightarrow \alpha = 90^\circ$
- 876     • SM coupling  $\rightarrow \alpha = 0^\circ$  and  $\kappa_{Htt} = 1$

877 The loop induced  $X_0$  coupling to gluons can also be described in terms of the  
 878 parametrization above, according to

$$\mathcal{L}_0^g = -\frac{1}{4} \left( c_\alpha \kappa_{Hgg} g_{Hgg} G_{\mu\nu}^a G^{a,\mu\nu} + s_\alpha \kappa_{Agg} g_{Agg} G_{\mu\nu}^a \tilde{G}^{a,\mu\nu} \right) X_0. \quad (2.59)$$

879 where  $g_{Hgg} = -\alpha_s/3\pi v$  and  $g_{Agg} = \alpha_s/2\pi v$ . Under the assumption that the top quark  
 880 dominates the gluon-fusion process at LHC energies,  $\kappa_{Hgg} \rightarrow \kappa_{Htt}$  and  $\kappa_{Agg} \rightarrow \kappa_{Att}$ ,  
 881 so that the ratio between the gluon-gluon fusion cross section for  $X_0$  and for the SM  
 882 Higgs prediction can be written as

$$\frac{\sigma_{NLO}^{gg \rightarrow X_0}}{\sigma_{NLO,SM}^{gg \rightarrow H}} = c_\alpha^2 \kappa_{Htt}^2 + s_\alpha^2 \left( \kappa_{Att} \frac{g_{Agg}}{g_{Hgg}} \right)^2. \quad (2.60)$$

883 If the rescaling parameters are set to

$$\kappa_{Htt} = 1, \quad \kappa_{Att} = \left| \frac{g_{Hgg}}{g_{Agg}} \right| = \frac{2}{3}. \quad (2.61)$$

884 the gluon-fusion SM cross section is reproduced for every value of the CP-mixing  
 885 angle  $\alpha$ ; therefore, by imposing that condition to the Lagrangian density 2.58, the

---

<sup>9</sup> analog to  $\kappa_t$  and  $\kappa_V$

CP-mixing angle is not constrained by current data. Figure 2.16 shows the NLO cross sections for t-channel  $tX_0$ (blue) and  $t\bar{t}X_0$  (red) associated production processes as a function of the CP-mixing angle  $\alpha$ .  $X_0$  is a generic spin-0 particle with top quark CP-violating coupling. Rescaling factors  $\kappa_{Htt}$  and  $\kappa_{Att}$  have been set to reproduce the SM gluon-fusion cross sections.

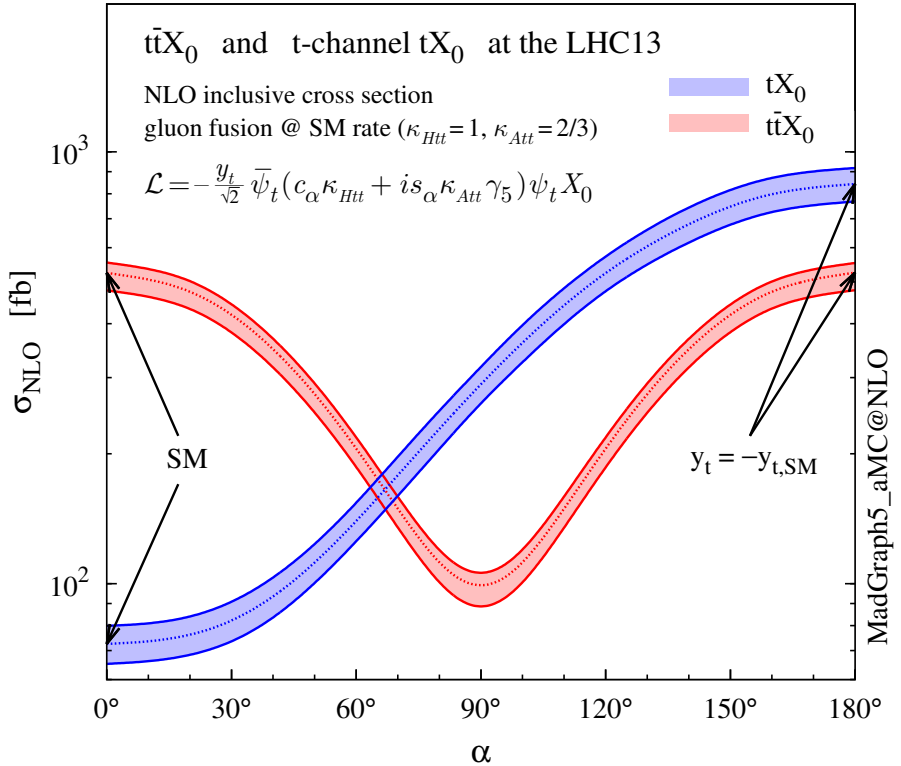


**Figure 2.16:** NLO cross sections for t-channel  $tX_0$ (blue) and  $t\bar{t}X_0$  (red) associated production processes as a function of the CP-mixing angle  $\alpha$ .  $X_0$  is a generic spin-0 particle with top quark CP-violating coupling [43].

It is interesting to notice that the  $tX_0$  cross section is enhanced, by a factor of about 10, when a continuous rotation in the scalar-pseudoscalar plane is applied; this enhancement is similar to the enhancement produced when the H-t coupling is flipped in sign with respect to the SM ( $y_t = -y_{t,SM}$  in the plot), as showed in section 2.4. In contrast, the degeneracy in the  $t\bar{t}X_0$  cross section is still present given that it depends

quadratically on the H-t coupling, but more interesting is to notice that  $t\bar{t}X_0$  cross section is exceeded by  $tX_0$  cross section after  $\alpha \sim 60^\circ$ .

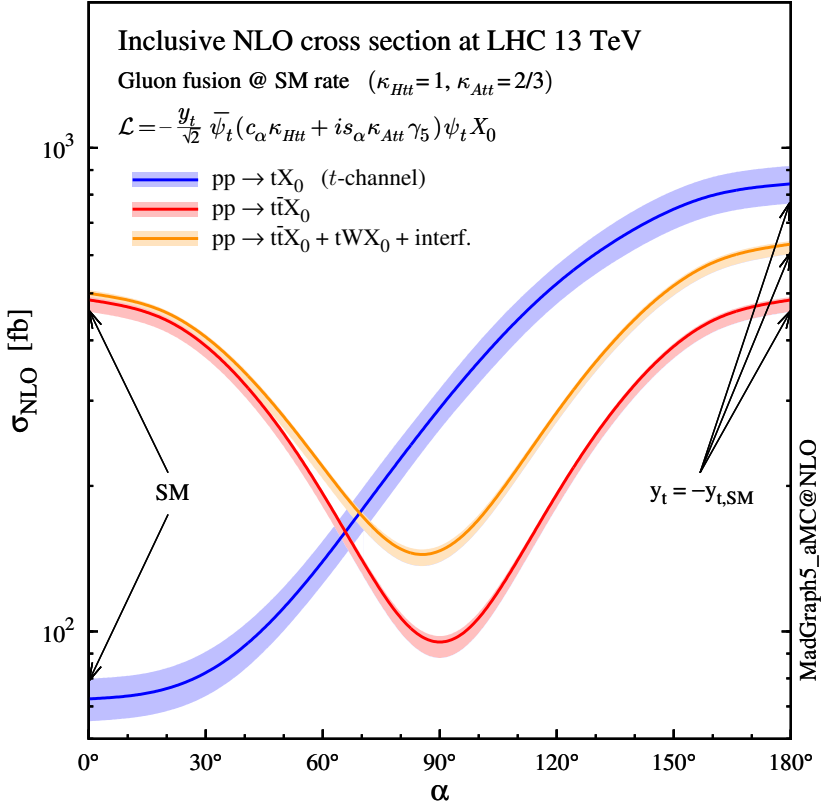


**Figure 2.17:** NLO cross sections for t-channel  $tX_0$ (blue),  $t\bar{t}X_0$  (red) associated production processes and combined  $tWX_0 + t\bar{t}X_0$  (including interference) production as a function of the CP-mixing angle  $\alpha$  [43].

897

898 A similar parametrization can be used to investigate the  $tHW$  process sensitivity to  
 899 CP-violating H-t coupling. As said in 2.4, the interference in the W-associated chan-  
 900 nel is more complicated because there are more than two contributions and also there  
 901 is interference with the  $t\bar{t}H$  production process.

902

903 Figure 2.17 shows the NLO cross sections for t-channel  $tX_0$ (blue),  $t\bar{t}X_0$  (red) asso-  
 904 ciated production and for the combined  $tWX_0 + t\bar{t}X_0 +$  interference (orange) as a  
 905 function of the CP-mixing angle. It is clear that the effect of the interference in the

906 combined case is the lifting of the degeneracy present in the  $t\bar{t}X_0$  production. The  
 907 constructive interference enhances the cross section from about 500 fb at SM ( $\alpha = 0$ )  
 908 to about 600 fb ( $\alpha = 180^\circ \rightarrow y_t = -y_{t,SM}$ ).

909 An analysis combining  $tHq$  and  $tHW$  processes will be made in this thesis taking  
 910 advantage of the sensitivity improvement.

911 **2.6 Experimantal status of the anomalous**  
 912 **Higg-fermion coupling.**

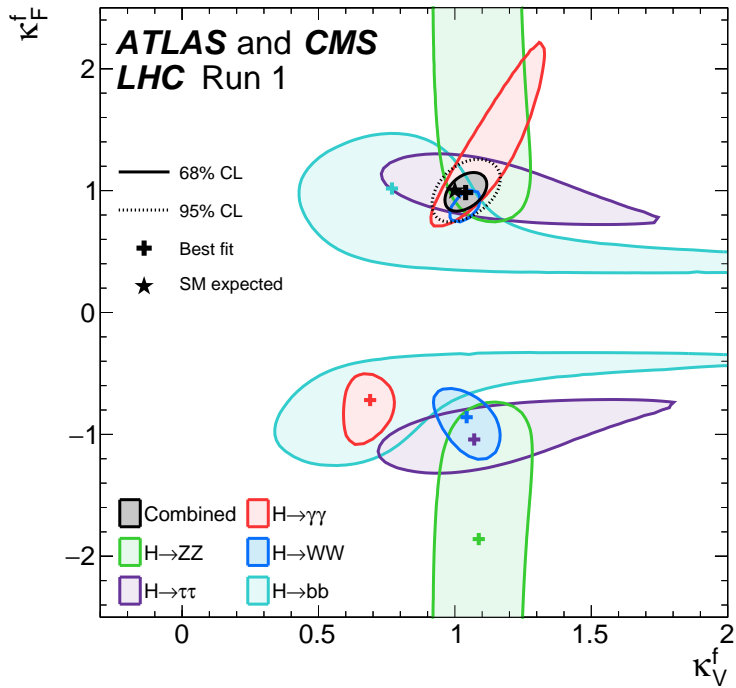


**Figure 2.18:** Combination of the ATLAS and CMS fits for coupling modifiers  $\kappa_t$ - $\kappa_V$ ; also shown the individual decay channels combination and their global combination. No assumptions have been made on the sign of the coupling modifiers [52].

913 ATLAS and CMS have performed analysis of the anomalous H-f coupling by making  
 914 likelihood scans for the two coupling modifiers,  $\kappa_t$  and  $\kappa_V$ , under the assumption that

915  $\kappa_Z = \kappa_W = \kappa_V$  and  $\kappa_t = \kappa_\tau = \kappa_b = \kappa_f$ . Figure 2.18 shows the result of the combination  
916 of ATLAS and CMS fits; also the individual decay channels combination and the  
917 global combination results are shown.

918 While all the channels are compatible for positive values of the modifiers, for negative  
919 values of  $\kappa_t$  there is no compatibility. The best fit for individual channels is compatible  
920 with negative values of  $\kappa_t$  except for the  $H \rightarrow bb$  channel which is expected to be the  
921 most sensitive channel; therefore, the best fit for the global fit yields  $\kappa_t \geq 0$ . Thus,  
922 the anomalous H-t coupling cannot be excluded completely.

923 **Chapter 3**

924 **The CMS experiment at the LHC**

925 **3.1 Introduction**

926 Located on the Swiss-French border, the European Council for Nuclear Research  
927 (CERN) is the largest scientific organization leading the particle physics research.  
928 About 13000 people in a broad range of fields including users, students, scientists,  
929 engineers among others, contribute to the data taking and analysis, with the goal  
930 of unveiling the secrets of nature and revealing the fundamental structure of the  
931 universe. CERN is also the home of the Large Hadron Collider (LHC), the largest  
932 circular particle accelerator around the world, where protons (or heavy ions) traveling  
933 close to the speed of light, are made to collide. These collisions open a window  
934 to investigate how particles (and their constituents if they are composite) interact  
935 with each other, providing clues about the laws of nature. This chapter presents an  
936 overview of the LHC structure and operation. A detailed description of the CMS  
937 detector is offered, given that the data used in this thesis have been taken with this  
938 detector.

## 939 3.2 The LHC

940 With 27 km of circumference, the LHC is currently the largest and most powerful  
 941 circular accelerator in the world. It is installed in the same tunnel where the Large  
 942 Electron-Positron (LEP) collider was located, taking advantage of the existing infras-  
 943 tructure. The LHC is also the larger accelerator in the CERN's accelerator complex  
 944 and is assisted by several successive accelerating stages before the particles are in-  
 945 jected into the LHC ring where they reach their maximum energy (see figure 3.1).

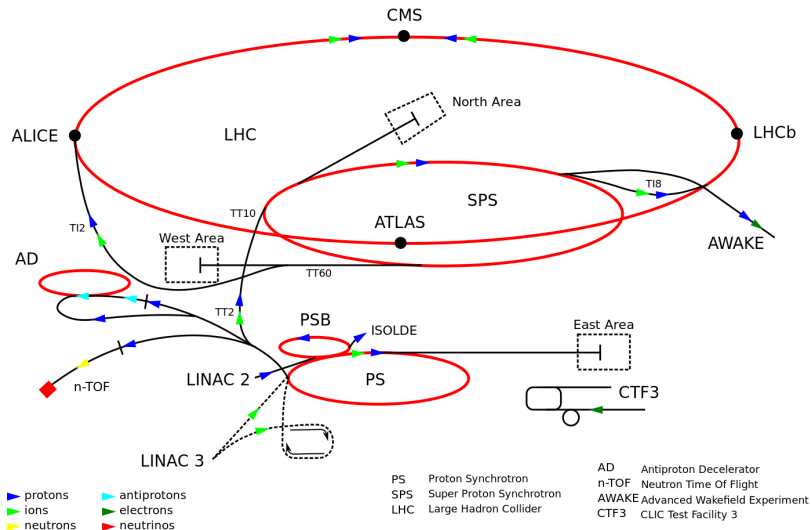


**Figure 3.1:** CERN accelerator complex. Blue arrows show the path followed by protons along the acceleration process [53].

946 LHC runs in three modes depending on the particles being accelerated

- 947 • Proton-Proton collisions ( $pp$ ) for multiple physics experiments.
- 948 • Lead-Lead collisions ( $Pb-Pb$ ) for heavy ion experiments.
- 949 • Proton-Lead collisions ( $p-Pb$ ) for quark-gluon plasma experiments.

950 In this thesis  $pp$  collisions will be considered.

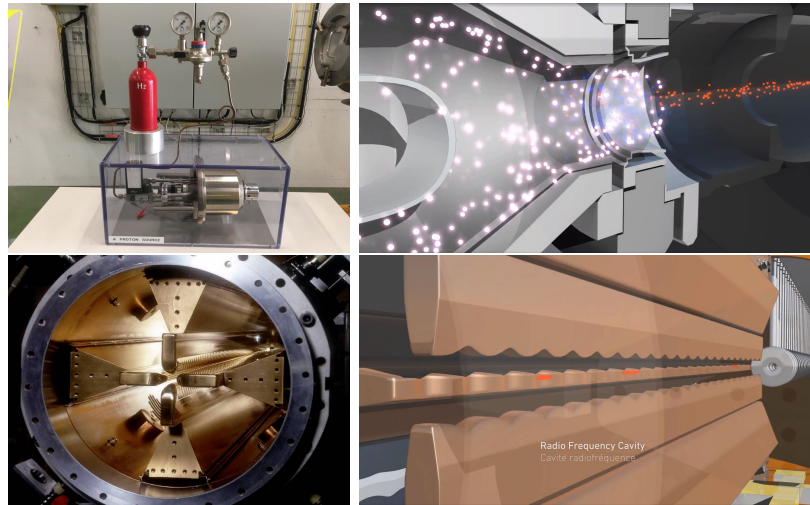


**Figure 3.2:** LHC protons source and the first acceleration stage. Top: the bottle contains hydrogen gas (white dots) which is injected into the metal cylinder to be broken down into electrons(blue dots) and protons(red dots); Bottom: the obtained protons are directed towards the radio frequency quadrupole which perform the first acceleration, focus the beam and create the bunches of protons. [57, 58]

952 Collection of protons starts with hydrogen atoms taken from a bottle, containing hy-  
 953 drogen gas, and injecting them in a metal cylinder; hydrogen atoms are broken down  
 954 into electrons and protons by an intense electric field (see figure3.2 top). The result-  
 955 ing protons leave the metal cylinder towards a radio frequency quadrupole (RFQ)  
 956 that focus the beam, accelerates the protons and creates the packets of protons called  
 957 bunches. In the RFQ, an electric field is generated by a RF wave at a frequency that  
 958 matches the resonance frequency of the cavity where the electrodes are contained.  
 959 The beam of protons traveling on the RFQ axis experiences an alternating electric  
 960 field gradient that generates the focusing forces.

961

962 In order to accelerate the protons, a longitudinal time-varying electric field component  
 963 is added to the system; it is done by giving the electrodes a sinus-like profile as shown  
 964 in figure 3.2 bottom. By matching the speed and phase of the protons with the  
 965 longitudinal electric field the bunching is performed; protons synchronized with the

966 RFQ (synchronous proton) do not feel an accelerating force, but those protons in the  
 967 beam that have more (or less) energy than the synchronous proton (asynchronous  
 968 protons) will feel a decelerating (accelerating) force; therefore, asynchronous protons  
 969 will oscillate around the synchronous ones forming bunches of protons [55]. From the  
 970 RFQ protons emerge with energy 750 keV in bunches of about  $1.15 \times 10^{11}$  protons [56].

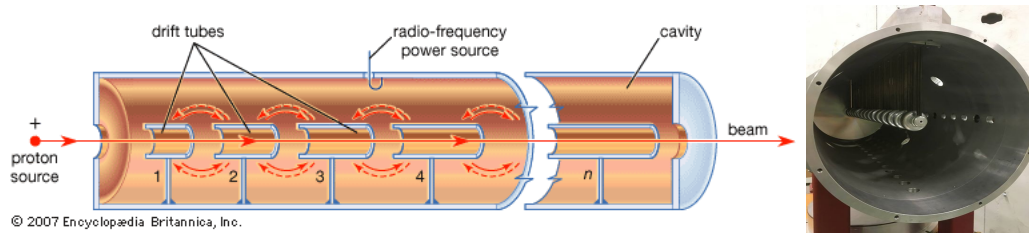


**Figure 3.3:** The LINAC2 accelerating system at CERN. Electric fields generated by radio frequency (RF) create acceleration and deceleration zones inside the cavity; deceleration zones are blocked by drift tubes where quadrupole magnets focus the proton beam. [59]

971 Proton bunches coming from the RFQ go to the linear accelerator 2 (LINAC2) where  
 972 they are accelerated to reach 50 MeV energy. In the LINAC2 stage, acceleration  
 973 is performed using electric fields generated by radio frequency which create zones  
 974 of acceleration and deceleration as shown in figure 3.3. In the deceleration zones,  
 975 the electric field is blocked using drift tubes where protons are free to drift while  
 976 quadrupole magnets focus the beam.

977

978 The beam coming from LINAC2 is injected into the proton synchrotron booster  
 979 (PSB) to reach 1.4 GeV in energy. The next acceleration is provided at the pro-  
 980 ton synchrotron (PS) up to 26 GeV, followed by the injection into the super proton  
 981 synchrotron (SPS) where protons are accelerated to 450 GeV. Finally, protons are  
 982 injected into the LHC where they are accelerated to the target energy of 6.5 TeV.  
 983 PSB, PS, SPS and LHC accelerate protons using the same RF acceleration technique  
 984 described before.

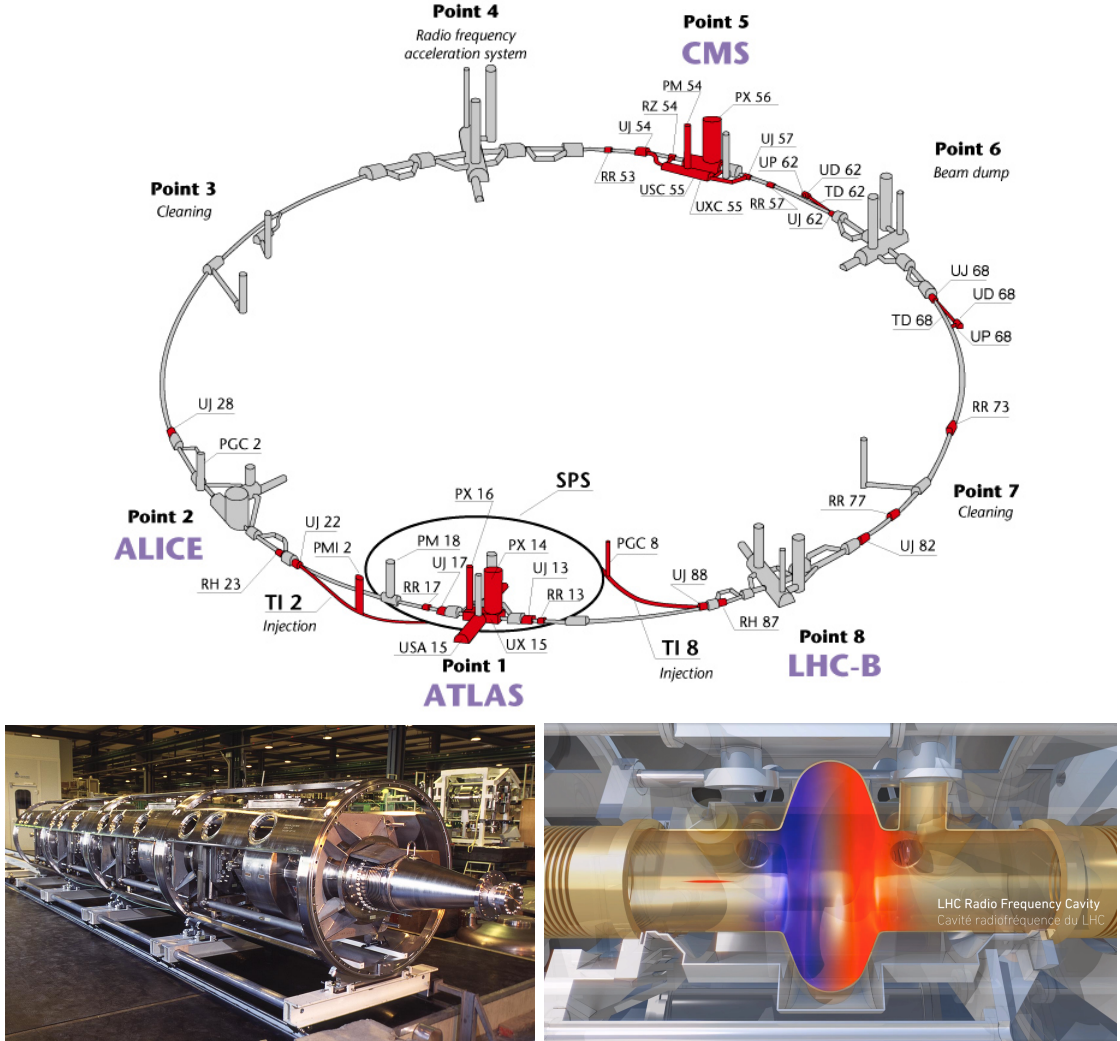


**Figure 3.4:** Top: LHC layout. The red zones indicate the infrastructure additions to the LEP installations, built to accommodate the ATLAS and CMS experiments which exceed the size of the former experiments located there [54]. Bottom: LHC RF cavities. A module accommodates 4 cavities that accelerate protons and preserve the bunch structure of the beam. [58, 60]

985 LHC has a system of 16 RF cavities located in the so-called point 4, as shown in  
 986 figure 3.4 top, tuned at a frequency of 400 MHz and the protons are carefully timed  
 987 so in addition to the acceleration effect the bunch structure of the beam is preserved.  
 988 Bottom side of figure 3.4 shows a picture of a Rf module composed of 4 RF cavities  
 989 working in a superconducting state at 4.5 K; also is showed a representation of the

990 accelerating electric field that accelerates the protons in the bunch.

991

992 While protons are accelerated in one section of the LHC ring, where the RF cavities  
 993 are located, in the rest of their path they have to be kept in the curved trajectory  
 994 defined by the LHC ring. Technically, LHC is not a perfect circle; RF, injection, beam  
 995 dumping, beam cleaning and sections before and after the experimental points where  
 996 protons collide are all straight sections. In total, there are 8 arcs 2.45 Km long each  
 997 and 8 straight sections 545 m long each. In order to curve the proton's trajectory in  
 998 the arc sections, superconducting dipole magnets are used.

999

1000 Inside the LHC ring, there are two proton beams traveling in opposite directions in  
 1001 two separated beam pipes; the beam pipes are kept at ultra-high vacuum ( $\sim 10^{-9}$   
 1002 Pa) to ensure that there are no particles that interact with the proton beams. The  
 1003 superconducting dipole magnets used in LHC are made of a NbTi alloy, capable of  
 1004 transporting currents of about 12000 A when cooled at a temperature below 2K using  
 1005 liquid helium (see figure 3.5).

1006

1007 Protons in the arc sections of LHC feel a centripetal force exerted by the dipole  
 1008 magnets which is perpendicular to the beam trajectory; The magnitude of magnetic  
 1009 field needed can be found assuming that protons travel at  $v \approx c$ , using the standard  
 1010 values for proton mass and charge and the LHC radius, as

$$F_m = \frac{mv^2}{r} = qBv \quad \rightarrow B = 8.33T \quad (3.1)$$

1011 which is about 100000 times the Earth's magnetic field. A representation of the mag-  
 1012 netic field generated by the dipole magnets is shown on the bottom left side of figure

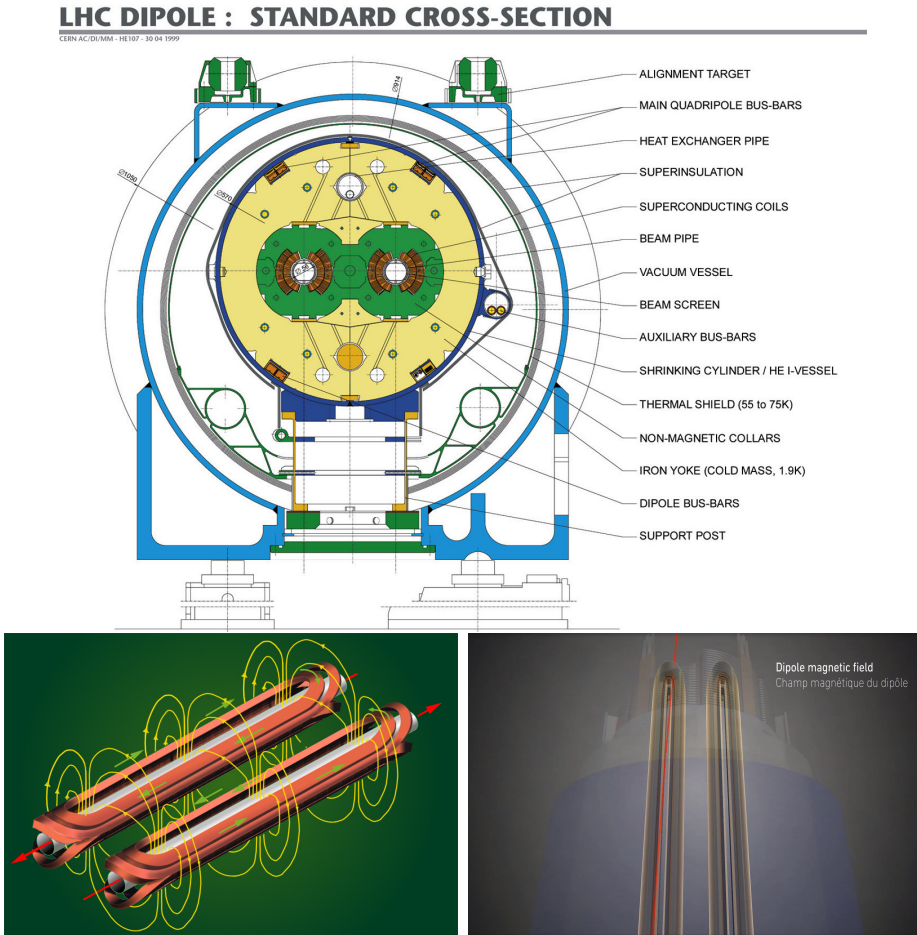


**Figure 3.5:** Top: LHC dipole magnet transverse view; cooling, shielding and mechanical support are indicated. Bottom left: Magnetic field generated by the dipole magnets; note that the direction of the field inside one beam pipe is opposite with respect to the other beam pipe which guarantee that both proton beams are curved in the same direction towards the center of the ring. The effect of the dipole magnetic field on the proton beam is represented on the bottom right side [58, 61, 62].

1013 3.5. The bending effect of the magnetic field on the proton beam is shown on the  
 1014 bottom right side of figure 3.5. Note that the dipole magnets are not curved; the arc  
 1015 section of the LHC ring is composed of straight dipole magnets of about 15 m. In  
 1016 total there are 1232 dipole magnets along the LHC ring.

1017

1018 In addition to bending the beam trajectory, the beam has to be focused so it stays

1019 inside the beam pipe. The focusing is performed by quadrupole magnets installed in  
 1020 a different straight section; in total 858 quadrupole magnets are installed along the  
 1021 LHC ring. Other effects like electromagnetic interaction among bunches, interaction  
 1022 with electron clouds from the beam pipe, the gravitational force on the protons, dif-  
 1023 ferences in energy among protons in the same bunch, among others, are corrected  
 1024 using sextupole and other magnetic multipoles.

1025

1026 The two proton beams inside the LHC ring are made of bunches with a cylindrical  
 1027 shape of about 7.5 cm long and about 1 mm in diameter; when bunches are close  
 1028 to the collision point (CP), the beam is focused up to a diameter of about 16  $\mu\text{m}$  in  
 1029 order to maximize the number of collisions per unit area and per second, known as  
 1030 luminosity ( $L$ ). Luminosity can be calculated using

$$L = fn \frac{N_1 N_2}{4\pi\sigma_x\sigma_y} \quad (3.2)$$

1031 where  $f$  is the revolution frequency,  $n$  is the number of bunches per beam,  $N_1$  and  
 1032  $N_2$  are the numbers of protons per bunch ( $1.5 \times 10^{11}$ ),  $\sigma_x$  and  $\sigma_y$  are the gaussian  
 1033 transverse sizes of the bunches. The expected luminosity about

$$f = \frac{v}{2\pi r_{LHC}} \approx \frac{3 \times 10^8 \text{ m/s}}{27 \text{ km}} \approx 11.1 \text{ kHz},$$

$$n = 2808$$

$$N_1 = N_2 = 1.5 \times 10^{11}$$

$$\sigma_x = \sigma_y = 16 \mu\text{m}$$

1034

$$L = 1.28 \times 10^{34} \text{ cm}^{-2} \text{ s}^{-1} = 1.28 \times 10^{-5} \text{ fb}^{-1} \text{ s}^{-1} \quad (3.3)$$

1035 Luminosity is a fundamental aspect of LHC given that the bigger luminosity the bigger  
 1036 number of collisions, which means that for processes with a very small cross section  
 1037 the number of expected occurrences is increased and so the chances of being detected.  
 1038 The integrated luminosity, i.e. the total luminosity, collected by the CMS experiment  
 1039 during 2016 is shown in figure 3.6; the data analyzed in this thesis corresponds to an  
 1040 integrated luminosity of  $35.9 \text{ fb}^{-1}$  at a center of mass-energy  $\sqrt{s} = 13 \text{ TeV}$ .  
 1041 A way to increase  $L$  is increasing the number of bunches in the beam. Currently, the  
 1042 separation between two consecutive bunches in the beam is 7.5 m which corresponds  
 1043 to a time separation of 25 ns. In the full LHC ring the allowed number of bunches is  
 1044  $n = 27\text{km}/7.5\text{m} = 3600$ ; however, there are some gaps in the bunch pattern intended  
 1045 for preparing the dumping and injection of the beam, thus, the proton beams are  
 1046 composed of 2808 bunches.

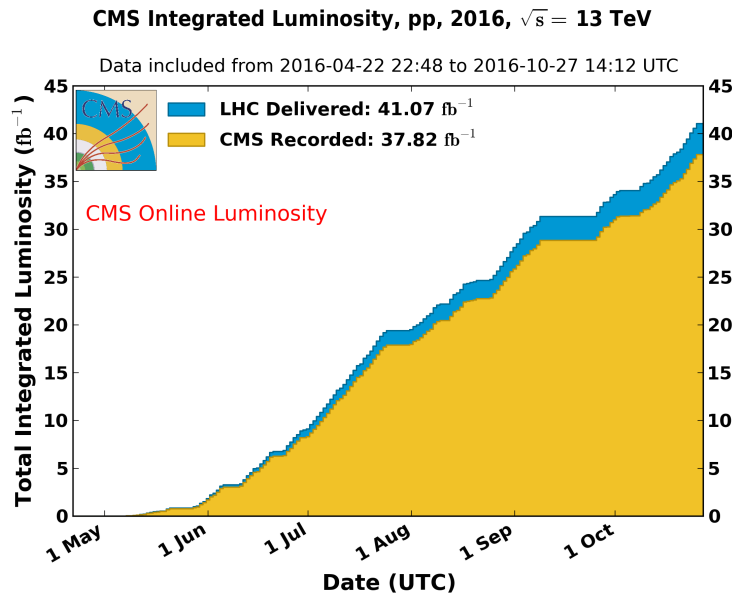


**Figure 3.6:** Integrated luminosity delivered by LHC and recorded by CMS during 2016. The difference between the delivered and the recorded luminosity is due to fails and issues occurred during the data taking in the CMS experiment [63].

1047 Once the proton beams reach the desired energy, they are brought to cross each other

1048 producing proton-proton collisions. The bunch crossing happens in precise places  
 1049 where the four LHC experiments are located, as seen in figure 3.7 left. In 2008, the  
 1050 first set of collisions involved protons with  $\sqrt{s} = 7$  TeV; the energy was increased to  
 1051 8 TeV in 2012 and to 13 TeV in 2015.

1052 CMS and ATLAS experiments, which are multi-purpose experiments, are enabled  
 1053 to explore physics in any of the collision modes. LHCb experiment is optimized  
 1054 to explore bottom quark physics, while ALICE is optimized for heavy ion collisions  
 1055 searches; TOTEM and LHCf are dedicated to forward physics studies; MoEDAL (not  
 1056 indicated in the figure) is intended for monopoles or massive pseudo stable particles  
 1057 searches.

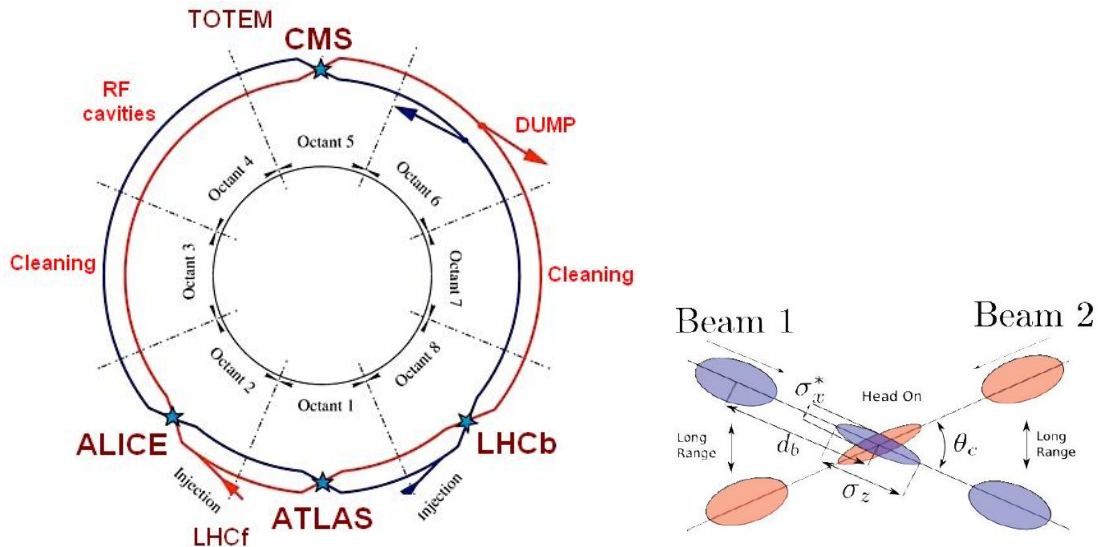


**Figure 3.7:** Left: LHC interaction points. Bunch crossing occurs where the LHC experiments are located [64]. Sections indicated as cleaning are dedicated to collimate the beam in order to protect the LHC ring from collisions with protons in very spreaded bunches. Right: bunch crossing scheme. Since the bunch crossing is not perfectly head-on, the luminosity is reduced in a factor of 17%.

1058 At the CP there are two interesting details that need to be addressed. The first  
 1059 one is that the bunch crossing does not occur head-on but at a small crossing angle  
 1060 ( $280 \mu\text{rad}$  in CMS and ATLAS) as shown in the right side of figure 3.7, affecting the

1061 overlapping between bunches; the consequence is a reduction of about 17% in the  
 1062 luminosity. The second one is the occurrence of multiple  $pp$  collisions in the same  
 1063 bunch crossing; this effect is called pile-up (PU). A fairly simple estimation of the  
 1064 PU follows from estimating the probability of collision between two protons, one from  
 1065 each of the bunches in course of collision; it depends roughly on the ratio of proton  
 1066 size and the cross section of the bunch in the interaction point, i.e.,

$$P(pp\text{-}collision) \sim \frac{d_{proton}^2}{\sigma_x \sigma_y} = \frac{(1\text{fm})^2}{(16\mu\text{m})^2} \sim 4 \times 10^{-21} \quad (3.4)$$

1067 however, there are  $N = 1.15 \times 10^{11}$  protons in a bunch, thus the estimated number of  
 1068 collisions in a bunch crossing is

$$PU = N^2 * P(pp\text{-}collision) \sim 50 \text{ pp-collision per bunch crossing}, \quad (3.5)$$

1069 about 20 of those  $pp$  collisions are inelastic. Each collision generates a vertex, but  
 1070 only the most energetic is considered as a primary vertex; the rest are considered as  
 1071 PU vertices. A multiple  $pp$  collision event in a bunch crossing at CMS is showed in  
 1072 figure3.8. Unstable particles outgoing from the primary vertex will eventually decay;  
 1073 this decay vertex is known as a secondary vertex.

1074 Next section presents a description of the CMS detector which it is the detector used  
 1075 to collect the data used in this thesis.

### 1076 3.3 The CMS experiment

1077 CMS is a general-purpose detector designed to conduct research in a wide range  
 1078 of physics from the standard model to new physics like extra dimensions and dark  
 1079 matter. Located at the point 5 in the LHC layout as shown in figure 3.4, CMS is

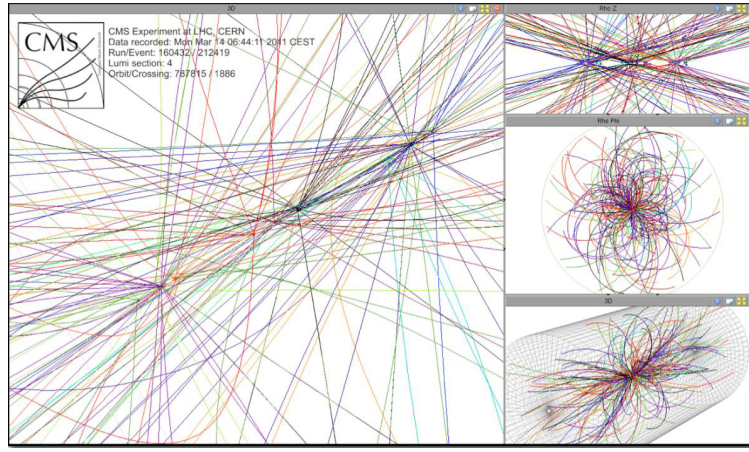


**Figure 3.8:** Multiple  $pp$  collision bunch crossing at CMS. Only the most energetic vertex is considered and the rest are cataloged as PU vertices [65].

1080 composed of several detection systems distributed in a cylindrical structure; in total,  
 1081 CMS weights about 12500 tons in a very compact 21.6 m long and 14.6 m diameter  
 1082 cylinder. It was built in 15 separate sections at the ground level and lowered to the  
 1083 cavern individually to be assembled. A complete and detailed description of the CMS  
 1084 detector and its components is given in reference [66] on which this section is based on.

1085

1086 Figure 3.9 shows the layout of the CMS detector. The design is driven by the require-  
 1087 ments on the identification, momentum resolution and unambiguous charge determi-  
 1088 nation of the muons; therefore, a large bending power is provided by the solenoid  
 1089 magnet made of superconducting cable capable to generate a 3.8 T magnetic field.  
 1090 The detection system is composed of (from the innermost to the outermost)

1091 • Pixel detector.

1092 • Silicon strip tracker.

1093 • Preshower detector.

1094 • Electromagnetic calorimeter.

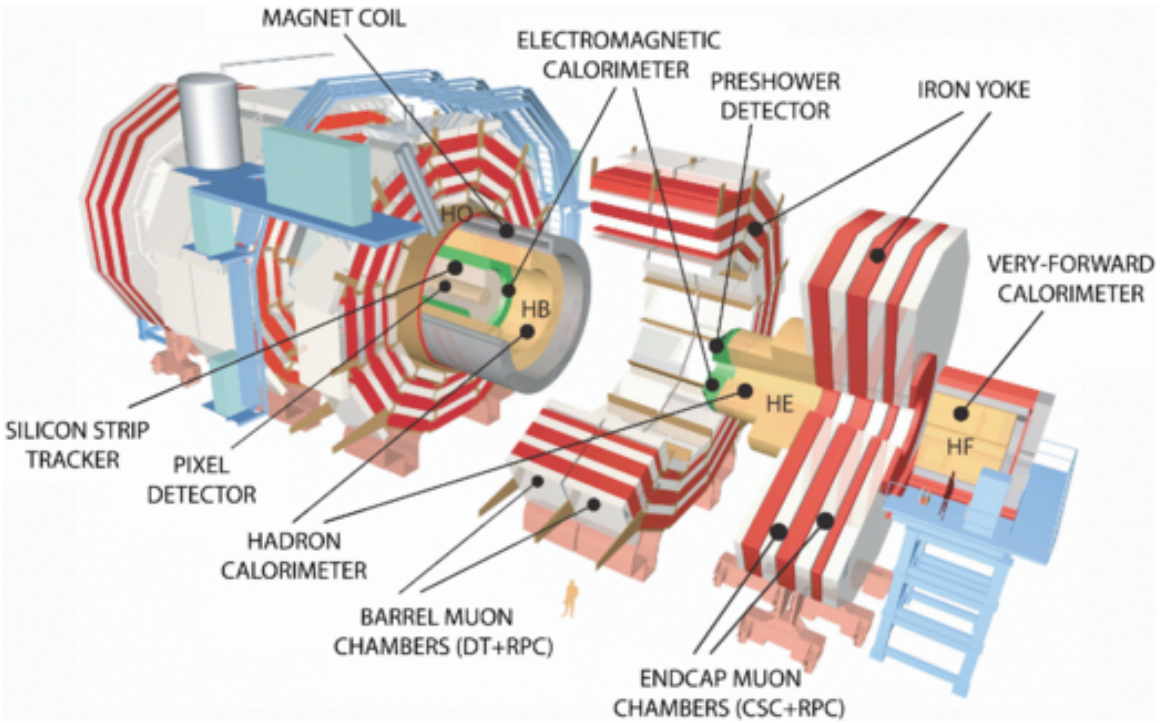


**Figure 3.9:** Layout of the CMS detector. The several subdetectors are indicated. The central region of the detector is referred as the Barrel section while the endcaps are referred as the forward sections. [67].

1095 • Hadronic calorimeter.

1096 • Muon chambers (Barrel and endcap)

1097 The central region of the detector is commonly referred as the barrel section while the  
 1098 endcaps are referred as the forward sections of the detector; thus, each subdetector  
 1099 is composed of a barrel section and a forward section.

### 1100 3.3.1 Coordinate system

1101 The coordinate system used by CMS is centered in the geometrical center of the  
 1102 detector which is the same as the CP as shown in figure 3.10. The  $z$ -axis is parallel  
 1103 to the beam direction, while the  $Y$ -axis pointing vertically upward, and the  $X$ -axis  
 1104 pointing radially inward toward the center of the LHC.

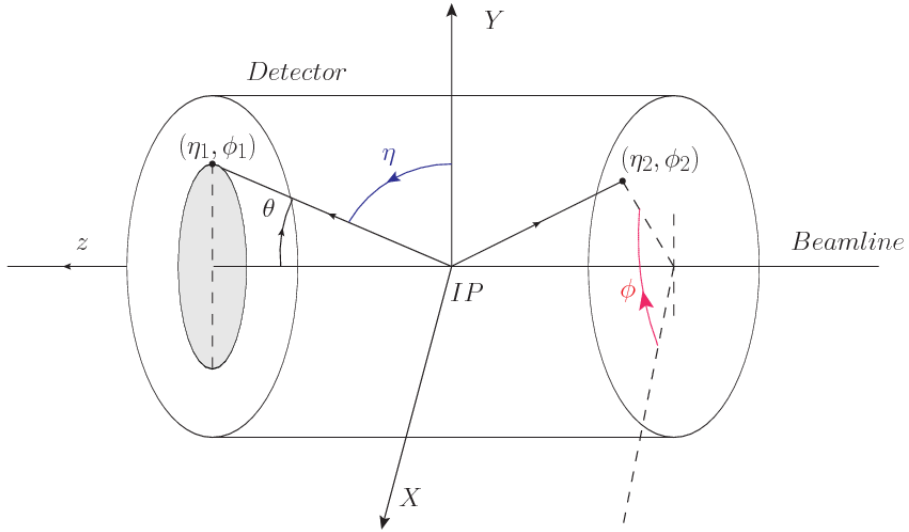


**Figure 3.10:** CMS detector coordinate system.

1105 In addition to the common cartesian and cylindrical coordinate systems, two coordi-  
 1106 nates are of particular utility in particle physics: rapidity( $y$ ) and pseudorapidity( $\eta$ ),  
 1107 defined in connection to the polar angle  $\theta$ , energy and longitudinal momentum com-  
 1108 ponent (momentum along the  $z$ -axis) according to

$$y = \frac{1}{2} \ln \frac{E + p_z}{E - p_z} \quad \eta = -\ln \left( \tan \frac{\theta}{2} \right) \quad (3.6)$$

1109 Rapidity is related to the angle between the  $XY$ -plane and the direction in which the  
 1110 products of a collision are emitted; it has the nice property that the difference between  
 1111 the rapidities of two particles is invariant with respect to Lorentz boosts along the  $z$ -  
 1112 axis. Thus, data analysis becomes more simple when based on rapidity; however, it is  
 1113 not simple to measure the rapidity of highly relativistic particles, as those produced  
 1114 after  $pp$  collisions. Under the highly relativistic motion approximation,  $y$  can be  
 1115 rewritten in terms of the polar angle, concluding that rapidity is approximately equal  
 1116 to the pseudorapidity defined above, i.e.  $y \approx \eta$ . Note that  $\eta$  is easier to measure than  $y$   
 1117 given the direct relationship between the former and the polar angle. Angular distance

1118 between two objects in the detector ( $\Delta R$ ) is defined in terms of their coordinates  
 1119  $(\eta_1, \phi_1), (\eta_2, \phi_2)$  as

$$\Delta R = \sqrt{(\Delta\eta)^2 - (\Delta\phi)^2} \quad (3.7)$$

1120 **3.3.2 Pixels detector**

1121 The CMS tracking system is designed to provide a precise measurement of the tra-  
 1122 jectory (*track*) followed by the charged particles created after the *pp* collisions; also,  
 1123 the precise reconstruction of the primary and secondary origins (*vertices*) is expected  
 1124 in an environment where, each 25 ns, the bunch crossing produce about 20 inelastic  
 1125 collisions and about 1000 particles. An increment in the luminosity is ongoing which  
 1126 implies that the PU will increase accordingly.

1127

1128 The pixel detector was replaced during the 2016-2017 extended year-end technical  
 1129 stop, due to the increasingly challenging operating conditions like the higher particle  
 1130 flow and more radiation harsh environment, among others. The new one is respond-  
 1131 ing as expected, reinforcing its crucial role in the successful way to fulfill the new  
 1132 LHC physics objectives after the discovery of the Higgs boson. The last chapter of  
 1133 this thesis is dedicated to describe my contribution to the “Forward Pixel Phase 1  
 1134 upgrade”.

1135

1136 The current pixel detector is composed of 1856 silicon pixel detector modules orga-  
 1137 nized in four-barrel layers in the central region and three disks in the forward region;  
 1138 it is designed to record efficiently and with high precision, up to  $10\mu\text{m}$  in the *XY*-  
 1139 plane and  $20\mu\text{m}$  in the *z*-direction, the first four space-points (*hits*) near to the CP  
 1140 region (see figure 3.11 left side) in the range  $|\eta| \leq 2.5$ . The first barrel layer is located

at a radius of 30 mm from the beamline, while the fourth layer is located at a radius of 160 mm closer to the strip tracker inner barrel layer (see section 3.3.3) in order to reduce the rate of fake tracks. The high granularity of the detector is represented in its about 123 Mpixels, each of size  $100 \times 150 \mu\text{m}^2$ , which is almost twice the channels of the old detector. The transverse momentum resolution of tracks can be measured with a resolution of 1-2% for muons of  $p_T = 100 \text{ GeV}$ .

1147

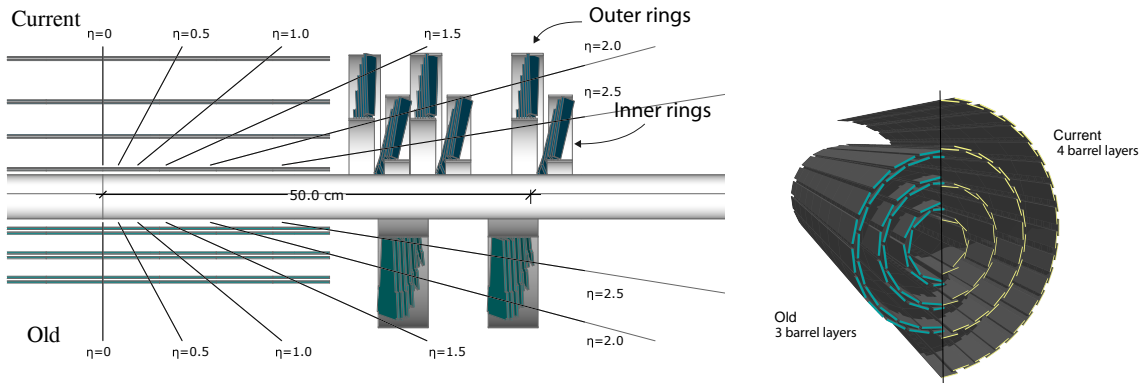


**Figure 3.11:** CMS pixel detector schematic view. Left: layout comparing the layers and disks in the old and current pixel detectors. Right: Transverse-oblique view comparing the pixel barrel layers in the two [69].

Some of the improvements with respect to the previous pixel detector include a higher average tracking efficiency and lower average fake rate as well as higher track impact parameter resolution which is fundamental in order to increase the efficiency in the identification of jets originating from b quarks (b-tagging). A significant source of improvement comes from the overall reduction in the material budget of the detector which results in fewer photon conversions and less multiple scattering from charged particles.

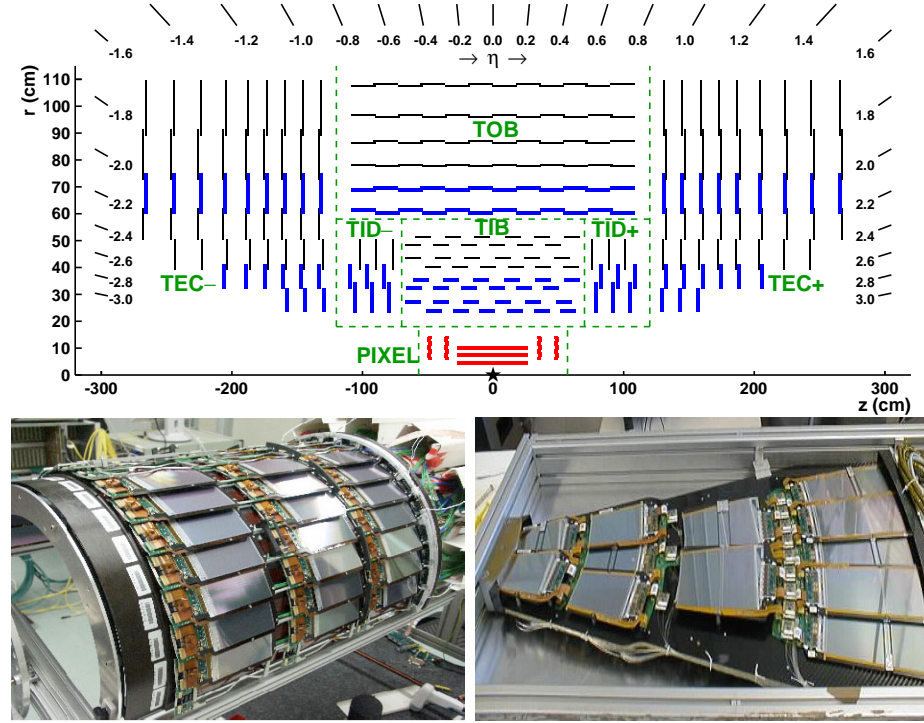


**Figure 3.12:** Top: CMS Silicon Strip Tracker (SST) schematic view. The SST is composed of the tracker inner barrel (TIB), the tracker inner disks (TID), the tracker outer barrel (TOB) and the tracker endcaps (TEC). Each part is made of silicon strip modules; the modules in blue represent two modules mounted back-to-back and rotated in the plane of the module by a stereo angle of 120 mrad in order to provide a 3-D reconstruction of the hit positions. Bottom: pictures of the TIB (left) and TEC (right) modules [70–72].

### 1155 3.3.3 Silicon strip tracker

1156 The silicon strip tracker (SST) is the second stage in the CMS tracking system. The  
 1157 top side of figure 3.12 shows a schematic of the SST. The inner tracker region is com-  
 1158 posed of the tracker inner barrel (TIB) and the tracker inner disks (TID) covering the  
 1159 region  $r < 55$  cm and  $|z| < 118$  cm. The TIB is composed of 4 layers while the TID  
 1160 is composed of 3 disks at each end. The silicon sensors in the inner tracker are 320  
 1161  $\mu\text{m}$  thick, providing a resolution of about 13–38  $\mu\text{m}$  in the  $r\phi$  position measurement.

1162

1163 The modules indicated in blue in the schematic view of figure 3.12 are two modules

1164 mounted back-to-back and rotated in the plane of the module by a “stereo” angle of  
 1165 100 mrad; the hits from these two modules, known as “stereo hits”, are combined to  
 1166 provide a measurement of the second coordinate ( $z$  in the barrel and  $r$  on the disks)  
 1167 allowing the reconstruction of hit positions in 3-D.

1168

1169 The outer tracker region is composed of the tracker outer barrel (TOB) and the  
 1170 tracker endcaps (TEC). The six layers of the TOB offer coverage in the region  $r > 55$   
 1171 cm and  $|z| < 118$  cm, while the 9 disks of the TEC cover the region  $124 < |z| < 282$   
 1172 cm. The resolution offered by the outer tracker is about 13-38  $\mu\text{m}$  in the  $r\phi$  position  
 1173 measurement. The inner four TEC disks use silicon sensors 320  $\mu\text{m}$  thick; those in  
 1174 the TOB and the outer three TEC disks use silicon sensors of 500  $\mu\text{m}$  thickness. The  
 1175 silicon strips run parallel to the  $z$ -axis and the distance between strips varies from 80  
 1176  $\mu\text{m}$  in the inner TIB layers to 183  $\mu\text{m}$  in the inner TOB layers; in the endcaps the  
 1177 wedge-shaped sensors with radial strips, whose pitch range between 81  $\mu\text{m}$  at small  
 1178 radii and 205  $\mu\text{m}$  at large radii.

1179

1180 The whole SST has 15148 silicon modules, 9.3 million silicon strips and cover a total  
 1181 active area of about 198  $\text{m}^2$ .

### 1182 3.3.4 Electromagnetic calorimeter

1183 The CMS electromagnetic calorimeter (ECAL) is designed to measure the energy of  
 1184 electrons and photons. It is composed of 75848 lead tungstate crystals which have a  
 1185 short radiation length (0.89 cm) and fast response, since 80% of the light is emitted  
 1186 within 25 ns; however, they are combined with Avalanche photodiodes (APDs) as  
 1187 photodetectors given that crystals themselves have a low light yield ( $30\gamma/\text{MeV}$ ). A

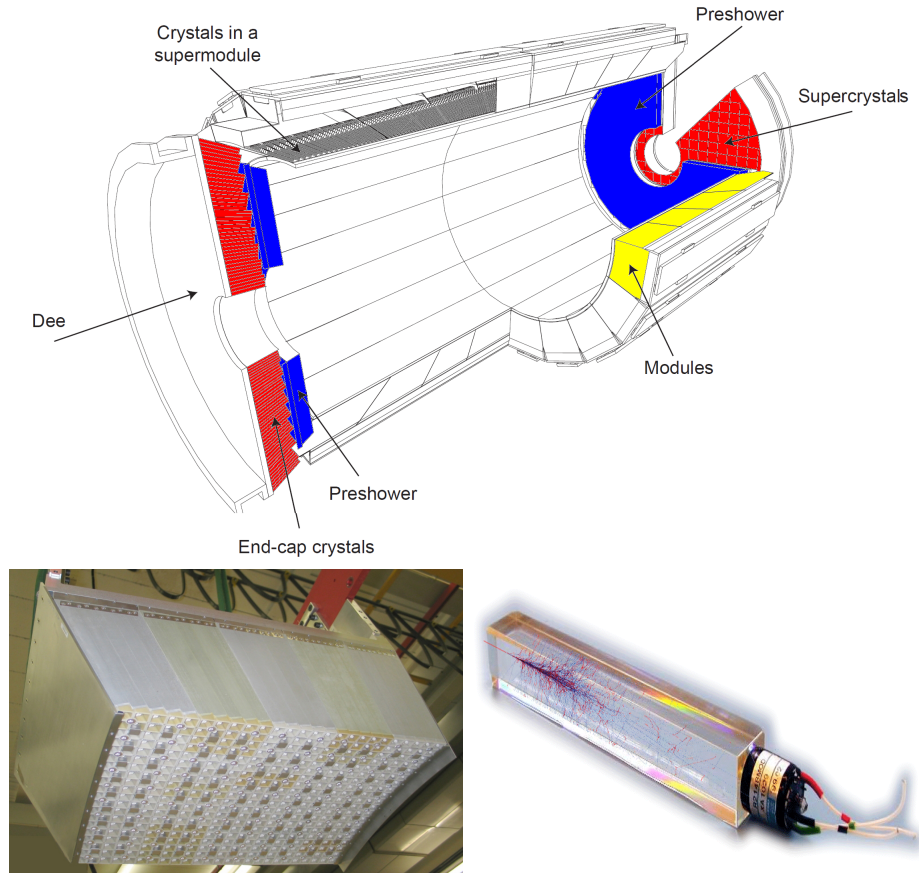


**Figure 3.13:** Top: CMS ECAL schematic view. Bottom: Module equipped with the crystals (left); ECAL crystal(right).

1188 schematic view of the ECAL is shown in figure 3.13.

1189

1190 Energy is measured when electrons and photons are absorbed by the crystals which  
 1191 generates an electromagnetic “shower”, as seen in bottom right picture of the fig-  
 1192 ure3.13; the shower is seen as a *cluster* of energy which depending on the amount  
 1193 of energy deposited can involve several crystals. The ECAL barrel (EB) covers the  
 1194 region  $|\eta| < 1.479$ , using crystals of depth of 23 cm and  $2.2 \times 2.2 \text{ cm}^2$  transverse  
 1195 section; the ECAL endcap (EE) covers the region  $1.479 < |\eta| < 3.0$  using crystals  
 1196 of depth 22 cm and transverse section of  $2.86 \times 2.86 \text{ cm}^2$ ; the photodetectors used

1197 are vacuum phototriodes (VPTs). Each EE is divided in two structures called “Dees”.

1198

1199 In front of the EE, it is installed the preshower detector (ES) which covers the region  
 1200  $1.653 < |\eta| < 2.6$ . The ES provides a precise measurement of the position of electro-  
 1201 magnetic showers, which allows to distinguish electrons and photons signals from  $\pi^0$   
 1202 decay signals. The ES is composed of a layer of lead absorber followed by a layer of  
 1203 plastic scintillators

### 1204 3.3.5 Hadronic calorimeter

1205 Hadrons are not absorbed by the ECAL but by the hadron calorimeter (HCAL),  
 1206 which is made of a combination of alternating brass absorber layers and silicon photo-  
 1207 multiplier(SiPM) layers; therefore, particles passing through the scintillator material  
 1208 produce showers, as in the ECAL, as a result of the inelastic scattering of the hadrons  
 1209 with the detector material. Since the particles are not absorbed in the scintillator,  
 1210 their energy is sampled; therefore the total energy is not measured but estimated from  
 1211 the energy clusters, which reduce the resolution of the detector. Brass was chosen  
 1212 as the absorber material due to its short interaction length ( $\lambda_I = 16.42\text{cm}$ ) and its  
 1213 non-magnetivity. Figure 3.14 shows a schematic view of the CMS HCAL.

1214

1215 The HCAL is divided into four sections; the Hadron Barrel (HB), the Hadron Outer  
 1216 (HO), the Hadron Endcap (HE) and the Hadron Forward (HF) sections. The HB  
 1217 covers the region  $0 < |\eta| < 1.4$ , while the HE covers the region  $1.3 < |\eta| < 3.0$ . The HF,  
 1218 made of quartz fiber scintillator and steel as absorption material, covers the forward  
 1219 region  $3.0 < |\eta| < 5.2$ . Both the HB and HF are located inside the solenoid. The HO  
 1220 is placed outside the magnet as an additional layer of scintillators with the purpose

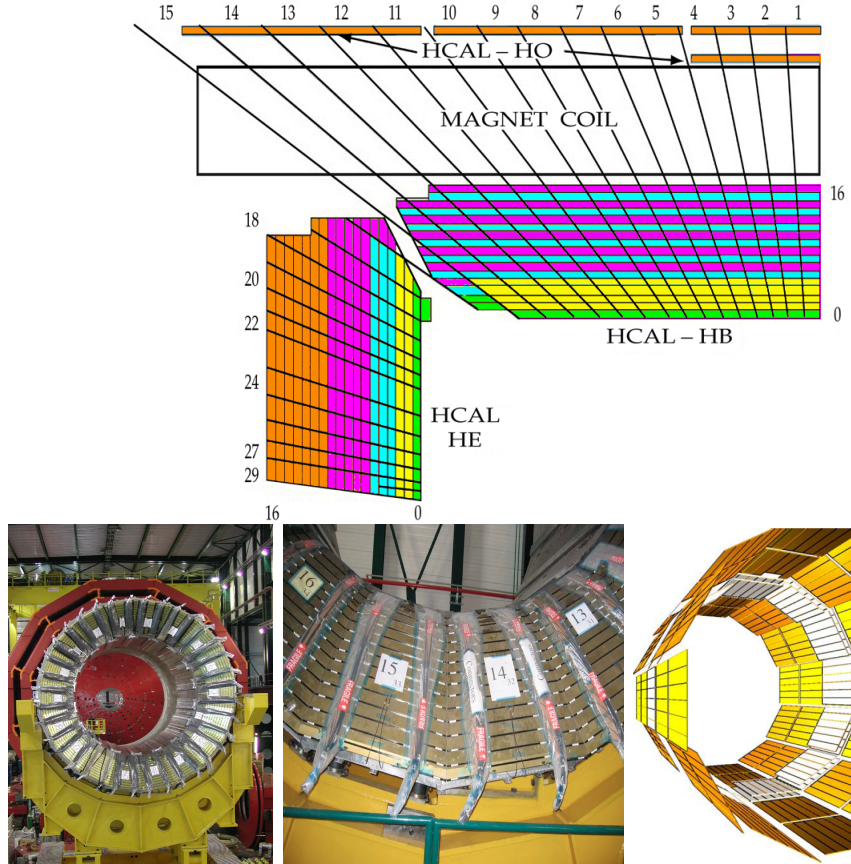


**Figure 3.14:** Top: CMS HCAL schematic view, the colors indicate the layers that are grouped into the same readout channels. Bottom: picture of a section of the HB; the absorber material is the golden region and scintillators are placed in between the absorber material (left and center). Schematic view of the HO (right). [73,74]

of measure the energy tails of particles passing through the HB and the magnet (see figure 3.14 top and bottom right). The upgrades made to the HCAL during the technical stop 2016-2017 consisted in the replacement of the photo transducer, in order to improve the efficiency.

### 3.3.6 Superconducting solenoid magnet

The superconducting magnet installed in the CMS detector is designed to provide an intense and highly uniform magnetic field in the central part of the detector. In

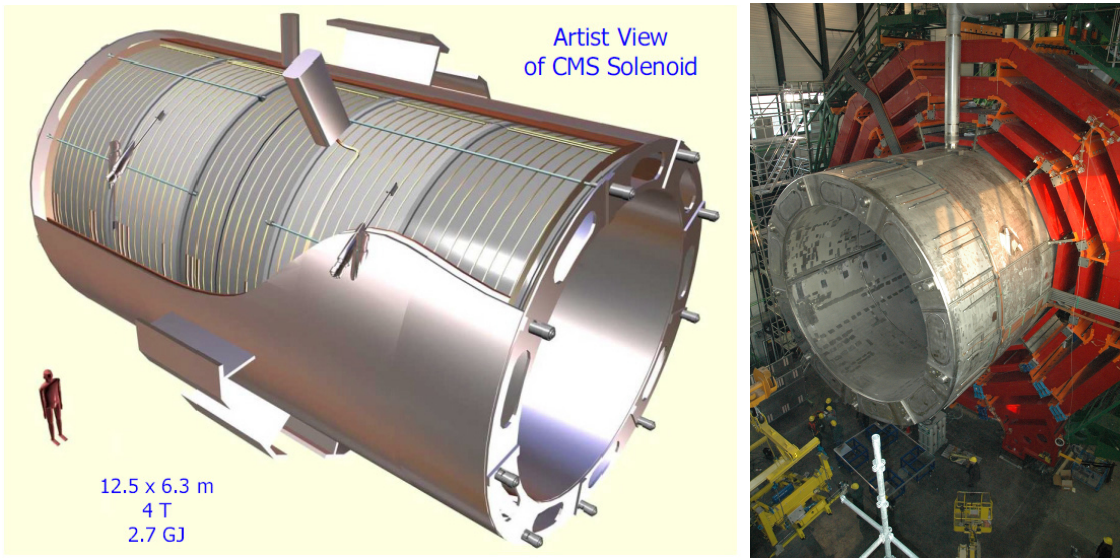


**Figure 3.15:** Artistic representation of the CMS solenoid magnet(left). The magnet is supported on an iron yoke (right) which also serves as the house of the muon detector and as mechanical support for the whole CMS detector [68].

fact, the tracking system takes advantage of the bending power of the magnetic field to measure with precision the momentum of the particles that traverse it; the unambiguous determination of the sign for high momentum muons was a driven principle during the design of the magnet. The magnet has a diameter of 6.3 m, a length of 12.5 m and a cold mass of 220 t; the generated magnetic field reaches a strength of 3.8T. Since it is made of Ni-Tb superconducting cable it has to operate at a temperature of 4.7 K by using a helium cryogenic system; the current circulating in the cables reaches 18800 A under normal running conditions. The left side of figure 3.15 shows an artistic view of the CMS magnet, while the right side shows a transverse view of the cold mass where the winding structure is visible.

1238

1239 The yoke (see figure 3.15), composed of 5 barrel wheels and 6 endcap disks made  
 1240 of iron, serves not only as the media for magnetic flux return but also provides the  
 1241 house for the muon detector system and structural stability to the full detector.

1242 **3.3.7 Muon system**

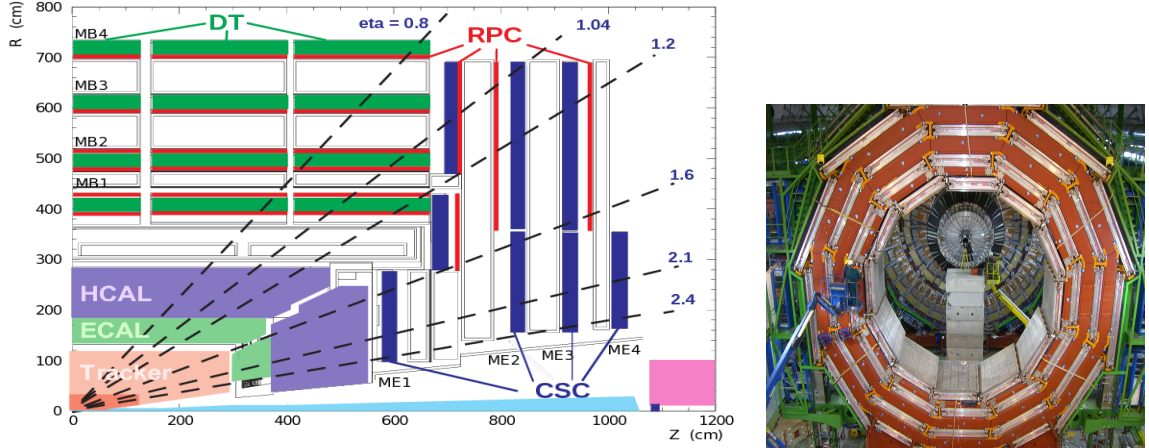


**Figure 3.16:** Left: CMS muon system schematic view; Right: one of the yoke rings with the muon DTs and RPCs installed; in the back it is possible to see the muon endcap [75].

1243 Muons are the only charged particles able to pass through all the CMS detector due  
 1244 to their low ionization energy loss; thus, muons can be separated easily from the  
 1245 high amount of particles produced in a  $pp$  collision. Also, muons are expected to be  
 1246 produced in the decay of several new particles; therefore, a good detection of muons  
 1247 was on the leading principles when designing the CMS detector.

1248

1249 The CMS muon detection system is embedded in the return yoke as seen in figure  
 1250 3.16. It is composed of three different detector types, the drift tube chambers (DT),  
 1251 Cathode strip chambers (CSC), and resistive plate chambers (RPC); DT are located  
 1252 in the central region  $\eta < 1.2$  arranged in four layers of drift chambers filled with an  
 1253 Ar/CO<sub>2</sub> gas mixture.

1254

1255 The muon endcaps are made of CSCs covering the region  $\eta < 2.4$  and filled with a  
 1256 mixture of Ar/CO<sub>2</sub>/CF<sub>4</sub>. The reason behind using a different detector type lies on  
 1257 the different conditions in the forward region like the higher muon rate and higher

1258 residual magnetic field compared to the central region.

1259

1260 The third type of detector used in the muon system is a set of four disks of RPCs  
1261 working in avalanche mode. The RPCs provide good spatial and time resolutions.

1262 The track of  $high - p_T$  muon candidates is built combining information from the  
1263 tracking system and the signal from up to six RPCs and four DT chambers.

1264 The muon tracks are reconstructed from the hits in the several layers of the muon  
1265 system.

### 1266 3.3.8 CMS trigger system

1267 Under normal conditions, CMS expects  $pp$  collisions every 25 ns i.e. an interaction  
1268 rate of 40 MHz for which it is not possible to store the recorded data in full. In order  
1269 to handle this high event rate data, an online event selection, known as triggering, is  
1270 performed; triggering reduce the event rate to 100 Hz for storage and further offline  
1271 analysis.

1272

1273 The trigger system starts with a reduction of the event rate to 100 kHz in the so-called  
1274 “level 1 trigger (L1)”. L1 is based on dedicated programmable hardware like Field  
1275 Programmable Gate Arrays (FPGAs) and Application Specific Integrated Circuits  
1276 (ASICs), partly located in the detector itself; another portion is located in the CMS  
1277 under-ground cavern. Hit patterns information from the muon chambers and the en-  
1278 ergy deposits in the calorimeter are used to decide if an event is accepted or rejected,  
1279 according to selection requirements previously defined, which reflect the interesting  
1280 physics processes. Figure 3.17 shows the L1 trigger architecture

1281

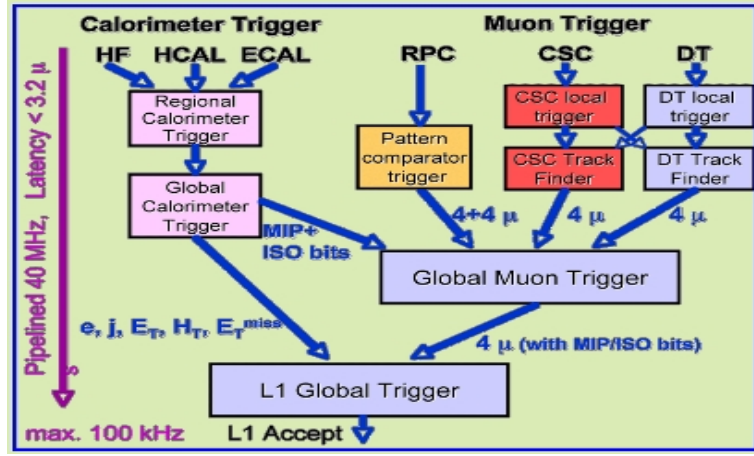


Figure 3.17: CMS Level-1 trigger architecture [76].

1282 The second stage in the trigger system is called “high-level trigger (HLT)”; events  
 1283 accepted by L1 are passed to HLT in order to make an initial reconstruction of them.  
 1284 HLT is software based and runs on a dedicated server farm, using selection algo-  
 1285 rithms and high-level object definitions; the event rate at HLT is reduced to 100 Hz.  
 1286 The first HLT stage takes information from the muon detectors and the calorimeters  
 1287 to make the initial object reconstruction; in the next HLT stage, information from  
 1288 the pixel and strip detectors is used to do first fast-tracking and then full tracking  
 1289 online. This initial object reconstruction is used in further steps of the trigger system.

1290

1291 Events and preliminary reconstructed physics objects from HLT are sent to be fully  
 1292 reconstructed at the CERN computing center. Again, the pixel detector information  
 1293 provides high-quality seeds for the track reconstruction algorithm offline, primary ver-  
 1294 tex reconstruction, electron and photon identification, muon reconstruction,  $\tau$  iden-  
 1295 tification, and b-tagging. After full reconstruction, data sets are made available for  
 1296 offline analyses.

1297

1298 During the 2016-2017 technical stop, the L1 system was updated in order to improve

1299 the physics object identification by improving the algorithms and accounting for the  
 1300 increasing pile-up scenario.

1301 **3.3.9 CMS computing**

1302 After the data, coming from the experiment, are processed at several levels, they have  
 1303 to be stored and made available for further analysis; in order to cope all the tasks  
 1304 implied in the offline data processing, like transfer, simulation, reconstruction and  
 1305 reprocessing, among others, a big computing power is required. The CMS computing  
 1306 system is based on the distributed architecture concept, where users of the system  
 1307 and physical computer centers are distributed worldwide and interconnected by high-  
 1308 speed networks.

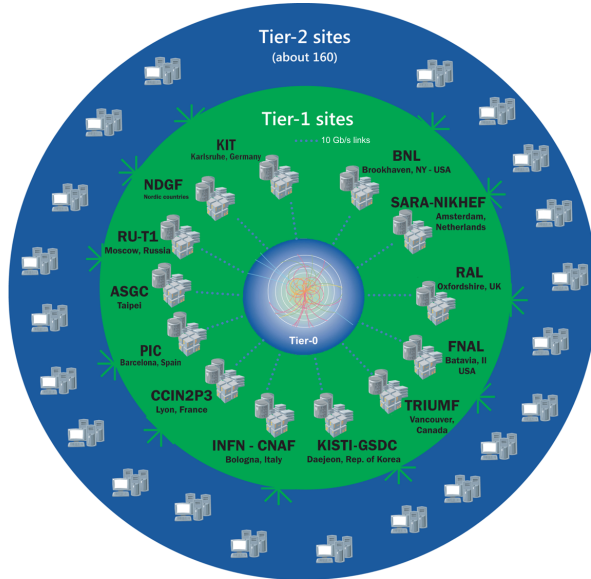


**Figure 3.18:** WLCCG structure. The primary computer centers (Tier-0) are located at CERN (data center) and at the Wigner datacenter in Budapest. Tier-1 is composed of 13 centers and Tier-2 is composed of about 160 centers. [77].

1309 The worldwide LHC computing grid (WLCCG) is the mechanism used to provide that  
 1310 distributed environment. WLCCG is a tiered structure connecting computing centers

1311 around the world, which provides the necessary storage and computing facilities. The  
1312 primary computing centers of the WLCG are located at the CERN and the Wigner  
1313 datacenter in Budapest and are known as Tier-0 as shown in figure 3.18. The main  
1314 responsibilities for each tier level are [77]

1315 • **Tier-0:** initial reconstruction of recorded events and storage of the resulting  
1316 datasets, the distribution of raw data to the Tier-1 centers.

1317 • **Tier-1:** provide storage capacity, support for the Grid, safe-keeping of a pro-  
1318 portional share of raw and reconstructed data, large-scale reprocessing and safe-  
1319 keeping of corresponding output, generation of simulated events, distribution  
1320 of data to Tier 2s, safe-keeping of a share of simulated data produced at these  
1321 Tier 2s.

1322 • **Tier-2:** store sufficient data and provide adequate computing power for specific  
1323 analysis tasks, provide analysis requirements and proportional share of simu-  
1324 lated event production and reconstruction.

1325 Aside from the general computing strategy to manage the huge amount of data pro-  
1326 duced by experiments, CMS uses a framework to perform a variety of processing,  
1327 selection and analysis tasks. The central concept of the CMS data model referred to  
1328 as “event data model” (EDM) is the “Event”; therefore, an event is the unit that con-  
1329 tains the information from a single bunch crossing as well as any data derived from  
1330 that information like the reconstructed objects, the details under which additional  
1331 data are derived.

1332

1333 Events are passed as the input to the “physics modules” that obtain information from  
1334 them and create new one; for instance, “event data producers” add new data into the

1335 events, “analyzers” produce an information summary from an event set, “filters” per-  
1336 form selection and triggering.

1337

1338 CMS uses several event formats with different levels of detail and precision

1339 • **Raw format:** events in this format contain the full recorded information from  
1340 the detector as well as trigger decision and other metadata. An extended version  
1341 of raw data is used to store information from the CMS Monte Carlo simulation  
1342 tools. Raw data are stored permanently, occupying about 2MB/event

1343 • **RECO format:** events in this format correspond to raw data that have been  
1344 submitted to reconstruction algorithms like primary and secondary vertex re-  
1345 construction, particle ID, track-finding. RECO events contain physical objects  
1346 and all the information used to reconstruct them; average size is about 0.5  
1347 MB/event.

1348 • **AOD format:** Analysis Object Data (AOD) is the data format used in the  
1349 physics analyses given that it contains the parameters describing the high-level  
1350 physics objects in addition to enough information to allow a kinematic refitting if  
1351 needed. AOD events are filtered versions of the RECO events to which skimming  
1352 or other kind processes have been applied. Requires about 100 kB/event.

1353 • **Non-event data** are data needed to interpret and reconstruct events. Some  
1354 of the non-event data used by CMS contains information about the detector  
1355 contraction and condition data like calibrations, alignment, and detector status.

1356 Figure 3.19 shows the data flow scheme between CMS detector and hardware tiers.

1357 The whole collection of software built as a framework is referred to as “CMSSW”. This  
1358 framework provides the services needed by the simulation, calibration and alignment,

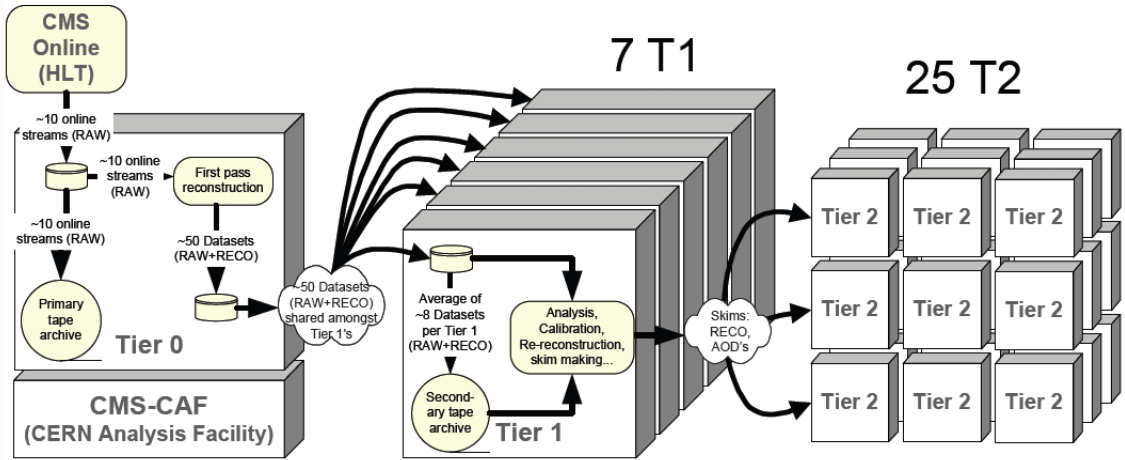


**Figure 3.19:** Data flow from CMS detector through hardware Tiers.

1359 and reconstruction modules that process event data, so that physicists can perform  
 1360 analysis. The CMSSW event processing model is composed of one executable, called  
 1361 cmsRun, and several plug-in modules which contain all the tools (calibration, recon-  
 1362 struction algorithms) needed to process an event. The same executable is used for  
 1363 both detector and Monte Carlo data [78].

1364 **Chapter 4**

1365 **Event generation, simulation and  
1366 reconstruction**

1367 The process of analyzing the data recorded by the CMS experiment involves several  
1368 stages where the data are processed in order to interpret the information provided by  
1369 all the detection systems; in those stages the particles produced after the  $pp$  collision  
1370 are identified by reconstructing their trajectories and measuring their features. In  
1371 addition, the SM provides a set of predictions that have to be compared with the  
1372 experimental results; however, in most of the cases, theoretical predictions are not  
1373 directly comparable to experimental results due to the diverse source of uncertainties  
1374 introduced by the experimental setup and theoretical approximations among others.

1375

1376 The strategy to face these conditions consist in using statistical methods implemented  
1377 in computational algorithms to produce numerical results that can be contrasted with  
1378 the experimental results. These computational algorithms are commonly known as  
1379 Monte Carlo (MC) methods and, in the case of particle physics, they are designed to  
1380 apply the SM rules and produce predictions about the physical observables measured

in the experiments. Since particle physics is governed by quantum mechanics principles, predictions are not allowed for single events; therefore, a high number of events are “generated” and predictions are produced in the form of statistical distributions for the observables. Effects of the detector presence are included in the predictions by introducing simulations of the detector itself.

1386

1387 This chapter presents a description of the event generation strategy and the tools  
 1388 used to perform the detector simulation and physics objects reconstruction. A com-  
 1389 prehensive review on event generators for LHC physics can be found in reference [79]  
 1390 on which this chapter is based.

## 1391 4.1 Event generation

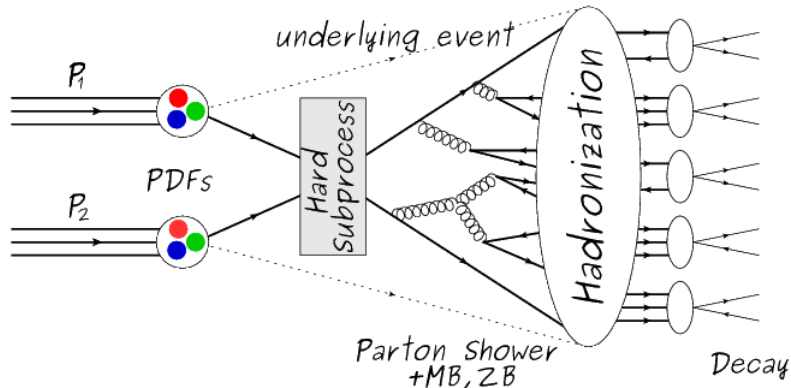


**Figure 4.1:** Event generation process. In the first step, the PDF of the colliding particles is considered so the specific interaction is described. The actual interaction is generated in the hard subprocess; the cross section of the process is calculated from the matrix element connecting the initial and final states. The parton shower describes the evolution of the partons from the hard subprocess according to the DGLAP equations. At this step the underlying event and PU effects are included in the generation. The resulting partons from the parton shower are recombined to form hadrons in the hadronization step; most of them are unstable, therefore, their decays are also generated in agreement to the known branching ratios. Modified from reference [80].

1392 The event generation is intended to create events that mimic the behavior of actual  
 1393 events produced in the collisions; they obey a sequence of steps from the particles colli-  
 1394 sion hard process to the decay process into the final state particles. Figure 4.1 shows  
 1395 an schematic view of the event generation process; the fact that the full process can  
 1396 be treated as several independent steps is based on the QCD factorization theorem.

1397

1398 Generation starts by taking into account the PDFs of the incoming particles. Event  
 1399 generators offer the option to chose from several PDF sets depending on the partic-  
 1400 ular process under simulation<sup>1</sup>; in the following  $pp$  collisions will be considered. The  
 1401 *hard subprocess* describes the actual interaction between partons from the incoming  
 1402 protons; it is represented by the matrix element connecting the initial and final states  
 1403 of the interaction. Normally, the matrix element can be written as a sum over Feyn-  
 1404 man diagrams and consider interferences between terms in the summation. During  
 1405 the generation of the hard subprocess, the production cross section is calculated.

1406

1407 The order to which the cross section is calculated depends on the order of the Feyn-  
 1408 man diagrams involved in the calculation; therefore, radiative corrections are included  
 1409 by considering a higher order Feynman diagrams where QCD radiation dominates.  
 1410 Currently, cross sections calculated to LO do not offer a satisfactory description of the  
 1411 processes, i.e., the results are only reliable for the shape of distributions; therefore,  
 1412 NLO calculations have to be performed with the implication that the computing time  
 1413 needed is highly increased.

1414

1415 The final parton content of the hard subprocess is subjected to the *parton shower*  
 1416 which generates the gluon radiation. Parton shower evolves the partons; i.e., glouns

---

<sup>1</sup> Tool in Reference [81] allows to plot different PDF sets under customizable conditions.

1417 split into quark-antiquark pairs and quarks of enough energy radiate gluons giving rise  
 1418 to further parton multiplication, following the DGLAP (Dokshitzer-Gribov-Lipatov-  
 1419 Altarelli-Parisi) equations. Showering continues until the energy scale is low enough  
 1420 to reach the non-perturbative limit.

1421

1422 In the simulation of LHC processes that involve  $b$  quarks like the single top quark or  
 1423 Higgs associated production, it is needed to consider that the  $b$  quark is heavier than  
 1424 the proton; in this sense, the QCD interaction description is made in two different  
 1425 schemes [82]

1426 • four-flavor (4F) scheme.  $b$  quarks appears only in the final state because they  
 1427 are heavier than the proton and therefore they can be produced only from the  
 1428 splitting of a gluon into pairs or singly in association with a  $t$  quark in high  
 1429 energy-scale interactions. During the simulation, the  $b$ -PDFs are set to zero  
 1430 because it cannot be part of the proton. Calculation in this scheme are more  
 1431 complicated due to the presence of the second  $b$  quark but the full kinematics is  
 1432 considered already at LO and therefore the accuracy of the description is better.

1433 • five-flavor (5F) scheme.  $b$  quarks are considered massless, therefore they can  
 1434 appear in both initial and final states since it can now be part of the proton; thus,  
 1435 during the simulation  $b$ -PDFs are not set to zero. In this scheme, calculations  
 1436 are simpler than in the 4F scheme and possible logarithmic divergences are  
 1437 absorbed by the PDFs through the DGLAP evolution.

1438 In this thesis, the  $tHq$  events are generated using the 4F scheme in order to reduce  
 1439 uncertainties, while the  $tHW$  events are generated using the 5F scheme to eliminate  
 1440 LO interference with the  $t\bar{t}H$  process [48].

1441

1442 Partons involved in the  $pp$  collision are the focus of the simulation, however, the rest  
 1443 of the partons inside the incoming protons are also affected because the remnants are  
 1444 colored objects; also, multiple parton interactions can occurs. The hadronization of  
 1445 the remnants and multiple parton interactions are known as “underlying event” and  
 1446 it has to be included in the simulation. In addition, multiple  $pp$  collisions in the same  
 1447 bunch crossing (pile-up mentioned in 3.2) occurs, actually in two forms

- 1448 • *in-time PU* which refers to multiple  $pp$  collision in the bunch crossing but that  
 1449 are not considered as primary vertices.
- 1450 • *Out-of-time PU* which refers to overlapping  $pp$  collisions from consecutive bunch  
 1451 crossings; this can occurs due to the time-delays in the detection systems where  
 1452 information from one bunch crossing is assigned to the next or previous one.

1453 While the underlying event effects are included in generation using generator-specific  
 1454 tools, PU effects are added to the generation by overlying Minimum-bias (MB) and  
 1455 Zero-bias (ZB) events to the generated events. MB events are inelastic events selected  
 1456 by using a loose (minimum bias) trigger with as little bias as possible, therefore ac-  
 1457 cepting a large fraction of the overall inelastic event; ZB events correspond to random  
 1458 events recorded by the detector when collisions are likely. MB model in-time PU and  
 1459 ZB model out-of-time PU.

1460

1461 The next step in the generation process is called “hadronization”. Since particles  
 1462 with a net color charge are not allowed to exits isolated, they have recombine to form  
 1463 bound states. This is precisely the process by which the partons resulting from the  
 1464 parton shower arrange themselves as color singlets to form hadrons. At this step, the  
 1465 energy-scale is low and the strong coupling constant is large, therefore hadronization  
 1466 process is non-perturbative and phenomenological model are used to describe the

1467 parton’s evolution. Most of the baryons and mesons produced in the hadronization  
 1468 are unstable and hence they will decay in the detector.

1469

1470 The last step in the generation process corresponds to the decay of the unstable  
 1471 particles generated during hadronization; it is also simulated in the hadronization  
 1472 step, based on the known branching ratios.

## 1473 4.2 Monte Carlo Event Generators.

1474 The event generation described in the previous section has been implemented in  
 1475 several software packages for which a brief description is given.

- 1476     • **PYTHIA 8.** It is a program designed to perform the generation of high en-  
   1477       ergy physics events which describe the collisions between particles such as elec-  
   1478       trons, protons. Several theories and models are implemented in it, in order to  
   1479       describe physical aspects like hard and soft interaction, parton distributions,  
   1480       initial and final-state parton showers, multiple parton interactions, beam rem-  
   1481       nants, hadronization<sup>2</sup> and particle decay. Thanks to extensive testing, several  
   1482       optimized parametrizations known as “tunnings” have been defined in order  
   1483       to improve the description of actual collisions to a high degree of precision; for  
   1484       analysis at  $\sqrt{s} = 13$  TeV, the underline event CUETP8M1 tune is employed [84].  
   1485       The calculation of the matrix element is performed at LO which is not enough  
   1486       for the current required level of precision; therefore, pythia is often used for  
   1487       parton shower, hadronization, decays, while other event generators are used to  
   1488       generate the matrix element at NLO.

---

<sup>2</sup> based in the Lund string model [83]

1489     • **MadGraph5\_aMC@NLO.** MadGraph is a matrix element generator which  
 1490       calculates the amplitudes for all contributing Feynman diagrams of a given pro-  
 1491       cess but does not provide a parton shower while MC@NLO incorporate NLO  
 1492       QCD matrix elements consistently into a parton shower framework; thus, Mad-  
 1493       Graph5\_aMC@NLO, as a merger of the two event generators MadGraph5 and  
 1494       aMC@NLO, is an event generator capable to calculate tree-level and NLO cross  
 1495       sections and perform the matching of those with the parton shower. It is one  
 1496       of the most frequently used matrix element generators; however, it has as par-  
 1497       ticular feature the presence of negative event weights which reduce the number  
 1498       of events used to reproduce the the properties of the objects generated [85].

1499

1500     • **POWHEG.** It is an NLO matrix element generator where the hardest emis-  
 1501       sion of color charged particles is generated in such a way that the negative event  
 1502       weights issue of MadGraph5\_aMC@NLO is overcome; however, the method re-  
 1503       quires an interface with  $p_T$ -ordered parton shower or a parton shower generator  
 1504       where this highest emission can be vetoed in order to avoid double counting of  
 1505       this highest-energetic emission. PYTHIA is a commonly matched to POWHEG  
 1506       event generator [86].

1507   Events resulting from the whole generation process are known as MC events.

### 1508   **4.3 CMS detector simulation.**

1509   After generation, MC events contain the physics of the collisions but they are not  
 1510   ready to be compared to the events recorded by the experiment since these recorded  
 1511   events correspond to the response of the detection systems to the interaction with the

1512 particles traversing them. The simulation of the CMS detector have to be applied on  
1513 top of the event generation; it is simulated with Geant4, a MC toolkit for the simula-  
1514 tion of particles passing though matter which is also able to simulates the electronic  
1515 signals that would be measured by all detectors inside CMS.

1516

1517 The simulation takes the generated particles contained in the MC events as input,  
1518 makes them to pass through the simulated geometry, and models physics processes  
1519 that particles experience during their passage through matter. The full set of results  
1520 from particle-matter interactions correspond to the simulated hit which contains in-  
1521 formation about the energy loss, momentum, position. Particles of the input event  
1522 are called “primary”, while the particles originating from GEANT4-modeled interac-  
1523 tions of a primary particle with matter are called a “secondary”. Simulated hits are  
1524 the input of subsequent modules that emulate the response of the detector readout  
1525 system and triggers. The output from the emulated detection systems and triggers is  
1526 known as digitization [87, 88].

1527

1528 The modeling of the CMS detector corresponds to the accurate modeling of the inter-  
1529 action among particles, the detector material and the magnetic field. This simulation  
1530 procedure includes the following standard steps

- 1531     • Modeling of the Interaction Region.
- 1532     • Modeling of the particle passage through the hierarchy of volumes that compose  
1533        CMS detector and of the accompanying physics processes.
- 1534     • Modeling of the effect of multiple interactions per beam crossing and/or the  
1535        effect of events overlay ( Pile-Up simulation).

1536        • Modeling of the detector’s electronics response, signal shape, noise, calibration  
 1537            constants (digitization).

1538      In addition to the full simulation, i.e. a detailed detector simulation, a faster simula-  
 1539      tions (FastSim) have been developed, that may be used where much larger statistics  
 1540      are required. In FastSim, detector material effects are parametrized and included in  
 1541      the hits; those hits are used as input of the same higher-level algorithms<sup>3</sup> used to an-  
 1542      alyze the recorded events. In this way, comparisons between fast and full simulations  
 1543      can be performed [90].

1544

1545      After the full detector simulation, the output events can be directly compared with  
 1546      events actually recorded in the CMS detector. The collection of MC events that  
 1547      reproduce the expected physics for a given process are known as MC samples.

## 1548      4.4 Event reconstruction.

1549      In contrast to MC samples for which all the particles’ information is available from  
 1550      it’s identity to it’s mass and energy, recorded events contain the electronic signals,  
 1551      provided by the CMS detection systems, encoding the interaction of physical parti-  
 1552      cles with the detector matter; these electronic signals have to be combined in order  
 1553      to identify these particle and measure its features i.e., particles have to be “recon-  
 1554      structed” using the signals provided by the detection systems. The CMS experiment  
 1555      use the “particle-flow event reconstruction algorithm (PF)” to do reconstruction of  
 1556      particles produced in  $pp$  collisions. Next sections will present a basic description of  
 1557      the *Elements* used by PF: tracker tracks, energy clusters and muon tracks.

---

<sup>3</sup> track fitting, calorimeter clustering, b tagging, electron identification, jet reconstruction and calibration, trigger algorithms which will be considered in the next sections

1558 **4.4.1 Particle-Flow Algorithm.**

1559 Each of the several subdetection systems of the CMS detector is dedicated to identify  
 1560 specific type of particles, i.e., photons and electrons are absorbed by the ECAL and  
 1561 their reconstruction is based on ECAL information; hadrons are reconstructed from  
 1562 clusters in the HCAL while muons are reconstructed from hits in the muon chambers.  
 1563 PF is designed to correlate signals from all the detector layers (tracks and energy  
 1564 clusters) in order to reconstruct and identify each final state particle and its properties.  
 1565 For instance, a charged hadron is identified by a geometrical connection, know as *link*  
 1566 between one or more calorimeter clusters and a track in the tracker provided there  
 1567 are no hits in the muon system; combining several measurements allows a better  
 1568 determination of the energy and charge sign of the charged hadron.

1569 **Charged-particle track reconstruction.**

1570 The strategy used by PF in order to reconstruct tracks is called “Iterative Tracking”  
 1571 which occurs in four steps

- 1572     • Seed generation where initial track candidates are found by looking for combina-  
 1573       tion of hits in the pixel detector, strip tracker and muon chambers. In total ten  
 1574       iterations are performed, each one with a different seeding requirement. Seeds  
 1575       are used to estimate the trajectory parameters and uncertainties at the time of  
 1576       the full track reconstruction. Seeds are also considered track candidates.
- 1577     • Track finding using a tracking software known as Combinatorial Track Finder  
 1578       (CTF) [93]. The seed trajectories are extrapolated along the expected flight  
 1579       path of a charged particle, in agreement to the the trajectory parameters ob-  
 1580       tained in the first step, in an attempt to find additional hits that can be assigned  
 1581       to the track candidates.

1582     • Track-fitting where the found tracks are passed as input to a module which  
 1583       provides the best estimate of the parameters of each trajectory.

1584     • Track selection where track candidates are submitted to a selection which dis-  
 1585       cards those that fail a set of defined quality criteria.

1586 Iterations differ in the seeding configuration and the final track selection as elaborated  
 1587 in references [91, 92]. In the first iteration, high  $p_T$  tracks and tracks produced near  
 1588 to the interaction region are identified and those hits are masked thereby reducing  
 1589 the combinatorial complexity. Next iterations search for more complicated tracks,  
 1590 like low  $p_T$  tracks and tracks from b hadron decays, which tend to be displaced from  
 1591 the interaction region.

1592 **Calorimeter clustering.**

1593 After traversing the CMS tracker system, electrons, photons and hadrons deposit their  
 1594 energy in the ECAL and HCAL cells. The PF clustering algorithm aims to provide  
 1595 a high detection efficiency even for low-energy particles and an efficient distinction  
 1596 between close energy deposits. The clustering runs independently in the ECAL barrel  
 1597 and endcaps, HCAL barrel and endcaps, and the two preshower layers, following two  
 1598 steps

1599     • cells with an energy larger than a given seed threshold and larger than the energy  
 1600       of the neighboring cells are identified as cluster seeds. The neighbor cells are  
 1601       those that either share a side with the cluster seed candidate, or the eight closest  
 1602       cells including cells that only share a corner with the seed candidate.

1603     • cells with at least a corner in common with a cell already in the cluster seed  
 1604       and with an energy above a cell threshold are grouped into topological clusters.

1605 Clusters formed in this way are known as *particle-flow clusters*. With this clustering  
 1606 strategy it is possible detect and measure the energy and direction of photons and  
 1607 neutral hadrons as well as differentiate these neutral particles from the charged hadron  
 1608 energy deposits. In cases involving charged hadrons for which the track parameters  
 1609 are not determined accurately, for instance low-quality and high-pT tracks, clustering  
 1610 helps in the energy measurements.

### 1611 **Electron track reconstruction.**

1612 Although the charged-particle track reconstruction described above works for elec-  
 1613 trons, they lose a significant fraction of their energy via bremsstrahlung photon radi-  
 1614 ation before reaching the ECAL; thus, the reconstruction performance depends on the  
 1615 ability to measure also the radiated energy. The reconstruction strategy in this case  
 1616 requires information from the tracking system and from the ECAL. Bremsstrahlung  
 1617 photons are emmited at similar  $\eta$  values to that of the electron but at different values  
 1618 of  $\phi$ ; therefore, the radiated energy can be recovered by grouping ECAL clusters in a  
 1619  $\eta$  window over a range of  $\phi$  around the electron direction. The group is called ECAL  
 1620 supercluster.

1621

1622 Electron candidates from the the track-seeding and ECAL superclustering are merged  
 1623 into a single collection which is submitted to a full electron tracking fit with a  
 1624 Gaussian-sum filter (GSF) [94]. The electron track and its associated ECAL su-  
 1625 percluster form a *particle-flow electron*.

### 1626 **Muon track reconstruction.**

1627 Given that the CMS detector is equipped with a muon detection system capable to  
 1628 identify and measure the momentum of the muons traversing it, the muon reconstruc-

tion is not specific to PF; therefore, three different muon types are defined  
 1629        $\text{\AA}$  standalone muon. Hits within each DT or CSC detector are clustered to form  
 1630       track segments, used as seeds for the pattern recognition in the muon spectrometer,  
 1631       to gather all DT, CSC, and RPC hits along the muon trajectory. The result of the  
 1632       final fitting is called a standalone-muon track.  $\text{\AA}$  global muon. Each standalone-  
 1633       muon track is matched to a track in the inner tracker (hereafter referred to as an  
 1634       inner track) if the parameters of the two tracks propagated onto a common surface  
 1635       are compatible. The hits from the inner track and from the standalone-muon track  
 1636       are combined and fit to form a global-muon track. At large transverse momenta,  $pT$   
 1637       & 200 GeV, the global-muon fit improves the momentum resolution with respect to  
 1638       the tracker-only fit.  $\text{\AA}$  tracker muon. Each inner track with  $pT$  larger than 0.5 GeV  
 1639       and a total momentum  $p$  in excess of 2.5 GeV is extrapolated to the muon system. If  
 1640       at least one muon segment matches the extrapolated track, the inner track qualifies  
 1641       as a tracker muon track. The track-to-segment matching is performed in a local ( $x$ ,  
 1642        $y$ ) coordinate system defined in a plane transverse to  
 1643       the beam axis, where  $x$  is the better measured coordinate. The extrapolated  
 1644       track and the segment are matched either if the absolute value of the difference  
 1645       between their positions in the  $x$  coordinate is smaller than 3 cm, or if the ratio of  
 1646       this distance to its uncertainty (pull) is smaller than 4. Global-muon reconstruction  
 1647       is designed to have high efficiency for muons penetrating through more than one  
 1648       muon detector plane. It typically requires segments to be associated in at least two  
 1649       muon detector planes. For momenta below about 10 GeV, this requirement fails  
 1650       more often because of the larger multiple scattering in the steel of the return yoke.  
 1651       For these muons, the tracker muon reconstruction is therefore more efficient, as it  
 1652       requires only one segment in the muon system [35]. Owing to the high efficiency of  
 1653       the inner track and muon segment reconstruction, about 99of the muons produced  
 1654       in the collision are reconstructed.

1655 within the geometrical acceptance of the muon system are reconstructed either as a  
1656 global muon or a tracker muon and very often as both. Global muons and tracker  
1657 muons that share the same inner track are merged into a single candidate. Muons  
1658 reconstructed only as standalone-muon tracks have worse momentum resolution and  
1659 a higher admixture of cosmic muons than global and tracker muons. Charged hadrons  
1660 may be misreconstructed as muons e.g. if some of the hadron shower remnants reach  
1661 the muon system (punch-through). Different identification criteria can be applied  
1662 to the muon tracks in order to obtain the desired balance between identification  
1663 efficiency and purity. In the PF muon identification algorithm (section 4.2), muon  
1664 energy deposits in ECAL, HCAL, and HO are associated with the muon track and  
1665 this information is used to improve the muon identification performance.  
  
1666 Once individual particles are identified and reconstructed, they can be grouped into  
1667 larger objects to form jets. The reconstruction of all the particles in an event is used  
1668 to determine the presence of neutrinos represented by an imbalance in the transverse  
1669 energy.

1670 Single particles give rise to different elements in the detector, thus a linking of  
1671 these elements is required in order to reconstruct a particle correctly. The linker al-  
1672 gorithm links two elements together on a trial basis and only keeps elements linked,  
1673 if their quality surpasses a certain threshold. The linker tries to extrapolate tracks  
1674 starting from the outermost hit in the silicon detector to either, the first two PS layers,  
1675 the ECAL in depth of a typical maximum of an electromagnetic shower or the HCAL  
1676 at a depth of a typical hadron shower length. If the extrapolated track is in corre-  
1677 spondence up to a certain link distance with a calorimeter cluster the two elements  
1678 are linked together. When linking tracks to ECAL clusters the trajectory of the track  
1679 is extrapolated along its tangent, looking for energy deposits by bremsstrahlung. El-  
1680 ements directly or indirectly linked with each other are known as blocks. The high

1681 granularity of the CMS detector causes most blocks to only contain one to three ele-  
1682 ments and therefore the object reconstruction is simplified. The linking algorithm, as  
1683 well as the whole particle flow algorithm, was intensively validated and commissioned  
1684 [96] as e. g. a broken link could lead to a reconstruction of a ghost particle and  
1685 thus to an overestimation of the total energy of the collision. In the last reconstruc-  
1686 tion step, the found blocks in the detector are interpreted as candidates, as they are  
1687 reconstructed as actual physical objects.

1688 CMS requires an offline first-pass full reconstruction of express line and all online  
1689 streams in quasi-realtime, which produces new reconstructed objects called RECO  
1690 data.

1691 vertexing , jets reco, anti-kt algorithm, jet energy corrections, btagging, MET

1692 The Tier-0 offline reconstruction step processes all RAW events from the online  
1693 system following an adjustable set of priorities (the express-line, by definition has  
1694 very high priority). This step creates new higher-level physics objects such as tracks,  
1695 vertices, and jets. These may improve or extend the set produced in the HLT pro-  
1696 cessing step. It must run with minimal delay compared to the online in order to  
1697 provide rapid feedback to the online operations, for example, identifying detector or  
1698 trigger problems which can then be rectified dynamically during the same LHC fill.

1699 The offline reconstruction will normally perform the same reconstruction steps for  
1700 each stream, with the possible exception of specialised calibration streams. In this  
1701 way we ensure that they are all useful in principle for all analysis groups. We apply  
1702 this same rule to later re-processings of the data, 2-3 times per year we expect to  
1703 bring all datasets into consistent status as to applied calibrations and algorithms, as  
1704 described below.

1705 **4.5 MVA methods, NN, BDT, boosting,**

1706 **overtraining, variable ranking**

1707 **4.6 statistical inference, likelihood**

1708 **parametrization**

1709 **4.7 nuisance parameters**

1710 **4.8 exclusion limits**

1711 **4.9 asymptotic limits**

<sup>1712</sup> **Chapter 5**

<sup>1713</sup> **Search for production of a Higgs**

<sup>1714</sup> **boson and a single top quark in**

<sup>1715</sup> **multilepton final states in pp**

<sup>1716</sup> **collisions at  $\sqrt{s} = 13$  TeV**

<sup>1717</sup> **5.1 Introduction**

<sup>1718</sup> Dont forget to mention previous constrains to ct check reference ?? and references

<sup>1719</sup> <https://link.springer.com/content/pdf/10.1007%2FJHEP01>

<sup>1720</sup> A. Azatov, R. Contino and J. Galloway, âIModel-Independent Bounds on a

<sup>1721</sup> Light Higgs,âI JHEP 1204 (2012) 127 [arXiv:1202.3415 [hep-ph]].

<sup>1722</sup> J. R. Espinosa, C. Grojean, M. Muhlleitner and M. Trott, âIJFingerprinting

<sup>1723</sup> Higgs Suspects at the LHC,âI JHEP 1205 (2012) 097 [arXiv:1202.3697 [hep-ph]].

<sup>1724</sup> This chapter present the search for the associated production of a Higgs boson and

<sup>1725</sup> a single top quark events with three leptons in the final state, targeting Higgs decay

1726 modes to  $WW$ ,  $ZZ$ , and  $\tau\tau$ . The analysis uses the 13 TeV dataset produced in 2016,  
 1727 corresponding to an integrated luminosity of  $35.9\text{fb}^{-1}$ . It is based on and expands  
 1728 previous analyses at 8 TeV [95, 96] and searches for associated production of  $t\bar{t}$  and  
 1729 Higgs in the same channel [97], and complements searches in other decay channels  
 1730 targeting  $H \rightarrow b\bar{b}$  [98].

1731 As showed in section 2.4, the cross section of the associated production of a Higgs  
 1732 boson and a single top quark ( $tHq$ ) process is driven by a destructive interference of  
 1733 two contributions (see Figure 5.1), where the Higgs couples to either the W boson or  
 1734 the top quark. Any deviation from the standard model (SM) in the Higgs coupling  
 1735 structure could therefore lead to a large enhancement of the cross section, making  
 1736 this analysis sensitive to such deviations. A second process, where the Higgs and  
 1737 top quark are accompanied by a W boson ( $tHW$ ) has similar behavior, albeit with a  
 1738 weaker interference pattern.

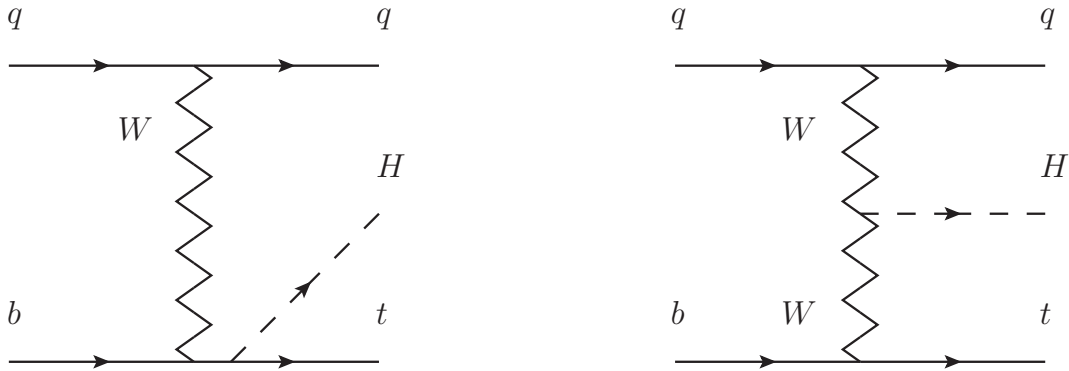


**Figure 5.1:** The two leading-order diagrams of  $tHq$  production.

1739 We selects events with three leptons and a  $b$  tagged jet in the final state. The  $tHq$   
 1740 signal contribution is then determined in a fit of the observed data to two multivariate  
 1741 classifier outputs, each trained to discriminate against one of the two dominant back-  
 1742 grounds of events with non-prompt leptons from  $t\bar{t}$  and of associated production of  $t\bar{t}$

1743 and vector bosons ( $t\bar{t}W$ ,  $t\bar{t}Z$ ). The fit result is then used to set an upper limit on the  
 1744 combined  $t\bar{t}H$ ,  $tHq$  and  $tHW$  production cross section, as a function of the relative  
 1745 coupling strengths of Higgs and top quark and Higgs and W boson, respectively.

## 1746 5.2 Data and MC Samples

1747 The data considered in this analysis were collected by the CMS experiment dur-  
 1748 ing 2016 and correspond to a total integrated luminosity of  $35.9\text{fb}^{-1}$ . Only periods  
 1749 when the CMS magnet was on were considered when selecting the data samples, that  
 1750 corresponds to the 23 Sep 2016 (Run B to G) and PromptReco (Run H) versions  
 1751 of the datasets. The MC samples used in this analysis correspond to the RunI-  
 1752 ISummer16MiniAODv2 campaign produced with CMSSW 80X. The two signal sam-  
 1753 ples (for  $tHq$  and  $tHW$ ) were produced with MG5\_aMC@NLO (version 5.222), in  
 1754 leading-order mode, and are normalized to next-to-leading-order cross sections,  
 1755 see Tab. 5.1. Each sample is generated with a set of event weights corresponding to  
 1756 different values of  $\kappa_t$  and  $\kappa_V$  couplings as shown in Tab. 5.2.

### 1757 5.2.1 Full 2016 dataset and MC samples

Sample	$\sigma$ [pb]	BF
/THQ_Hincl_13TeV-madgraph-pythia8_TuneCUETP8M1/	0.7927	0.324
/THW_Hincl_13TeV-madgraph-pythia8_TuneCUETP8M1/	0.1472	1.0

**Table 5.1:** Signal samples and their cross section and branching fraction used in this analysis. See Ref. [99] for more details.

1758 Different MC generators were used to generate the background processes. The  
 1759 dominant sources ( $t\bar{t}$ ,  $t\bar{t}W$ ,  $t\bar{t}Z$ ,  $t\bar{t}H$ ) were produced using AMC@NLO interfaced  
 1760 to PYTHIA8, and are scaled to NLO cross sections. Other processes are simulated

		<i>tHq</i>		<i>tHW</i>		
$\kappa_V$	$\kappa_t$	sum of weights	cross section [pb]	sum of weights	cross section [pb]	LHE weights
1.0	-3.0	35.700022	2.991	11.030445	0.6409	LHEweight_wgt[446]
1.0	-2.0	20.124298	1.706	5.967205	0.3458	LHEweight_wgt[447]
1.0	-1.5	14.043198	1.205	4.029093	0.2353	LHEweight_wgt[448]
1.0	-1.25	11.429338	0.9869	3.208415	0.1876	LHEweight_wgt[449]
1.0	-1.0		0.7927		0.1472	
1.0	-0.75	7.054998	0.6212	1.863811	0.1102	LHEweight_wgt[450]
1.0	-0.5	5.294518	0.4723	1.339886	0.07979	LHEweight_wgt[451]
1.0	-0.25	3.818499	0.3505	0.914880	0.05518	LHEweight_wgt[452]
1.0	0.0	2.627360	0.2482	0.588902	0.03881	LHEweight_wgt[453]
1.0	0.25	1.719841	0.1694	0.361621	0.02226	LHEweight_wgt[454]
1.0	0.5	1.097202	0.1133	0.233368	0.01444	LHEweight_wgt[455]
1.0	0.75	0.759024	0.08059	0.204034	0.01222	LHEweight_wgt[456]
1.0	1.0	0.705305	0.07096	0.273617	0.01561	LHEweight_wgt[457]
1.0	1.25	0.936047	0.0839	0.442119	0.02481	LHEweight_wgt[458]
1.0	1.5	1.451249	0.1199	0.709538	0.03935	LHEweight_wgt[459]
1.0	2.0	3.335034	0.2602	1.541132	0.08605	LHEweight_wgt[460]
1.0	3.0	10.516125	0.8210	4.391335	0.2465	LHEweight_wgt[461]
1.5	-3.0	45.281492	3.845	13.426212	0.7825	LHEweight_wgt[462]
1.5	-2.0	27.606715	2.371	7.809713	0.4574	LHEweight_wgt[463]
1.5	-1.5	20.476088	1.784	5.594971	0.3290	LHEweight_wgt[464]
1.5	-1.25	17.337465	1.518	4.635978	0.2749	LHEweight_wgt[465]
1.5	-1.0	14.483302	1.287	3.775902	0.2244	LHEweight_wgt[466]
1.5	-0.75	11.913599	1.067	3.014744	0.1799	LHEweight_wgt[467]
1.5	-0.5	9.628357	0.874	2.352505	0.1410	LHEweight_wgt[468]
1.5	-0.25	7.627574	0.702	1.789184	0.1081	LHEweight_wgt[469]
1.5	0.0	5.911882	0.5577	1.324946	0.08056	LHEweight_wgt[470]
1.5	0.25	4.479390	0.4365	0.959295	0.05893	LHEweight_wgt[471]
1.5	0.5	3.331988	0.3343	0.692727	0.04277	LHEweight_wgt[472]
1.5	0.75	2.469046	0.2558	0.525078	0.03263	LHEweight_wgt[473]
1.5	1.0	1.890565	0.2003	0.456347	0.02768	LHEweight_wgt[474]
1.5	1.25	1.596544	0.1689	0.486534	0.02864	LHEweight_wgt[475]
1.5	1.5	1.586983	0.1594	0.615638	0.03509	LHEweight_wgt[476]
1.5	2.0	2.421241	0.2105	1.170602	0.06515	LHEweight_wgt[477]
1.5	3.0	7.503280	0.5889	3.467546	0.1930	LHEweight_wgt[478]
0.5	-3.0	27.432685	2.260	8.929074	0.5136	LHEweight_wgt[479]
0.5	-2.0	13.956013	1.160	4.419093	0.2547	LHEweight_wgt[480]
0.5	-1.5	8.924438	0.7478	2.757611	0.1591	LHEweight_wgt[481]
0.5	-1.25	6.835341	0.5726	2.075247	0.1204	LHEweight_wgt[482]
0.5	-1.0	5.030704	0.4273	1.491801	0.08696	LHEweight_wgt[483]
0.5	-0.75	3.510528	0.2999	1.007273	0.05885	LHEweight_wgt[484]
0.5	-0.5	2.274811	0.1982	0.621663	0.03658	LHEweight_wgt[485]
0.5	-0.25	1.323555	0.1189	0.334972	0.01996	LHEweight_wgt[486]
0.5	0.0	0.656969	0.06223	0.147253	0.008986	LHEweight_wgt[487]
0.5	0.25	0.274423	0.02830	0.058342	0.003608	LHEweight_wgt[488]
0.5	0.5	0.176548	0.01778	0.068404	0.003902	LHEweight_wgt[489]
0.5	0.75	0.363132	0.03008	0.177385	0.009854	LHEweight_wgt[490]
0.5	1.0	0.834177	0.06550	0.385283	0.02145	LHEweight_wgt[491]
0.5	1.25	1.589682	0.1241	0.692099	0.03848	LHEweight_wgt[492]
0.5	1.5	2.629647	0.2047	1.097834	0.06136	LHEweight_wgt[493]
0.5	2.0	5.562958	0.4358	2.206057	0.1246	LHEweight_wgt[494]
0.5	3.0	14.843102	1.177	5.609519	0.3172	LHEweight_wgt[495]

**Table 5.2:**  $\kappa_V$  and  $\kappa_t$  combinations generated for the two signal samples and their NLO cross sections. The *tHq* cross section is multiplied by the branching fraction of the enforced leptonic decay of the top quark (0.324). See also Ref. [99].

Sample	$\sigma$ [pb]
TTWJetsToLNu_TuneCUETP8M1_13TeV-amcatnloFXFX-madspin-pythia8	0.2043
TTZToLLNuNu_M-10_TuneCUETP8M1_13TeV-amcatnlo-pythia8	0.2529
tthJetToNonbb_M125_13TeV_amcatnloFXFX_madspin_pythia8_mWCutfix /store/cmst3/group/susy/gpetrucc/13TeV/u/TTLL_m1to10_L0_NoMS_for76X/	0.2151 0.0283
WGToLNuG_TuneCUETP8M1_13TeV-madgraphMLM-pythia8	585.8
ZGTo2LG_TuneCUETP8M1_13TeV-amcatnloFXFX-pythia8	131.3
TGJets_TuneCUETP8M1_13TeV_amcatnlo_madspin_pythia8	2.967
TGJets_TuneCUETP8M1_13TeV_amcatnlo_madspin_pythia8	2.967
TTGJets_TuneCUETP8M1_13TeV-amcatnloFXFX-madspin-pythia8	3.697
WpWpJJ_EWK_QCD_TuneCUETP8M1_13TeV-madgraph-pythia8	0.03711
ZZZ_TuneCUETP8M1_13TeV-amcatnlo-pythia8	0.01398
WWZ_TuneCUETP8M1_13TeV-amcatnlo-pythia8	0.1651
WZZ_TuneCUETP8M1_13TeV-amcatnlo-pythia8	0.05565
WW_DoubleScattering_13TeV-pythia8	1.64
tZq_ll_4f_13TeV-amcatnlo-pythia8_TuneCUETP8M1	0.0758
ST_tWll_5f_LO_13TeV-MadGraph-pythia8	0.01123
TTTT_TuneCUETP8M1_13TeV-amcatnlo-pythia8	0.009103
WZTo3LNu_TuneCUETP8M1_13TeV-powheg-pythia8	4.4296
ZZTo4L_13TeV_powheg_pythia8	1.256
TTJets_SingleLeptFromTbar_TuneCUETP8M1_13TeV-madgraphMLM-pythia8	182.1754
TTJets_SingleLeptFromT_TuneCUETP8M1_13TeV-madgraphMLM-pythia8	182.1754
TTJets_DiLept_TuneCUETP8M1_13TeV-madgraphMLM-pythia8	87.3
DYJetsToLL_M-10to50_TuneCUETP8M1_13TeV-amcatnloFXFX-pythia8	18610
DYJetsToLL_M-50_TuneCUETP8M1_13TeV-madgraphMLM-pythia8	6024
WJetsToLNu_TuneCUETP8M1_13TeV-amcatnloFXFX-pythia8	61526.7
ST_tW_top_5f_inclusiveDecays_13TeV-powheg-pythia8_TuneCUETP8M1	35.6
ST_tW_antitop_5f_inclusiveDecays_13TeV-powheg-pythia8_TuneCUETP8M1	35.6
ST_t-channel_4f_leptonDecays_13TeV-amcatnlo-pythia8_TuneCUETP8M1	70.3144
ST_t-channel_antitop_4f_leptonDecays_13TeV-powheg-pythia8_TuneCUETP8M1	26.2278
ST_s-channel_4f_leptonDecays_13TeV-amcatnlo-pythia8_TuneCUETP8M1	3.68064
WWTo2L2Nu_13TeV-powheg	10.481

**Table 5.3:** List of background samples used in this analysis (CMSSW 80X). In the first section of the table are listed the samples of the processes for which we use the simulation to extract the final yields and shapes, in the second section the samples of the processes we will estimate from data. The MC simulation is used to design the data driven methods and derive the associated systematics.

Sample	$\sigma$ [pb]
ttWJets_13TeV_madgraphMLM	0.6105
ttZJets_13TeV_madgraphMLM	0.5297/0.692

**Table 5.4:** Leading-order  $t\bar{t}W$  and  $t\bar{t}Z$  samples used in the signal BDT training.

1761 using POWHEG interfaced to PYTHIA, or bare PYTHIA (see table 5.3 and [97]  
1762 for more details).

Three lepton and Four lepton
HLT_DiMu9_Ele9_CaloIdL_TrackIdL_v*
HLT_Mu8_DiEle12_CaloIdL_TrackIdL_v*
HLT_TripleMu_12_10_5_v*
HLT_Ele16_Ele12_Ele8_CaloIdL_TrackIdL_v*
HLT_Mu23_TrkIsoVVL_Ele8_CaloIdL_TrackIdL_IsoVL_v*
HLT_Mu23_TrkIsoVVL_Ele8_CaloIdL_TrackIdL_IsoVL_DZ_v*
HLT_Mu8_TrkIsoVVL_Ele23_CaloIdL_TrackIdL_IsoVL_v*
HLT_Mu8_TrkIsoVVL_Ele23_CaloIdL_TrackIdL_IsoVL_DZ_v*
HLT_Ele23_Ele12_CaloIdL_TrackIdL_IsoVL_DZ_v*
HLT_Mu17_TrkIsoVVL_Mu8_TrkIsoVVL_DZ_v*
HLT_Mu17_TrkIsoVVL_TkMu8_TrkIsoVVL_DZ_v*
HLT_IsoMu22_v*
HLT_IsoTkMu22_v*
HLT_IsoMu22_eta2p1_v*
HLT_IsoTkMu22_eta2p1_v*
HLT_IsoMu24_v*
HLT_IsoTkMu24_v*
HLT_Ele27_WPTight_Gsf_v*
HLT_Ele25_eta2p1_WPTight_Gsf_v*
HLT_Ele27_eta2p1_WPLoose_Gsf_v*

**Table 5.5:** Table of high-level triggers that we consider in the analysis.

### 1763 5.2.2 Triggers

1764 We consider online-reconstructed events triggered by one, two, or three leptons.  
 1765 Single-lepton triggers are included to boost the acceptance of events where the  $p_T$  of  
 1766 the sub-leading lepton falls below the threshold of the double-lepton triggers. Ad-  
 1767 ditionally, by including double-lepton triggers in the  $\geq 3$  lepton category, as well  
 1768 as single-lepton triggers in all categories, we increase the efficiency, considering the  
 1769 logical “or” of the trigger decisions of all the individual triggers in a given category.  
 1770 Tab. 5.5 shows the lowest-threshold non-prescaled triggers present in the High-Level  
 1771 Trigger (HLT) menus for both Monte-Carlo and data in 2016.

#### 1772 5.2.2.1 Trigger efficiency scale factors

1773 The efficiency of events to pass the trigger is measured in simulation (trivially using  
 1774 generator information) and in the data (using event collected by an uncorrelated

Category	Scale Factor
ee	$1.01 \pm 0.02$
e $\mu$	$1.01 \pm 0.01$
$\mu\mu$	$1.00 \pm 0.01$
3l	$1.00 \pm 0.03$

**Table 5.6:** Trigger efficiency scale factors and associated uncertainties, shown here rounded to the nearest percent.

1775 MET trigger). Small differences between the data and MC efficiencies are corrected  
 1776 by applying scale factors as shown in Tab. 5.6. The exact procedure and control plots  
 1777 are documented in [100] for the current analysis.

## 1778 5.3 Object Identification and event selection

### 1779 5.3.1 Jets and $b$ tagging

1780 The analysis uses anti- $k_t$  (0.4) particle-flow (PF) jets, corrected for charged hadrons  
 1781 not coming from the primary vertex (charged hadron subtraction), and having jet  
 1782 energy corrections (`Summer16_23Sep2016V3`) applied as a function of the jet  $E_T$  and  
 1783  $\eta$ . Jets are only considered if they have a transverse energy above 25GeV.

1784 In addition, they are required to be separated from any lepton candidates passing  
 1785 the fakeable object selections (see Tables 5.7 and 5.8) by  $\Delta R > 0.4$ .

1786 The loose and medium working points of the CSV b-tagging algorithm are used to  
 1787 identify  $b$  jets. Data/simulation differences in the  $b$  tagging performance are corrected  
 1788 by applying per-jet weights to the simulation, dependent on the jet  $p_T$ , eta,  $b$  tagging  
 1789 discriminator, and flavor (from simulation truth) [101]. The per-event weight is taken  
 1790 as the product of the per-jet weights, including those of the jets associated to the  
 1791 leptons. More details can be found in the corresponding  $t\bar{t}H$  documentation [97, 100].

1792 **5.3.2 Lepton selection**

Cut	Loose	Fakeable object	Tight
$ \eta  < 2.4$	✓	✓	✓
$p_T$	$> 5\text{GeV}$	$> 15\text{GeV}$	$> 15\text{GeV}$
$ d_{xy}  < 0.05 \text{ (cm)}$	✓	✓	✓
$ d_z  < 0.1 \text{ (cm)}$	✓	✓	✓
$\text{SIP}_{3D} < 8$	✓	✓	✓
$I_{\text{mini}} < 0.4$	✓	✓	✓
is Loose Muon	✓	✓	✓
jet CSV	—	$< 0.8484$	$< 0.8484$
is Medium Muon	—	—	✓
tight-charge	—	—	✓
lepMVA $> 0.90$	—	—	✓

**Table 5.7:** Requirements on each of the three muon selections. In the cases where the cut values change between the selections, those values are listed in the table. Otherwise, whether the cut is applied is indicated. For the two  $p_T^{\text{ratio}}$  and CSV rows, the cuts marked with a † are applied to leptons that fail the lepton MVA cut, while the loose cut value is applied to those that pass the lepton MVA cut.

1793 The lepton reconstruction and selection is identical to that used in the  $t\bar{t}H$  mul-  
 1794 tilepton analysis, as documented in Refs. [97, 100]. For details on the reconstruction  
 1795 algorithms, isolation, pileup mitigation, and a description of the lepton MVA discrim-  
 1796 inator and validation plots thereof, we refer to that document since they are out of  
 1797 the scope of this thesis. Three different selections are defined both for the electron  
 1798 and muon object identification: the *Loose*, *Fakeable Object*, and *Tight* selection. As  
 1799 described in more detail later, these are used for event level vetoes, the fake rate  
 1800 estimation application region, and the final signal selection, respectively. The  $p_T$  of  
 1801 fakeable objects is defined as  $0.85 \times p_T(\text{jet})$ , where the jet is the one associated to the  
 1802 lepton object. This mitigates the dependence of the fake rate on the momentum of  
 1803 the fakeable object and thereby improves the precision of the method.

1804 Tables 5.7 and 5.8 list the full criteria for the different selections of muons and  
 1805 electrons.

Cut	Loose	Fakeable Object	Tight
$ \eta  < 2.5$	✓	✓	✓
$p_T$	$> 7\text{GeV}$	$> 15\text{GeV}$	$> 15\text{GeV}$
$ d_{xy}  < 0.05 \text{ (cm)}$	✓	✓	✓
$ d_z  < 0.1 \text{ (cm)}$	✓	✓	✓
$\text{SIP}_{3D} < 8$	✓	✓	✓
$I_{\text{mini}} < 0.4$	✓	✓	✓
MVA ID $> (0.0, 0.0, 0.7)$	✓	✓	✓
$\sigma_{in\eta} < (0.011, 0.011, 0.030)$	—	✓	✓
$\text{H/E} < (0.10, 0.10, 0.07)$	—	✓	✓
$\Delta\eta_{in} < (0.01, 0.01, 0.008)$	—	✓	✓
$\Delta\phi_{in} < (0.04, 0.04, 0.07)$	—	✓	✓
$-0.05 < 1/E - 1/p < (0.010, 0.010, 0.005)$	—	✓	✓
$p_T^{\text{ratio}}$	—	$> 0.5^\dagger / -$	—
jet CSV	—	$< 0.3^\dagger / < 0.8484$	$< 0.8484$
tight-charge	—	—	✓
conversion rejection	—	—	✓
Number of missing hits	$< 2$	$== 0$	$== 0$
lepMVA $> 0.90$	—	—	✓

**Table 5.8:** Criteria for each of the three electron selections. In cases where the cut values change between selections, those values are listed in the table. Otherwise, whether the cut is applied is indicated. In some cases, the cut values change for different  $\eta$  ranges. These ranges are  $0 < |\eta| < 0.8$ ,  $0.8 < |\eta| < 1.479$ , and  $1.479 < |\eta| < 2.5$  and the respective cut values are given in the form (value<sub>1</sub>, value<sub>2</sub>, value<sub>3</sub>).

### 1806 5.3.3 Lepton selection efficiency

1807 Efficiencies of reconstruction and selecting loose leptons are measured both for muons  
 1808 and electrons using a tag and probe method on both data and MC, using  $Z \rightarrow \ell^+ \ell^-$ .  
 1809 Corresponding scale factors are derived from the ratio of efficiencies and applied to the  
 1810 selected These. Events are produced for the leptonic SUSY analyses using equivalent  
 1811 lepton selections and recycled for the  $t\bar{t}H$  analysis as well as for this analysis. The  
 1812 efficiencies of applying the tight selection as defined in Tables 5.7 and 5.8, on the  
 1813 loose leptons are determined again by using a tag and probe method on a sample of  
 1814 DY-enriched events. They are documented for the  $t\bar{t}H$  analysis in Ref. [100] and are  
 1815 exactly equivalent for this analysis.

## 1816 5.4 Background predictions

1817 The modeling of reducible and irreducible backgrounds in this analysis uses the exact  
1818 methods, analysis code, and ROOT trees used for the  $t\bar{t}H$  multilepton analysis. We  
1819 give a brief description of the methods and refer to the documentation of that analysis  
1820 in Refs. [97, 100] for any details.

1821 The backgrounds in three-lepton final states can be split in two broad categories:  
1822 irreducible backgrounds with genuine prompt leptons (i.e. from on-shell W and Z  
1823 boson decays); and reducible backgrounds where at least one of the leptons is “non-  
1824 prompt”, i.e. produced within a hadronic jet, either a genuine lepton from heavy  
1825 flavor decays, or simply mis-reconstructed jets.

1826 Irreducible backgrounds can be reliably estimated directly from Monte-Carlo sim-  
1827 ulated events, using higher-order cross sections or data control regions for the overall  
1828 normalization. This is done in this analysis for all backgrounds involving prompt lep-  
1829 tons:  $t\bar{t}W$ ,  $t\bar{t}Z$ ,  $t\bar{t}H$ ,  $WZ$ ,  $ZZ$ ,  $W^\pm W^\pm qq$ ,  $t\bar{t}t\bar{t}$ ,  $tZq$ ,  $tZW$ ,  $WWW$ ,  $WWZ$ ,  $WZZ$ ,  
1830  $ZZZ$ .

1831 Reducible backgrounds, on the other hand, are not well predicted by simulation,  
1832 and are estimated using data-driven methods. In the case of non-prompt leptons, a  
1833 fake rate method is used, where the contribution to the final selection is estimated by  
1834 extrapolating from a sideband (or “application region”) with a looser lepton definition  
1835 (the fakeable object definitions in Tabs. 5.7 and 5.8) to the signal selection. The tight-  
1836 to-loose ratios (or “fake rates”) are measured in several background dominated data  
1837 events with dedicated triggers, subtracting the residual prompt lepton contribution  
1838 using MC. Non-prompt leptons in our signal regions are predominantly produced in  $t\bar{t}$   
1839 events, with a much smaller contribution, from Drell–Yan production. The systematic  
1840 uncertainty on the normalization of the non-prompt background estimation is on the

1841 order of 50%, and thereby one of the dominant limitations on the performance of  
 1842 multilepton analyses in general and this analysis in particular. It consists of several  
 1843 individual sources, such as the result of closure tests of the method using simulated  
 1844 events, limited statistics in the data control regions due to necessary prescaling of  
 1845 lepton triggers, and the uncertainty in the subtraction of residual prompt leptons  
 1846 from the control region.

1847 The fake background where the leptons pass the looser selection are weighted  
 1848 according to how many of them fail the tight criteria. Events with a single failing  
 1849 lepton are weighted with the factor  $f/(1-f)$  for the estimate to the tight selection  
 1850 region, where  $f$  is the fake rate. Events with two failing leptons are given the negative  
 1851 weight  $-f_i f_j / (1 - f_i)(1 - f_j)$ , and for three leptons the weight is positive and equal  
 1852 to the product of  $f/(1-f)$  factor evaluated for each failing lepton.

1853 Figures 5.2 show the distributions of some relevant kinematic variables, normalized  
 1854 to the cross section of the respective processes and to the integrated luminosity.

## 1855 5.5 Signal discrimination

1856 The  $tHq$  signal is separated from the main backgrounds using a boosted decision  
 1857 tree (BDT) classifier, trained on simulated signal and background events. A set of  
 1858 discriminating variables are given as input to the BDT which produces a output  
 1859 distribution maximizing the discrimination power. Table 5.9 lists the input variables  
 1860 used while Figures 5.3 show their distributions for the relevant signal and background  
 1861 samples, for the three lepton channel. Two BDT classifiers are trained for the two  
 1862 main backgrounds expected in the analysis: events with prompt leptons from  $t\bar{t}W$  and  
 1863  $t\bar{t}Z$  (also referred to as  $t\bar{t}V$ ), and events with non-prompt leptons from  $t\bar{t}$ . The datasets  
 1864 used in the training are the  $tHq$  signal (see Tab. 5.1), and LO MADGRAPH samples

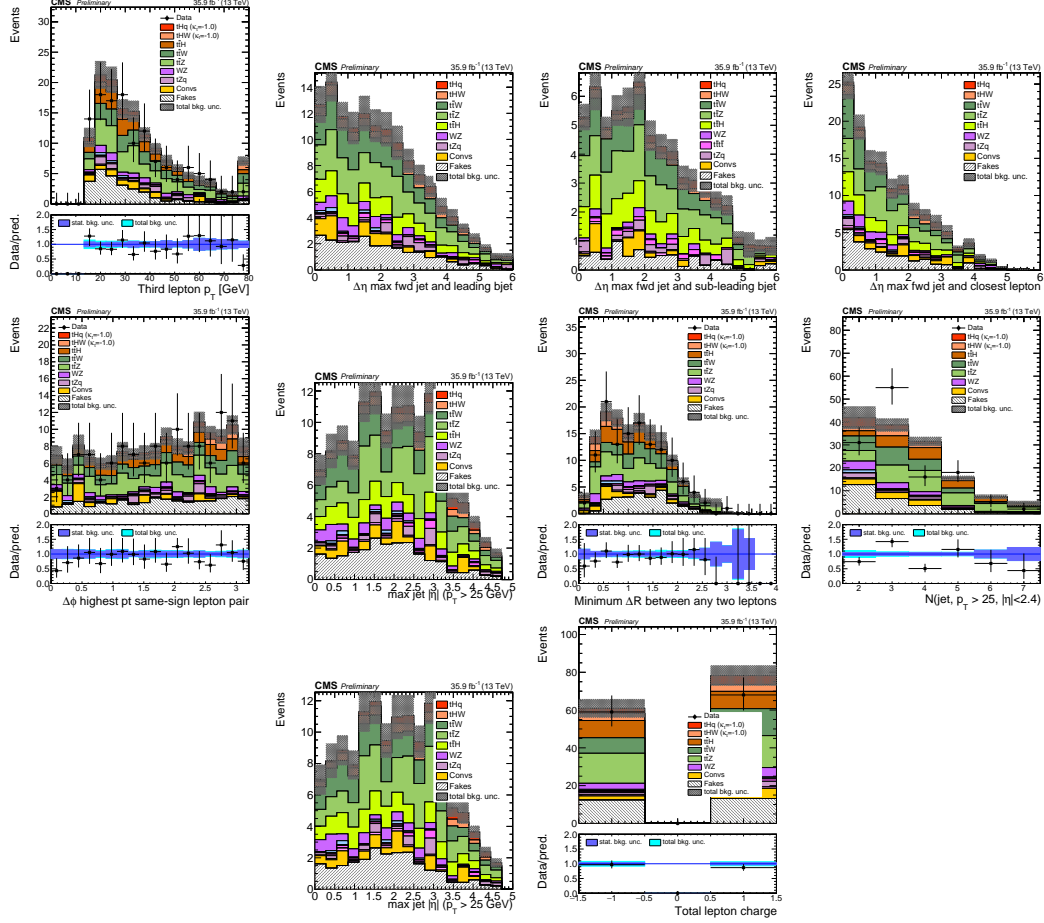


**Figure 5.2:** Distributions of input variables to the BDT for signal discrimination, three lepton channel, normalized to their cross section and to  $35.9\text{fb}^{-1}$ .

of  $t\bar{t}W$  and  $t\bar{t}Z$ , in an admixture proportional to their respective cross sections (see Tab. 5.4).

The MVA analysis consist of two stages: first a “training” where the MVA method is trained to discriminate between simulated signal and background events, then a “test” stage where the trained algorithm is used to classify different events from the samples. The sample is obtained from a pre-selection (see Tab. ?? with pre-selection cuts). Figures 5.4 show the input variables distributions as seen by the MVA algorithm. Note that in contrast to the distributions in Fig. 5.3 only the main backgrounds ( $t\bar{t}$  from simulation,  $t\bar{t}V$ ) are included.

Variable name	Description
nJet25	Number of jets with $p_T > 25$ GeV, $ \eta  < 2.4$
MaxEtaJet25	Maximum $ \eta $ of any (non-CSV-loose) jet with $p_T > 25$ GeV
totCharge	Sum of lepton charges
nJetEta1	Number of jets with $ \eta  > 1.0$ , non-CSV-loose
detaFwdJetBJet	$\Delta\eta$ between forward light jet and hardest CSV loose jet
detaFwdJet2BJet	$\Delta\eta$ between forward light jet and second hardest CSV loose jet (defaults to -1 in events with only one CSV loose jet)
detaFwdJetClosestLep	$\Delta\eta$ between forward light jet and closest lepton
dphiHighestPtSSPair	$\Delta\phi$ of highest $p_T$ same-sign lepton pair
minDRll	minimum $\Delta R$ between any two leptons
Lep3Pt/Lep2Pt	$p_T$ of the 3 <sup>rd</sup> lepton (2 <sup>nd</sup> for ss2l)

**Table 5.9:** MVA input discriminating variables

1874 Note that splitting the training in two groups reveals that some variables show  
 1875 opposite behavior for the two background sources; potentially screening the discrimi-  
 1876 nation power if they were to be used in a single discriminant. For some other variables  
 1877 the distributions are similar in both background cases.

1878 From table 5.9, it is clear that the input variables are correlated to some extend.  
 1879 These correlations play an important role for some MVA methods like the Fisher  
 1880 discriminant method in which the first step consist of performing a linear transfor-  
 1881 mation to an phase space where the correlations between variables are removed. In  
 1882 case a boosted decision tree (BDT) method however, correlations do not affect the  
 1883 performance. Figure 5.6 show the linear correlation coefficients for signal and back-  
 1884 ground for the two training cases (the signal values are identical by construction). As  
 1885 expected, strong correlations appears for variables related to the forward jet activity.  
 1886 Same trend is seen in case of the same sign dilepton channel in Figure ??.

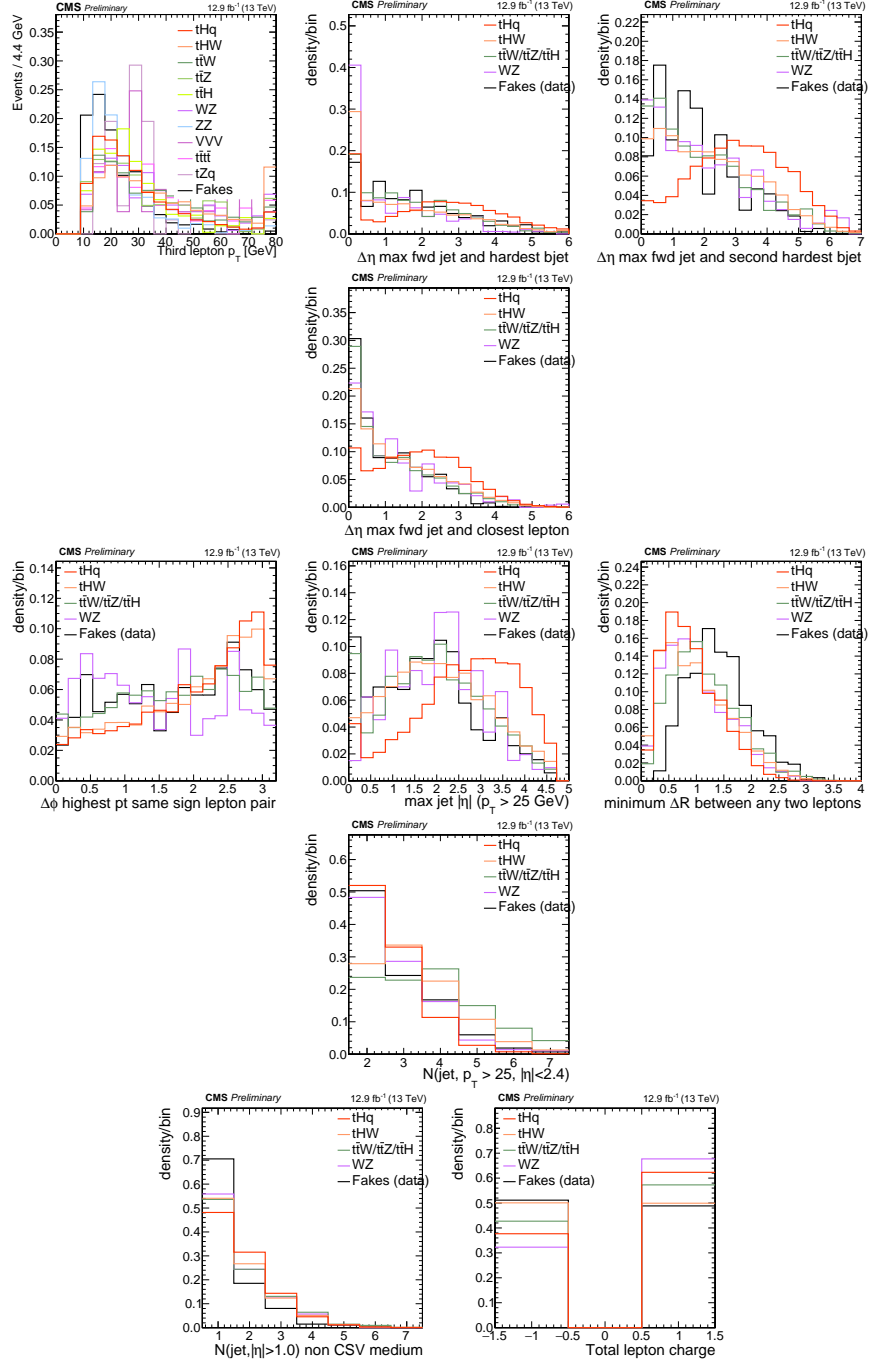


**Figure 5.3:** Distributions of input variables to the BDT for signal discrimination, three lepton channel.

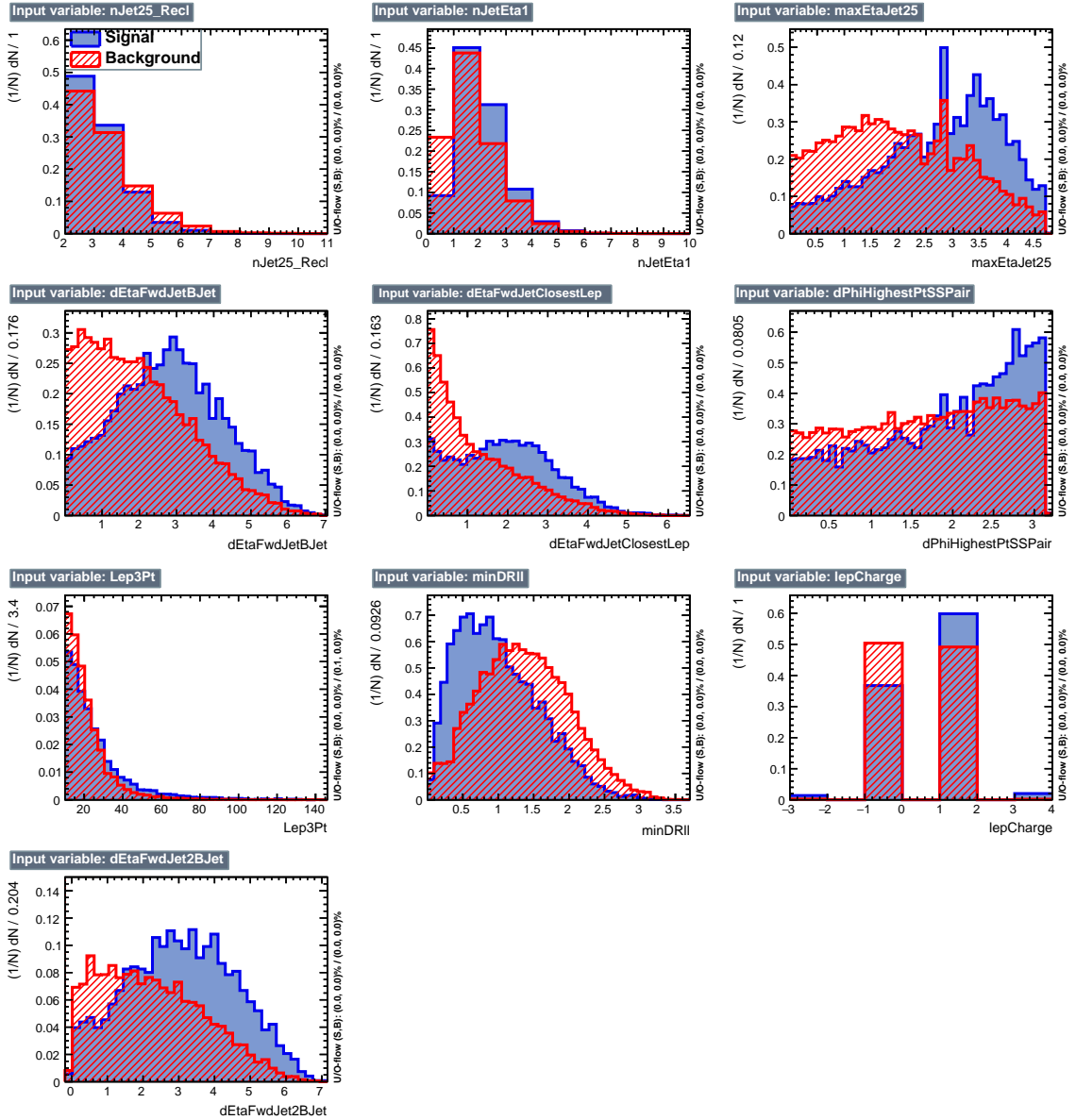


**Figure 5.4:** BDT inputs as seen by TMVA (signal, in blue, is  $tHq$ , background, in red, is  $t\bar{t}$ ) for the three lepton channel, discriminated against  $t\bar{t}$  (fakes) background.

### 1887 5.5.1 Classifiers response

1888 Several MVA algorithms were evaluated to determine the most appropriate method  
 1889 for this analysis. The plots in Fig. 5.7 (top) show the background rejection as a  
 1890 function of the signal efficiency for  $t\bar{t}$  and  $t\bar{t}V$  trainings (ROC curves) for the different

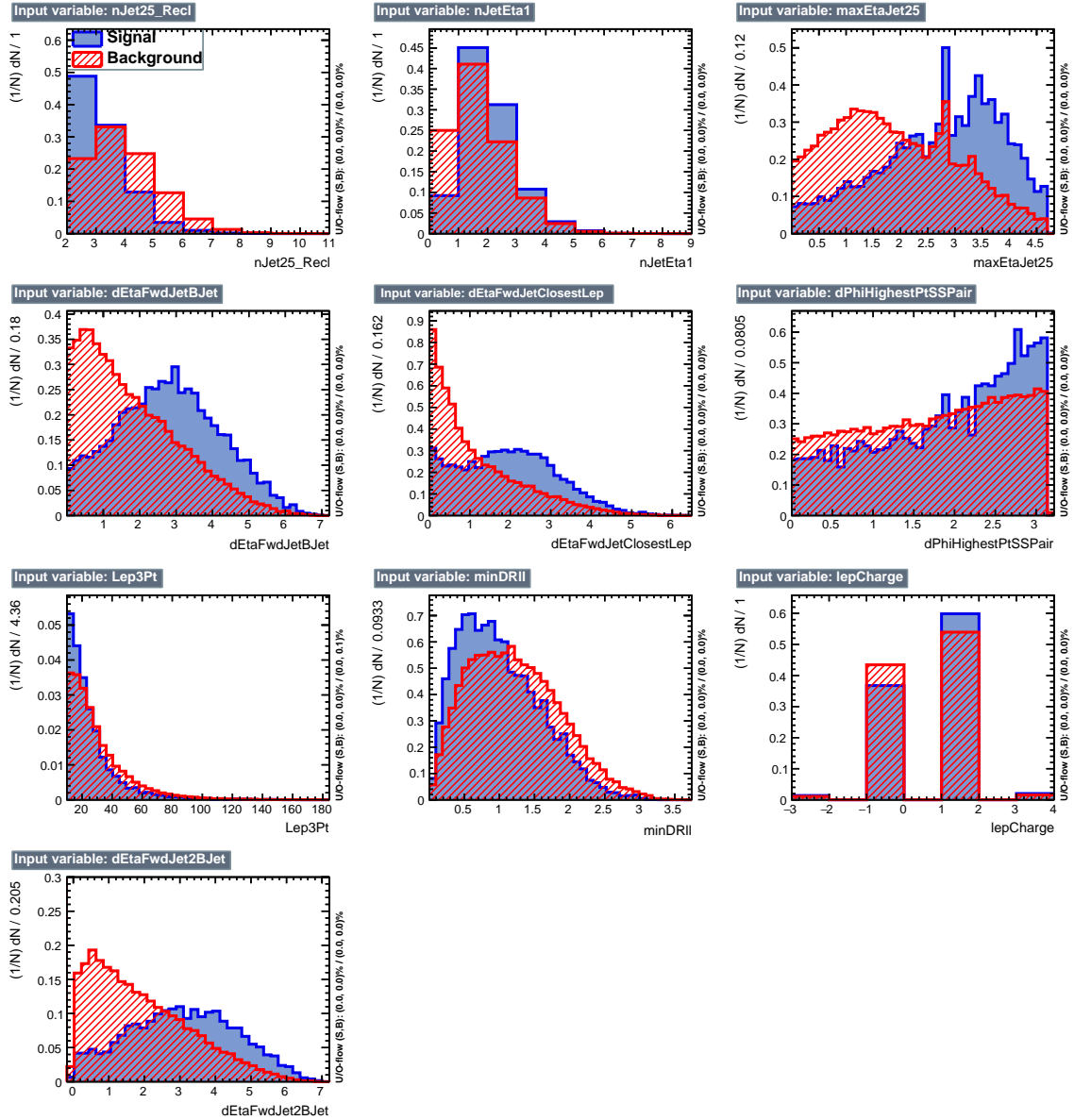


**Figure 5.5:** BDT inputs as seen by TMVA (signal, in blue, is  $tHq$ , background, in red, is  $t\bar{t}W+t\bar{t}Z$ ) for the three lepton channel, discriminated against  $t\bar{t}V$  background.

1891 algorithms that were evaluated.

1892 In both cases the gradient boosted decision tree (“BDTA\_GRAD”) classifier offers  
 1893 the best results, followed by an adaptive BDT classifier (“BDTA”). The BDTA\_GRAD  
 1894 classifier output distributions for signal and backgrounds are shown on the bottom of  
 1895 Fig. 5.7. As expected, a good discrimination power is obtained using default discrim-

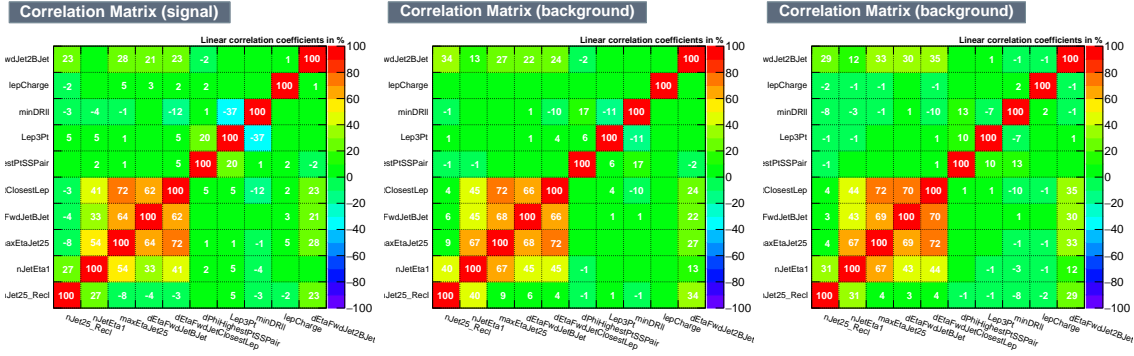


**Figure 5.6:** Signal (left),  $t\bar{t}$  background (middle), and  $t\bar{t}V$  background (right.) correlation matrices for the input variables in the TMVA analysis for the three lepton channel.

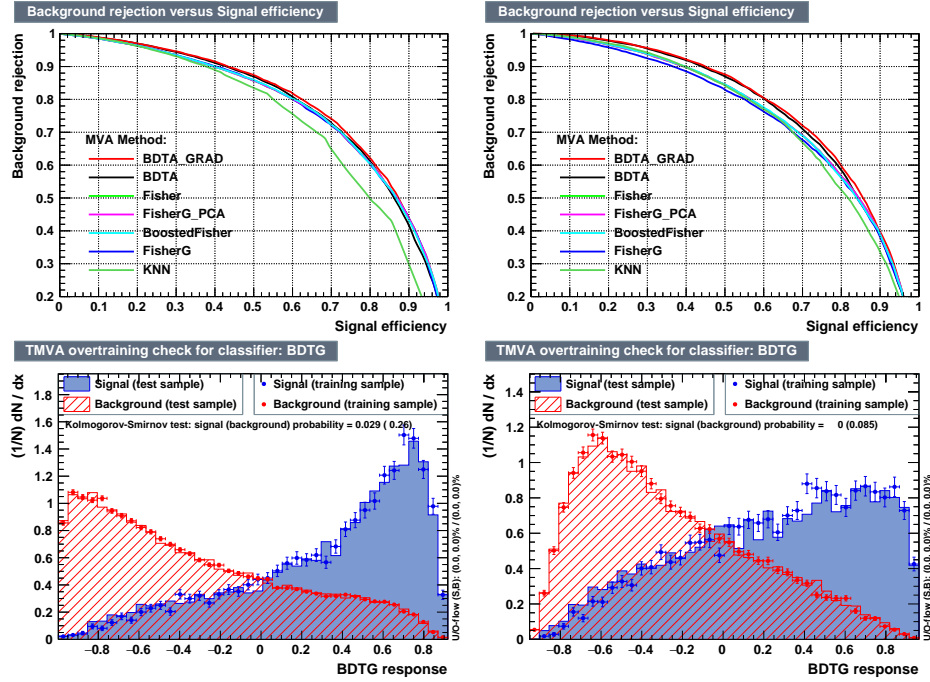


**Figure 5.7:** Top: background rejection vs signal efficiency (ROC curves) for various MVA classifiers (top) in the three lepton channel against  $t\bar{t}V$  (left) and  $t\bar{t}$  (right). Bottom: classifier output distributions for the gradient boosted decision trees, for training against  $t\bar{t}V$  (left) and against  $t\bar{t}$  (right).

1896 inator parameter values, with minimal overtraining. TMVA provides a ranking of the  
 1897 input variables by their importance in the classification process, shown in Tab. 5.10.  
 1898 The TMVA settings used in the BDT training are shown in Tab. 5.11.

ttbar training			ttV training		
Rank	Variable	Importance	Variable	Importance	Importance
1	minDRll	1.329e-01	dEtaFwdJetBJet	1.264e-01	
2	dEtaFwdJetClosestLep	1.294e-01	Lep3Pt	1.224e-01	
3	dEtaFwdJetBJet	1.209e-01	maxEtaJet25	1.221e-01	
4	dPhiHighestPtSSPair	1.192e-01	dEtaFwdJet2BJet	1.204e-01	
5	Lep3Pt	1.158e-01	dEtaFwdJetClosestLep	1.177e-01	
6	maxEtaJet25	1.121e-01	minDRll	1.143e-01	
7	dEtaFwdJet2BJet	9.363e-02	dPhiHighestPtSSPair	9.777e-02	
8	nJetEta1	6.730e-02	nJet25_Recl	9.034e-02	
9	nJet25_Recl	6.178e-02	nJetEta1	4.749e-02	
10	lepCharge	4.701e-02	lepCharge	4.116e-02	

**Table 5.10:** TMVA input variables ranking for BDTA\_GRAD method for the trainings in the three lepton channel. For both trainings the rankings show almost the same 5 variables in the first places.

---

```

TMVA.Types.kBDT
NTrees=800
BoostType=Grad
Shrinkage=0.10
!UseBaggedGrad
nCuts=50
MaxDepth=3
NegWeightTreatment=PairNegWeightsGlobal
CreateMVAPdfs

```

---

**Table 5.11:** TMVA configuration used in the BDT training.

## 1899    5.6 Additional discriminating variables

1900 Two additional discriminating variables were tested considering the fact that the  
 1901 forward jet in the background could come from the pileup; since we have a real  
 1902 forward jet in the signal, it could give some improvement in the discriminating power.  
 1903 The additional variables describe the forward jet momentum (fwdJetPt25) and the  
 1904 forward jet identification(fwdJetPUID). Distributions for these variables in the three  
 1905 lepton channel are shown in the figure 5.8. The forward jet identification distribution  
 1906 show that for both, signal and background, jets are mostly real jets.

1907 The testing was made including in the MVA input one variable at a time, so we

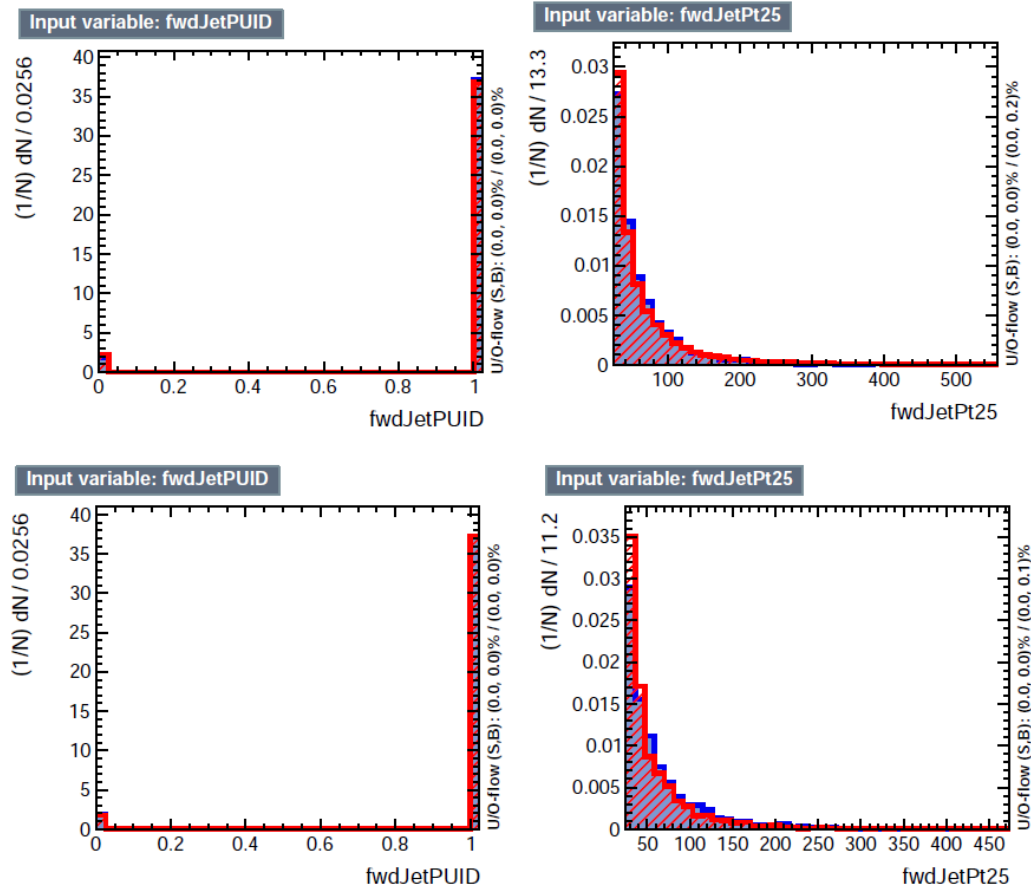


**Figure 5.8:** Additional discriminating variables distributions for ttV training (Top row) and tt training (bottom row) in the three lepton channel. The origin of the jets in the forward jet identification distribution is tagged as 0 for “pileup jets” while “real jets” are tagged as 1.

1908 can evaluate the discrimination power of each variable, and then both simultaneously.  
 1909 fwdJetPUID was ranked in the last place in importance (11) in both training (ttV  
 1910 and tt) while fwdJetPt25 was ranked 3 in the ttV training and 7 in the tt training.  
 1911 When training using 12 variables, fwdJetPt25 was ranked 5 and 7 in the ttV and tt  
 1912 trainings respectively, while fwdJetPUID was ranked 12 in both cases.

1913 The improvement in the discrimination performance provided by the additional  
 1914 variables is about 1%, so it was decided not to include them in the procedure. Table  
 1915 5.12 show the ROC-integral for all the testing cases we made.

ROC-integral	
base 10 var ttv	0.848
+ fwdJetPUID ttv	0.849
+ fwdJetPt25 ttv	0.856
12 var ttv	0.856
<hr/>	
base 10 var tt	0.777
+ fwdJetPUID tt	0.777
+ fwdJetPt25 tt	0.787
12 var	0.787

**Table 5.12:** ROC-integral for all the testing cases we made in the evaluation of the additional variables discriminating power. The improvement in the discrimination performance provided by the additional variables is about 1%

## 1916 References

- 1917 [1] J. Schwinger. "Quantum Electrodynamics. I. A Covariant Formulation". Physical Review. 74 (10): 1439-61, (1948).
- 1919 [2] R. P. Feynman. "Space-Time Approach to Quantum Electrodynamics". Physical Review. 76 (6): 769-89, (1949).
- 1921 [3] S. Tomonaga. "On a Relativistically Invariant Formulation of the Quantum Theory of Wave Fields". Progress of Theoretical Physics. 1 (2): 27-42, (1946).
- 1923 [4] D.J. Griffiths, "Introduction to electrodynamics". 4th ed. Pearson, (2013).
- 1924 [5] F. Mandl, G. Shaw. "Quantum field theory." Chichester: Wiley (2009).
- 1925 [6] F. Halzen, and A.D. Martin, "Quarks and leptons: An introductory course in modern particle physics". New York: Wiley, (1984) .
- 1927 [7] File: Standard\_Model\_of\_Elementary\_Particle\_dark.svg. (2017, June 12) Wikimedia Commons, the free media repository. Retrieved November 27, 2017 from <https://www.collegiate-advanced-electricity.com/single-post/2017/04/10/The-Standard-Model-of-Particle-Physics>.
- 1931 [8] E. Noether, "Invariante Variationsprobleme", Nachrichten von der Gesellschaft der Wissenschaften zu Göttingen, mathematisch-physikalische Klasse, vol. 1918, pp. 235-257, (1918).

- 1934 [9] C. Patrignani et al. (Particle Data Group), Chin. Phys. C, 40, 100001 (2016)  
 1935 and 2017 update.
- 1936 [10] M. Goldhaber, L. Grodzins, A.W. Sunyar “Helicity of Neutrinos”, Phys. Rev.  
 1937 109, 1015 (1958).
- 1938 [11] Palanque-Delabrouille N et al. “Neutrino masses and cosmology with Lyman-alpha forest power spectrum”, JCAP 11 011 (2015).
- 1940 [12] M. Gell-Mann. “A Schematic Model of Baryons and Mesons”. Physics Letters.  
 1941 8 (3): 214-215 (1964).
- 1942 [13] G. Zweig. “An SU(3) Model for Strong Interaction Symmetry and its Breaking”  
 1943 (PDF). CERN Report No.8182/TH.401 (1964).
- 1944 [14] G. Zweig. “An SU(3) Model for Strong Interaction Symmetry and its Breaking:  
 1945 II” (PDF). CERN Report No.8419/TH.412(1964).
- 1946 [15] M. Gell-Mann. “The Interpretation of the New Particles as Displaced Charged  
 1947 Multiplets”. Il Nuovo Cimento 4: 848. (1956).
- 1948 [16] T. Nakano, K, Nishijima. “Charge Independence for V-particles”. Progress of  
 1949 Theoretical Physics 10 (5): 581-582. (1953).
- 1950 [17] N. Cabibbo, “Unitary symmetry and leptonic decays” Physical Review Letters,  
 1951 vol. 10, no. 12, p. 531, (1963).
- 1952 [18] M.Kobayashi, T.Maskawa, “CP-violation in the renormalizable theory of weak  
 1953 interaction,” Progress of Theoretical Physics, vol. 49, no. 2, pp. 652-657, (1973).
- 1954 [19] File: Weak Decay (flipped).svg. (2017, June 12). Wikimedia Com-  
 1955 mons, the free media repository. Retrieved November 27, 2017 from

- 1956        [https://commons.wikimedia.org/w/index.php?title=File:Weak\\_Decay\\_\(flipped\).svg&oldid=247498592](https://commons.wikimedia.org/w/index.php?title=File:Weak_Decay_(flipped).svg&oldid=247498592).
- 1958 [20] Georgia Tech University. Coupling Constants for the Fundamental  
1959 Forces(2005). Retrieved January 10, 2018, from <http://hyperphysics.phy-astr.gsu.edu/hbase/Forces/couple.html#c2>
- 1961 [21] M. Strassler. (May 31, 2013).The Strengths of the Known Forces. Retrieved Jan-  
1962 uary 10, 2018, from <https://profmattstrassler.com/articles-and-posts/particle-physics-basics/the-known-forces-of-nature/the-strength-of-the-known-forces/>
- 1964 [22] S.L. Glashow. “Partial symmetries of weak interactions”, Nucl. Phys. 22 579-  
1965 588, (1961).
- 1966 [23] A. Salam, J.C. Ward. “Electromagnetic and weak interactions”, Physics Letters  
1967 13 168-171, (1964).
- 1968 [24] S. Weinberg, “A model of leptons”, Physical Review Letters, vol. 19, no. 21, p.  
1969 1264, (1967).
- 1970 [25] M. Peskin, D. Schroeder, “An introduction to quantum field theory”. Perseus  
1971 Books Publishing L.L.C., (1995).
- 1972 [26] A. Pich. “The Standard Model of Electroweak Interactions”  
1973 <https://arxiv.org/abs/1201.0537>
- 1974 [27] F.Bellaiche. (2012, 2 September). “What’s this Higgs boson anyway?”. Retrieved  
1975 from: <https://www.quantum-bits.org/?p=233>
- 1976 [28] M. Endres et al. Nature 487, 454-458 (2012) doi:10.1038/nature11255

- 1977 [29] F. Englert, R. Brout. “Broken Symmetry and the Mass of Gauge  
1978 Vector Mesons”. Physical Review Letters. 13 (9): 321-23.(1964)  
1979 doi:10.1103/PhysRevLett.13.321
- 1980 [30] P.Higgs. “Broken Symmetries and the Masses of Gauge Bosons”. Physical Re-  
1981 view Letters. 13 (16): 508-509,(1964). doi:10.1103/PhysRevLett.13.508.
- 1982 [31] G.Guralnik, C.R. Hagen and T.W.B. Kibble. “Global Conservation Laws  
1983 and Massless Particles”. Physical Review Letters. 13 (20): 585-587, (1964).  
1984 doi:10.1103/PhysRevLett.13.585.
- 1985 [32] CMS collaboration. “Observation of a new boson at a mass of 125 GeV with  
1986 the CMS experiment at the LHC”. Physics Letters B. 716 (1): 30-61 (2012).  
1987 arXiv:1207.7235. doi:10.1016/j.physletb.2012.08.021
- 1988 [33] ATLAS collaboration. “Observation of a New Particle in the Search for the Stan-  
1989 dard Model Higgs Boson with the ATLAS Detector at the LHC”. Physics Letters  
1990 B. 716 (1): 1-29 (2012). arXiv:1207.7214. doi:10.1016/j.physletb.2012.08.020.
- 1991 [34] ATLAS collaboration; CMS collaboration (26 March 2015). “Combined Mea-  
1992 surement of the Higgs Boson Mass in pp Collisions at  $\sqrt{s}=7$  and 8 TeV with  
1993 the ATLAS and CMS Experiments”. Physical Review Letters. 114 (19): 191803.  
1994 arXiv:1503.07589. doi:10.1103/PhysRevLett.114.191803.
- 1995 [35] LHC InternationalMasterclasses“When protons collide”. Retrieved from  
1996 [http://atlas.physicsmasterclasses.org/en/zpath\\_protoncollisions.htm](http://atlas.physicsmasterclasses.org/en/zpath_protoncollisions.htm)
- 1997 [36] CMS Collaboration, “SM Higgs Branching Ratios and To-  
1998 tal Decay Widths (up-date in CERN Report4 2016)”).

- 1999 https://twiki.cern.ch/twiki/bin/view/LHCPhysics/CERNYellowReportPageBR  
 2000 , last accessed on 17.12.2017.
- 2001 [37] R.Grant V. “Determination of Higgs branching ratios in  $H \rightarrow W^+W^- \rightarrow l\nu jj$  and  $H \rightarrow ZZ \rightarrow l^+l^-jj$  channels”. Physics Department, University of Tennessee (Dated: October 31, 2012). Retrieved from <http://aesop.phys.utk.edu/ph611/2012/projects/Riley.pdf>
- 2005 [38] LHC Higgs Cross Section Working Group, Denner, A., Heinemeyer, S. et al.  
 2006 “Standard model Higgs-boson branching ratios with uncertainties”. Eur. Phys.  
 2007 J. C (2011) 71: 1753. <https://doi.org/10.1140/epjc/s10052-011-1753-8>
- 2008 [39] F. Maltoni, K. Paul, T. Stelzer, and S. Willenbrock, “Associated production  
 2009 of Higgs and single top at hadron colliders”, Phys.Rev. D64 (2001) 094023,  
 2010 [hep-ph/0106293].
- 2011 [40] S. Biswas, E. Gabrielli, F. Margaroli, and B. Mele, “Direct constraints on the  
 2012 top-Higgs coupling from the 8 TeV LHC data,” Journal of High Energy Physics,  
 2013 vol. 07, p. 073, (2013).
- 2014 [41] M. Farina, C. Grojean, F. Maltoni, E. Salvioni, and A. Thamm, “Lifting de-  
 2015 generacies in Higgs couplings using single top production in association with a  
 2016 Higgs boson,” Journal of High Energy Physics, vol. 05, p. 022, (2013).
- 2017 [42] T.M. Tait and C.-P. Yuan, “Single top quark production as a window to physics  
 2018 beyond the standard model”, Phys. Rev. D 63 (2000) 014018 [hep-ph/0007298].
- 2019 [43] F. Demartin, F. Maltoni, K. Mawatari, and M. Zaro, “Higgs production in  
 2020 association with a single top quark at the LHC,” European Physical Journal C,  
 2021 vol. 75, p. 267, (2015).

- 2022 [44] CMS Collaboration, “Modelling of the single top-quark pro-  
 2023 duction in association with the Higgs boson at 13 TeV.”  
 2024 <https://twiki.cern.ch/twiki/bin/viewauth/CMS/SingleTopHiggsGeneration13TeV>,  
 2025 last accessed on 16.01.2018.
- 2026 [45] CMS Collaboration, “SM Higgs production cross sections at  $\sqrt{s} = 13$  TeV.”  
 2027 <https://twiki.cern.ch/twiki/bin/view/LHCPhysics/CERNYellowReportPageAt13TeV>, last  
 2028 accessed on 16.01.2018.
- 2029 [46] S. Dawson, The effective W approximation, Nucl. Phys. B 249 (1985) 42.
- 2030 [47] S. Biswas, E. Gabrielli and B. Mele, JHEP 1301 (2013) 088 [[arXiv:1211.0499 \[hep-ph\]](#)].
- 2032 [48] F. Demartin, B. Maier, F. Maltoni, K. Mawatari, and M. Zaro, “tWH associated  
 2033 production at the LHC”, European Physical Journal C, vol. 77, p. 34, (2017).  
 2034 [arXiv:1607.05862](#)
- 2035 [49] LHC Higgs Cross Section Working Group, “Handbook of LHC Higgs Cross  
 2036 Sections: 4.Deciphering the Nature of the Higgs Sector”, [arXiv:1610.07922](#).
- 2037 [50] J. Ellis, D. S. Hwang, K. Sakurai, and M. Takeuchi.“Disentangling Higgs-Top  
 2038 Couplings in Associated Production”, JHEP 1404 (2014) 004, [[arXiv:1312.5736](#)].
- 2039 [51] CMS Collaboration, V. Khachatryan et al., “Precise determination of the mass  
 2040 of the Higgs boson and tests of compatibility of its couplings with the standard  
 2041 model predictions using proton collisions at 7 and 8 TeV,” [arXiv:1412.8662](#).
- 2042 [52] ATLAS and CMS Collaborations, “Measurements of the Higgs boson produc-  
 2043 tion and decay rates and constraints on its couplings from a combined ATLAS

- 2044 and CMS analysis of the LHC pp collision data at  $sqrts = 7$  and 8 TeV,” (2016).  
 2045 CERN-EP-2016-100, ATLAS-HIGG-2015-07, CMS-HIG-15-002.
- 2046 [53] File:Cern-accelerator-complex.svg. Wikimedia Commons,  
 2047 the free media repository. Retrieved January, 2018 from  
 2048 <https://commons.wikimedia.org/wiki/File:Cern-accelerator-complex.svg>
- 2049 [54] J.L. Caron , “Layout of the LEP tunnel including future LHC infrastructures.”,  
 2050 (Nov, 1993). A C Collection. Legacy of AC. Pictures from 1992 to 2002. Re-  
 2051 trieval from <https://cds.cern.ch/record/841542>
- 2052 [55] M. Vretenar, “The radio-frequency quadrupole”. CERN Yellow Report CERN-  
 2053 2013-001, pp.207-223 DOI:10.5170/CERN-2013-001.207. arXiv:1303.6762
- 2054 [56] L.Evans. P. Bryant (editors). “LHC Machine”. JINST 3 S08001 (2008).
- 2055 [57] CERN Photographic Service.“Radio-frequency quadrupole, RFQ-1”, March  
 2056 1983, CERN-AC-8303511. Retrieved from <https://cds.cern.ch/record/615852>.
- 2057 [58] CERN Photographic Service “Animation of CERN’s accelerator net-  
 2058 work”, 14 October 2013. DOI: 10.17181/cds.1610170 Retrieved from  
 2059 <https://videos.cern.ch/record/1610170>
- 2060 [59] C.Sutton. “Particle accelerator”.Encyclopedia Britannica. July 17, 2013. Re-  
 2061 trieval from <https://www.britannica.com/technology/particle-accelerator>.
- 2062 [60] L.Guiraud. “Installation of LHC cavity in vacuum tank.”. July 27 2000. CERN-  
 2063 AC-0007016. Retrieved from <https://cds.cern.ch/record/41567>.
- 2064 [61] J.L. Caron, “Magnetic field induced by the LHC dipole’s superconducting coils”.  
 2065 March 1998. AC Collection. Legacy of AC. Pictures from 1992 to 2002. LHC-  
 2066 PHO-1998-325. Retrieved from <https://cds.cern.ch/record/841511>

- 2067 [62] AC Team. “Diagram of an LHC dipole magnet”. June 1999. CERN-DI-9906025  
2068 retrieved from <https://cds.cern.ch/record/40524>.
- 2069 [63] CMS Collaboration “Public CMS Luminosity Information”.  
2070 <https://twiki.cern.ch/twiki/bin/view/CMSPublic/LumiPublicResults#2016>  
2071 \_proton\_proton\_13\_TeV\_collis, last accessed 24.01.2018
- 2072 [64] J.L Caron. “LHC Layout” AC Collection. Legacy of AC. Pictures  
2073 from 1992 to 2002. September 1997, LHC-PHO-1997-060. Retrieved from  
2074 <https://cds.cern.ch/record/841573>.
- 2075 [65] J.A. Coarasa. “The CMS Online Cluster: Setup, Operation and Maintenance  
2076 of an Evolving Cluster”. ISGC 2012, 26 February - 2 March 2012, Academia  
2077 Sinica, Taipei, Taiwan.
- 2078 [66] CMS Collaboration. “The CMS experiment at the CERN LHC” JINST 3 S08004  
2079 (2008).
- 2080 [67] CMS Collaboration. “CMS detector drawings 2012” CMS-PHO-GEN-2012-002.  
2081 Retrieved from <http://cds.cern.ch/record/1433717>.
- 2082 [68] R. Breedon. “View through the CMS detector during the cooldown of the  
2083 solenoid on February 2006. CMS Collection”, February 2006, CMS-PHO-  
2084 OREACH-2005-004, Retrieved from <https://cds.cern.ch/record/930094>.
- 2085 [69] A. Dominguez et. al. “CMS Technical Design Report for the Pixel Detector  
2086 Upgrade”, CERN-LHCC-2012-016. CMS-TDR-11.
- 2087 [70] CMS Collaboration. “Description and performance of track and primary-vertex  
2088 reconstruction with the CMS tracker,” Journal of Instrumentation, vol. 9, no.  
2089 10, p. P10009,(2014).

- 2090 [71] CMS Collaboration and M. Brice. “Images of the CMS Tracker Inner  
2091 Barrel”, November 2008, CMS-PHO-TRACKER-2008-002. Retrieved from  
2092 <https://cds.cern.ch/record/1431467>.
- 2093 [72] M. Weber. “The CMS tracker”. 6th international conference on hyperons, charm  
2094 and beauty hadrons Chicago, June 28-July 3 2004.
- 2095 [73] CMS Collaboration. “Projected Performance of an Upgraded CMS Detector at  
2096 the LHC and HL-LHC: Contribution to the Snowmass Process”. Jul 26, 2013.  
2097 arXiv:1307.7135
- 2098 [74] L. Veillet. “End assembly of HB with EB rails and rotation in-  
2099 side SX ”,January 2002. CMS-PHO-HCAL-2002-002. Retrieved from  
2100 <https://cds.cern.ch/record/42594>.
- 2101 [75] J. Puerta-Pelayo.“First DT+RPC chambers installation round in the  
2102 UX5 cavern.”. January 2007, CMS-PHO-OREACH-2007-001. Retrieved from  
2103 <https://cds.cern.ch/record/1019185>
- 2104 [76] X. Cid Vidal and R. Cid Manzano. “CMS Global Muon Trigger” web  
2105 site: Taking a closer look at LHC. Retrieved from [https://www.lhc-closer.es/taking\\_a\\_closer\\_look\\_at\\_lhc/0.lhc\\_trigger](https://www.lhc-closer.es/taking_a_closer_look_at_lhc/0.lhc_trigger)
- 2107 [77] WLCG Project Office, “Documents & Reference - Tiers - Structure,” (2014).  
2108 <http://wlcg.web.cern.ch/documents-reference> , last accessed on 30.01.2018.
- 2109 [78] CMS Collaboration. “CMSSW Application Framework”,  
2110 <https://twiki.cern.ch/twiki/bin/view/CMSPublic/WorkBookCMSSWFFramework>,  
2111 last accesses 06.02.2018

- 2112 [79] A. Buckleya, J. Butterworthb, S. Giesekec, et. al. “General-purpose event gen-  
 2113 erators for LHC physics”. arXiv:1101.2599v1 [hep-ph] 13 Jan 2011
- 2114 [80] A. Quadt. “Top Quark Physics at Hadron Colliders”. Advances in the Physics  
 2115 of Particles and Nuclei. Springer-Verlag Berlin Heidelberg. DOI: 10.1007/978-  
 2116 3-540-71060-8 (2007)
- 2117 [81] DurhamHep Data Project, “The Durham HepData Project - PDF Plotter.”  
 2118 <http://hepdata.cedar.ac.uk/pdf/pdf3.html> , last accessed on 02.02.2018.
- 2119 [82] F. Maltoni, G. Ridolfi, and M. Ubiali, “b-initiated processes at the LHC: a  
 2120 reappraisal,” Journal of High Energy Physics, vol. 07, p. 022, (2012).
- 2121 [83] B. Andersson, G. Gustafson, G. Ingelman and T. Sjostrand, “Parton fragmen-  
 2122 tation and string dynamics”, Physics Reports, Vol. 97, No. 2-3, pp. 31-145,  
 2123 1983.
- 2124 [84] CMS Collaboration, “Event generator tunes obtained from underlying event  
 2125 and multiparton scattering measurements;” European Physical Journal C, vol.  
 2126 76, no. 3, p. 155, (2016).
- 2127 [85] J. Alwall et. al., “The automated computation of tree-level and next-to-leading  
 2128 order differential cross sections, and their matching to parton shower simula-  
 2129 tions,” Journal of High Energy Physics, vol. 07, p. 079, (2014).
- 2130 [86] S. Frixione, P. Nason, and C. Oleari, “Matching NLO QCD computations with  
 2131 Parton Shower simulations: the POWHEG method,” Journal of High Energy  
 2132 Physics, vol. 11, p. 070, (2007).
- 2133 [87] S. Agostinelli et al., “GEANT4: A Simulation toolkit,” Nuclear Instruments  
 2134 and Methods in Physics, vol. A506, pp. 250–303, (2003).

- 2135 [88] J.Allison et.al.,“Recent developments in Geant4”, Nuclear Instruments and  
 2136 Methods in Physics Research A 835 (2016) 186-225.
- 2137 [89] CMS Collaboration “Full Simulation Offline Guide”,  
 2138 <https://twiki.cern.ch/twiki/bin/view/CMSPublic/SWGuideSimulation>, last  
 2139 accessed 04.02.2018
- 2140 [90] A. Giammanco. “The Fast Simulation of the CMS Experiment” J. Phys.: Conf.  
 2141 Ser. 513 022012 (2014)
- 2142 [91] A.M. Sirunyan et. al. “Particle-flow reconstruction and global event description  
 2143 with the CMS detector”, JINST 12 P10003 (2017) <https://doi.org/10.1088/1748-0221/12/10/P10003>.
- 2145 [92] The CMS Collaboration. “ Description and performance of track and pri-  
 2146 mary vertex reconstruction with the CMS tracker”. JINST 9 P10009 (2014).  
 2147 doi:10.1088/1748-0221/9/10/P10009
- 2148 [93] P. Billoir and S. Qian, “Simultaneous pattern recognition and track fitting by  
 2149 the Kalman filtering method”, Nucl. Instrum. Meth. A 294 219. (1990).
- 2150 [94] W. Adam, R. Fruhwirth, A. Strandlie and T. Todorov, “Reconstruction of  
 2151 electrons with the Gaussian sum filter in the CMS tracker at LHC”, eConf  
 2152 C 0303241 (2003) TULT009 [physics/0306087].
- 2153 [95] CMS Collaboration, “Search for the associated production of a Higgs boson  
 2154 with a single top quark in proton-proton collisions at  $\sqrt{s} = 8$  TeV”, JHEP 06  
 2155 (2016) 177,doi:10.1007/JHEP06(2016)177, arXiv:1509.08159.

- 2156 [96] B. Stieger, C. Jorda Lope et al., “Search for Associated Production of a Single  
2157 Top Quark and a Higgs Boson in Leptonic Channels”, CMS Analysis Note CMS  
2158 AN-14-140, 2014.
- 2159 [97] M. Peruzzi, C. Mueller, B. Stieger et al., “Search for ttH in multilepton final  
2160 states at  $\sqrt{s} = 13$  TeV”, CMS Analysis Note CMS AN-16-211, 2016.
- 2161 [98] CMS Collaboration, “Search for H to bbar in association with a single top quark  
2162 as a test of Higgs boson couplings at  $\sqrt{s} = 13$  TeV”, CMS Physics Analysis  
2163 Summary CMS-PAS-HIG-16-019, 2016.
- 2164 [99] B. Maier, “SingleTopHiggProduction13TeV”, February, 2016.  
2165 <https://twiki.cern.ch/twiki/bin/viewauth/CMS/SingleTopHiggsGeneration13TeV>.
- 2166 [100] M. Peruzzi, F. Romeo, B. Stieger et al., “Search for ttH in multilepton final1  
2167 states at  $\sqrt{s} = 13$  TeV”, CMS Analysis Note CMS AN-17-029, 2017.
- 2168 [101] B. WG, “BtagRecommendation80XReReco”, February, 2017.  
2169 <https://twiki.cern.ch/twiki/bin/view/CMS/BtagRecommendation80XReReco>.